

Surpassing the loss-noise robustness trade-off in quantum key distribution

Hannah Seabrook,^{1,2,*} Emilien Lavie,¹ Teodor Strömberg,³ Matthew P. Stafford,^{1,2} and Giulia Rubino^{1,4,†}

¹*Quantum Engineering Technology Labs, H. H. Wills Physics Laboratory and Department and Electrical & Electronic Engineering, University of Bristol, BS8 1FD, United Kingdom*

²*Quantum Engineering Centre for Doctoral Training, Centre for Nanoscience and Quantum Information, University of Bristol, United Kingdom*

³*Institute of Science and Technology Austria, Klosterneuburg, Austria*

⁴*H. H. Wills Physics Laboratory, University of Bristol, Tyndall Avenue, Bristol, BS8 1TL, United Kingdom*

(Dated: December 13, 2024)

Quantum key distribution (QKD) offers a theoretically secure method to share secret keys, yet practical implementations face challenges due to noise and loss over long-distance channels. Traditional QKD protocols require extensive noise compensation, hindering their industrial scalability and lowering the achievable key rates. Alternative protocols encode logical qubits in noise-resilient states, but at the cost of using many physical qubits, increasing susceptibility to loss and limiting transmission distance. In this work, we introduce a logical qubit encoding that uses antisymmetric Bell-states in the continuous photonic degrees of freedom, frequency and time. By leveraging the continuous space, we overcome this noise-loss robustness trade-off by minimising the number of photons per logical qubit, whilst optimising the encoding resilience over noise fluctuations. We analyse the security of our encoding and demonstrate its robustness compared to existing state-of-the-art protocols. This approach provides a path towards scalable, efficient QKD implementations under realistic noise conditions.

Quantum information theory reached key milestones with the establishment of early protocols such as BB84 [1] and advancements like Shor’s algorithm [2], which showcased its transformative potential for real-world applications. These developments solidified the field’s focus on practical challenges, laying the foundation for quantum technologies today [3]. Among these technologies, quantum key distribution (QKD) stands out as a leading candidate for near-term applications and commercialisation due to its potential for fundamentally secure communication [4, 5]. However, transitioning QKD from theoretical models to scalable, industrial implementations remains a significant challenge [6]. Achieving high key rates across a large-scale QKD network requires extensive stabilisation and compensation techniques to overcome the noise experienced by qubits in transmission [7–9]. For example, twin-field QKD (TF-QKD), while enabling state-of-the-art key rates, requires the stabilisation of two lasers’ frequencies, polarisations, and field phases across long-distance noisy channels [10–12]. Impressive systems have been demonstrated experimentally that actively stabilise these elements [9, 13–16]. Nonetheless, this raises the question of whether an alternative approach to implementing QKD could offer a path forward without the substantial overheads required for compensated QKD.

Here, we investigate such an alternative solution: devising a QKD protocol that encodes information into inherently noise-resilient states. Such protocols have previously been proposed, e.g., for resilience against collective unitary noise channels [17–21], and they typically encode logical qubits in the subspace of a higher-dimensional space formed from many photonic qubits. However, these

approaches inherently involve a trade-off between loss-robustness and noise-robustness (see Table I). On the one hand, increasing the number of qubits improves the noise-robustness of the logical subspace, and beyond a minimum qubit threshold, the logical states can be made perfectly noise-robust. On the other hand, if even one photon is lost in transmission, the whole logical state is compromised. Thus, increasing the number of photons in the logical state makes it exponentially more susceptible to photon loss, severely limiting the distance over which the secret key can be shared.

In this work, we introduce an encoding scheme that reduces the number of photons in a logical qubit state, thereby minimising the impact of loss, whilst increasing the robustness of the logical state to noise. Inspired loosely by bosonic codes—a field of quantum error correction that uses the redundancy of infinite-dimensional Hilbert spaces to encode logical qubits and mitigate physical errors [22]—we exploit similar redundancies in a continuous photonic degree of freedom (DoF) to achieve noise resilience. Specifically, our encoding represents logical qubit states in superpositions across two-photon antisymmetric Bell-states defined over frequency bins and time bins. The antisymmetric structure of the states ensures intrinsic robustness to noise. At the same time, by utilizing superpositions of excitations across modes of a continuous photonic DoF, our encoding reduces the number of photons required for a logical qubit, thus offering a low-loss alternative to noise-robust QKD protocols.

We illustrate the robustness of our protocol under two continuous channel noise models: one experimentally motivated (chromatic dispersion) and the other motivated

Protocol	Loss scaling	No stabilisation needed?	Robust to collective unitary noise?	Robust to randomly varying unitary noise parameters?
TF-QKD [10]	$\eta^{1/2}$	✗	✗	✗
BB84 [1]	η	✗	✗	✗
Wang (2005) [17]	η^2	✓	✓	✗
This work	η^2	✓	✓	✓
Boileau <i>et al.</i> (2004) 3-photon [18]	η^3	✓	✓	✓
Boileau <i>et al.</i> (2004) 4-photon [18]	η^4	✓	✓	✓
Li <i>et al.</i> (2008) [19]	η^4	✓	✓	✓

TABLE I. **Comparison of commonly employed protocols and existing noise-robust protocols in terms of loss- and noise-robustness.** Protocols are listed with increasing susceptibility to photon loss down the table, where $\eta = 10^{-\text{loss(dB)}/10}$ is the channel transmissivity. Twin-Field QKD (TF-QKD) [10] and BB84 [1] are not robust to noise fluctuations, requiring extensive stabilisation techniques for their effective operation. As our protocol utilises both frequency-bin and time-bin qubits, in Section II B we outline the model used to assess the robustness of our protocol on conjugate qubits, in the form of a unitary on frequency-bin qubits. In Appendix A, we further detail this loss-noise robustness trade-off.

to enable a comparison with existing discrete variable (DV) encoded protocols (a unitary applied to frequency-bin qubits). Additionally, we demonstrate that the parameters of our encoding can be optimised over fluctuations in noise parameters.

Finally, we perform a rigorous and unified key rate analysis of our protocol under the noise models and loss channel, and compare the key rates to those of existing noise-robust protocols [17–19]. We show that our protocol surpasses the noise-resilience of two-photon protocols [17] and the loss-robustness of perfectly noise-cancelling protocols [18, 19]. These results highlight how encoding in continuous DoFs can enhance the robustness of secure communication protocols.

In the following section, we present our encoding. In Section II, we demonstrate the noise-robust properties of our encoding. In Section III, we analyse and discuss the security of our protocol and existing protocols in lossy and collective unitary noise channels. We conclude by discussing our findings and their implications and suggesting possible directions for future work.

I. PROTOCOL

Our protocol follows the BB84 scheme [1], with single photon states replaced by two-photon logical qubit states encoded in a continuous DoF for noise-resilience, as illustrated in Fig. 1. In the protocol, a sender (Alice) prepares states randomly in either the logical Z (which we label Z_L) basis $\{|0_L\rangle, |1_L\rangle\}$, or the logical X (X_L) basis $\{|\pm_L\rangle\} = (|0_L\rangle \pm |1_L\rangle)/\sqrt{2}$. Similarly, a receiver (Bob) measures randomly in either Z_L or X_L . Bob’s projectors are given by $\{|0_L\rangle\langle 0_L|, |1_L\rangle\langle 1_L|, |+_L\rangle\langle +_L|, |-_L\rangle\langle -_L|, |\perp_L\rangle\langle \perp_L|\}$, where $|\perp_L\rangle$ corresponds to an inconclusive measurement due to loss or the measurement of a state outside of the logical

subspace.

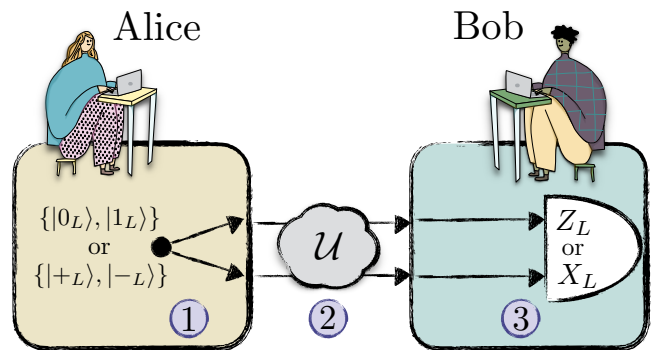


Fig 1. **Depiction of the BB84 protocol using logical noise-robust qubit states.** We propose a BB84 protocol using logical noise-robust states to improve key rates in noisy channels. Alice prepares a logical qubit in either the Z_L or X_L basis, randomly, encoding the bit value 0 in $|0_L\rangle$ or $|+_L\rangle$ and the bit value 1 in $|1_L\rangle$ or $|-_L\rangle$. She sends the state to Bob, who measures randomly in either the Z_L or X_L basis. After transmission, Alice and Bob discard cases with mismatched bases and check for errors due to an eavesdropper on a subset of the remaining bits. If the error rate is below a certain threshold, they proceed with error correction and privacy amplification, otherwise they abort the protocol. We assume the channel induces ‘collective noise’, applying the same unknown transformation \mathcal{U} to each photon in the logical state.

To describe our encoding, we simply need to establish the encoding of the Z_L basis states $\{|0_L\rangle, |1_L\rangle\}$, as the X_L basis states and the measurement operators follow trivially. We use antisymmetric Bell-states to encode $|0_L\rangle$ and $|1_L\rangle$ in such a way that they are naturally robust to noise, as in the existing DV protocols [17–19] (reviewed in Supplementary Material (SM), Sec. S.I). These states are invariant under local collective unitary operations, i.e., $(U \otimes U) |\Psi^-\rangle = e^{i\Delta} |\Psi^-\rangle$ where $|\Psi^-\rangle = \frac{1}{\sqrt{2}}(|0\rangle|1\rangle - |1\rangle|0\rangle)$ and Δ is some U -dependent

global phase factor [23] (see Appendix A). To minimise the number of photons per logical state, we encode the Z_L basis states as two-photon antisymmetric Bell-states in conjugate variables, frequency and time.

Our encoding is built in two layers. The first layer is formed of single-photon physical qubits. In this layer, we define single-photon physical qubit states in conjugate variables: the single-photon frequency-bin qubit states that we label by $\{|0_f\rangle, |1_f\rangle\}$, and the single-photon time-bin qubit states that we label as $\{|0_t\rangle, |1_t\rangle\}$. The second layer is the logical encoding layer (labelled by subscript- L). In the logical layer, we construct two two-photon antisymmetric Bell-states, one from the frequency-bin qubits of the first layer, and the other from the time-bin qubits. These two antisymmetric Bell-states act as the building blocks of our logical qubit space $\{|0_L\rangle, |1_L\rangle\}$.

We start by defining the first layer of the encoding using bosonic creation operators on the vacuum state $|\emptyset\rangle$. We define the creation operator for a photon occupying a frequency-bin mode as

$$\hat{a}_{\Omega_i, A}^\dagger = \int d\omega f_{\Omega_i, \sigma_\omega}(\omega) \hat{a}_A^\dagger(\omega), \quad (1)$$

where $\hat{a}_A^\dagger(\omega)$ is the creation operator for a photon in some mode A (for example, a polarisation mode or a spatial mode) with frequency ω , and $f_{\Omega_i, \sigma_\omega}(\omega)$ is the frequency-bin mode amplitude function centred around Ω_i with width σ_ω , that we take to be the state-normalised Gaussian function.

Similarly, we define the creation operator for a photon occupying a time-bin mode as

$$\hat{a}_{\tau_i, A}^\dagger = \int dt f_{\tau_i, \sigma_t}(t) \hat{a}_A^\dagger(t) = \int d\omega F_{\tau_i, \sigma_t}(\omega) \hat{a}_A^\dagger(\omega), \quad (2)$$

where $\hat{a}_A^\dagger(t)$ is the creation operator for a photon in some mode A at time t and $f_{\tau_i, \sigma_t}(t)$ is the time-bin mode amplitude function centred around τ_i with width σ_t , that we model as the state-normalised Gaussian function. The second equality shows that this can be expressed as a creation operator on frequency modes by applying the Fourier transform between frequency and time. In this context, $F_{\tau_i, \sigma_t}(\omega)$ is the Fourier transform of $f_{\tau_i, \sigma_t}(t)$, and ω is now defined relative to the central frequency of the states.

Defining two frequency bins centred at frequencies Ω_0 and Ω_1 and two time bins centred at times τ_0 and τ_1 , we can now define single-photon frequency-bin qubit and time-bin qubit states as

$$|i_x\rangle_A = \hat{a}_{\mu_i, A}^\dagger |\emptyset\rangle, \quad (3)$$

where $i \in \{0, 1\}$ and $x \in \{f, t\}$, where f stands for the frequency-bin states and t is for the time-bin states, and μ_i is Ω_i or τ_i , respectively. This assumes that Ω_0 and Ω_1 , and τ_0 and τ_1 are sufficiently well separated such that

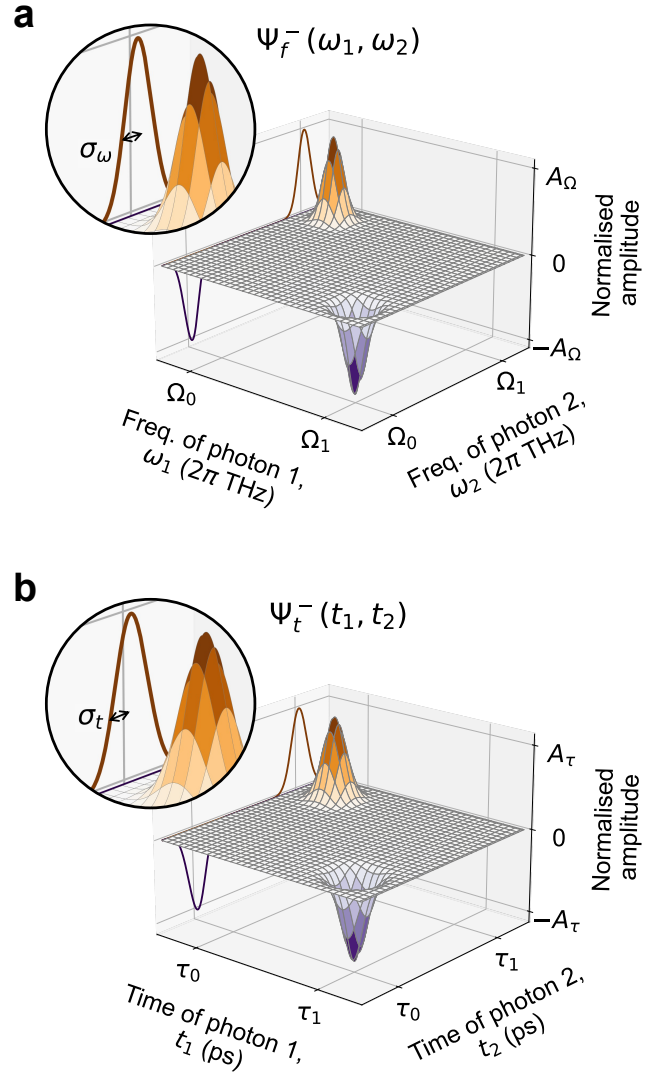


Fig 2. **2D joint frequency and temporal spectra of the frequency-bin and time-bin encoded antisymmetric Bell-states used to form the logical states $|0_L\rangle$ and $|1_L\rangle$.** (a) The normalised bi-photon wavefunction amplitude of the antisymmetric frequency-bin encoded Bell-state $|\Psi_f^-\rangle$ visualised in the frequency domain and (b) the normalised bi-photon wavefunction amplitude of the antisymmetric time-bin encoded Bell-state $|\Psi_t^-\rangle$ visualised in the time domain. A_Ω and A_τ are the peak amplitudes of the wavefunctions (set by the normalisation conditions and the encoding parameters $\vec{\Omega}$ and $\vec{\tau}$, respectively – see SM, Sec. S.II). The insets highlights the widths, σ_ω and σ_t , of the 1D frequency bins and time bins.

$\langle 0_x | 1_x \rangle_A \approx 0$. For brevity, we label the parameters of the frequency-bin and time-bin qubits by $\vec{\Omega} = (\Omega_0, \Omega_1, \sigma_\omega)$ and $\vec{\tau} = (\tau_0, \tau_1, \sigma_t)$, respectively.

We now establish the logical encoding layer, formed from bi-photon antisymmetric Bell-states in frequency

bins and time bins. We define these as

$$|\Psi_x^-\rangle = \frac{|0_x\rangle_A |1_x\rangle_B - |1_x\rangle_A |0_x\rangle_B}{\sqrt{2}}, \quad (4)$$

where the labels A and B signify that the two photons are distinguished by some extra mode (e.g., spatial mode or polarisation). The states $|\Psi_f^-\rangle$ in the frequency domain and $|\Psi_t^-\rangle$ in the time domain are depicted in Fig. 2. $|\Psi_f^-\rangle$ and $|\Psi_t^-\rangle$ define a 2-dimensional logical Hilbert space. The logical states in the Z_L basis are given by

$$|0_L\rangle = |\Psi_f^-\rangle \quad |1_L\rangle = |\Psi_{\perp f}^-\rangle, \quad (5)$$

where $|\Psi_{\perp f}^-\rangle$ is a state orthogonal to $|\Psi_f^-\rangle$, defined according to

$$|\Psi_{\perp f}^-\rangle = \frac{(|\Psi_t^-\rangle - a|\Psi_f^-\rangle)}{\sqrt{1 - |a|^2}}, \quad (6)$$

where a is the overlap of the frequency-bin and time-bin Bell-states, $\langle\Psi_f^-|\Psi_t^-\rangle$. Typical experimental parameters give a negligible value for a , and, in fact, $|\Psi_f^-\rangle$ and $|\Psi_t^-\rangle$ can be made perfectly distinguishable (i.e., $a = 0$) by tuning $\vec{\Omega}$ and $\vec{\tau}$ (see SM, Sec. S.II). In Appendix B, we propose one possible method for preparing these states and measuring in the two bases, using domain-engineered non-linear crystals.

In the next section, we demonstrate the robustness of this encoding to different noise channels and their parameter fluctuations.

II. NOISE-ROBUSTNESS OF ENCODING

We now showcase the resilience of our encoding against two example channel noise models. First, we briefly demonstrate the robustness of our encoding under a common experimental noise model (dispersion), illustrating the applicability of our encoding to typical experimental scenarios. This initial analysis is heuristic, with a detailed quantitative study and figures provided in the SM, Sec. S.VIII. The remainder of this section is dedicated to in-depth analysis of our encoding’s resilience to a theoretically-motivated noise model (the “frequency beamsplitter” (FBS)). This model enables us to compare the efficacy of our encoding’s noise-robustness to that of the existing protocols in Refs [17–19], which we subsequently present in Section III.

A. Dispersion noise

Chromatic dispersion is an optical property of transparent media in which the phase velocity and group velocity of light traversing a medium are frequency-dependent [24] (typical in optical fibres, for example [25]).

In this subsection, we present the analytical noise model of chromatic dispersion and summarise the effect of this noise on our encoding and its key rates.

By expanding the frequency-dependent wavevector of light in a dispersive media about some frequency ω_0 , the effect of n -th order dispersion on the photon’s spectral amplitude can be written as

$$g(\omega) \mapsto e^{i\alpha_n(\omega-\omega_0)^n} g(\omega), \quad (7)$$

where α_n is the corresponding dispersion coefficient (as derived in the SM, Sec. S.VIII). Typical materials only need consideration of the group delay dispersion (GDD), $n = 1$ term, and the group velocity dispersion (GVD), $n = 2$ term. When higher-order terms have to be considered, it is often more convenient to use direct numerical modelling [24].

GDD ($n = 1$) physically corresponds to a simple time-delay of the pulses sent by Alice, as understood by the time-shift property of the Fourier transform. Both our protocol and current QKD experiments can cancel this using common synchronisation techniques based on the arrival time of a reference signal from Alice at Bob [26–29]. Synchronisation ensures Alice and Bob assign the same sequence number to each event [30], and that the time-bin basis state labels of Alice’s encoding align with those of Bob’s measurement for time-bin encoded QKD. However, our encoding relaxes the synchronisation requirements needed for typical time-bin encoded QKD. Only synchronising the events’ sequence number is necessary, as an offset between Alice and Bob’s time-bin labels results in an incurred loss rather than a quantum bit error rate (QBER) for our protocol (see SM, Sec. S.VIII C).

GVD ($n = 2$) instead changes the shape of the temporal probability amplitude by broadening it. For single-qubit time-bin encoded QKD, this broadening effect compromises the security of the protocol over intermediate distances (≈ 50 km of fibre), unless appropriate compensation is employed [28]. This occurs due to the QBER rapidly increasing as the pulses spread into the neighbouring time bins. In contrast, for our encoding, GVD increases the effective loss, due to an increasing rate of inconclusive outcomes as the photons’ probability density “leaks” outside of Bob’s logical measurement subspace. However, this does not raise the QBER, allowing our protocol to maintain security under this noise at long distances.

Overall, the effect of chromatic dispersion on our encoding results in decaying oscillations of key rate as a function of $|\alpha_n|$. The decay rate is due to the increased inconclusive outcomes and depends on the encoding parameters $\vec{\Omega}$ and $\vec{\tau}$. The oscillations arise from an α_n -dependent decoherence phase imparted on the single-qubit frequency-bin states, due to the difference in dispersive phase between the two central frequencies. This corresponds to a decoherence phase at the logical layer of our encoding, resulting in an oscillating phase error rate,

with a period depending again on $\vec{\Omega}$ and $\vec{\tau}$. The encoding parameters can be optimised to maintain significant key rates across the channel, by ensuring the key rate oscillation period is large compared to the variation of the dispersion parameters, α_n , (e.g., due to varying temperature [31]). This allows the key rate to remain close to a maximum within the fluctuation range of α_n . Figures, further mathematical analysis, and the consideration of real experimental parameters are presented in the SM, Sec. S.VIII.

B. Frequency beamsplitter (FBS) noise

To compare the noise resilience of our protocol against existing protocols that leverage antisymmetric Bell-states (Refs. [17–19]), we now consider an alternative noise model based on frequency-bin qubits. While the physical encoding of Refs. [17–19] can be expressed in a discrete Hilbert space, our logical qubit encoding utilises two distinct physical qubit types defined in conjugate variables, requiring representation in a continuous space. To address this, we define the FBS noise model, which applies a unitary operation on frequency-bin qubits, enabling a direct comparison of the noise-robustness of these protocols and ours (assuming the former are encoded in frequency-bin qubits). Although rooted in theoretical considerations, this noise model has potential experimental relevance, for example, in processes such as Bragg scattering four-wave mixing [32].

1. Frequency beamsplitter model

We first define a single-frequency beamsplitter (BS) operation. A single-frequency BS acts on pairs of single-frequency creation operators $\hat{a}^\dagger(\omega)$ to apply a BS unitary operation, U_{BS} , on the frequency modes in the form $\hat{a}^\dagger(\omega_1) \mapsto \cos \theta \hat{a}^\dagger(\omega_1) + e^{i\phi} \sin \theta \hat{a}^\dagger(\omega_2)$ and $\hat{a}^\dagger(\omega_2) \mapsto -e^{-i\phi} \sin \theta \hat{a}^\dagger(\omega_1) + \cos \theta \hat{a}^\dagger(\omega_2)$. This applies a unitary operation between a pair of single-frequency modes, with rotation noise parameter θ , and dephasing noise parameter ϕ .

We now generalise the single-frequency BS to define the general FBS noise model, illustrated in Fig. 3. In the general FBS model, the same (but unknown) single-frequency BS operations act between pairs of frequencies, separated by μ , over continuous frequency intervals of width ϵ . The first interval is centred on frequency Ω and, correspondingly, the second interval on the frequency $\Omega + \mu$. For brevity, we label the FBS noise parameters by $\vec{\epsilon} = (\Omega, \mu, \epsilon)$. The action of this model in the frequency domain is made mathematically explicit in the SM, Sec. S.III and further extended in SM, Sec. S.IV.

Before analysing the impact of the FBS noise model on our encoding, it is helpful to summarise the key param-

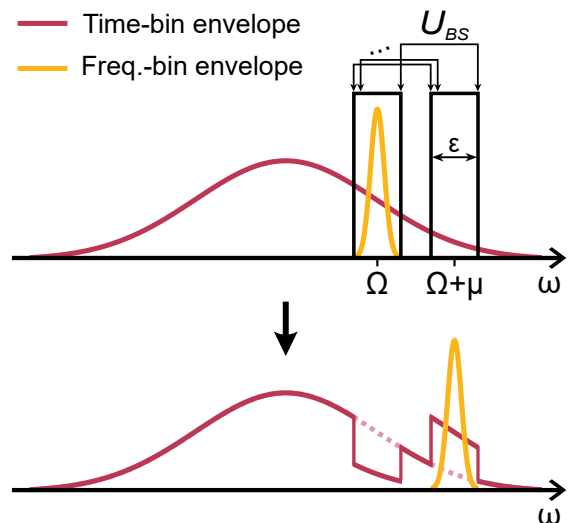


Fig 3. **Schematic of the frequency beamsplitter (FBS) noise model.** The FBS model applies a beamsplitter unitary (U_{BS}) across pairs of frequency modes separated by μ over continuous frequency intervals of width ϵ , as shown in the top diagram. For the example of a bit-flip, X , operation on single-photon time-bin and frequency-bin states, this operation transforms the pink and yellow states in the top diagram to the corresponding states in the bottom diagram. The pink curve represents the broad spectral amplitude envelope of the time-bin states, whilst the orange curve depicts a frequency-bin state.

ters introduced so far. The frequency-bin qubit states are parameterised by frequencies Ω_0 and Ω_1 , and Gaussian width σ_ω . The time-bin qubit states are parameterised by times τ_0 and τ_1 , and Gaussian width σ_t . We then parameterise the FBS noise model as a unitary operation across frequency modes with rotation angle θ and dephasing angle ϕ . This FBS noise acts on frequency bins centred around Ω and $\Omega + \mu$, with a top-hat filter shape of width ϵ .

2. Effect of frequency beamsplitter noise

To analyse the effect of the FBS on our encoding, we must first make assumptions about the relationship of parameters $\vec{\epsilon}$ to $\vec{\Omega}$. We assume that the FBS acts exactly across the frequency-bin states of Alice’s encoding (i.e. $\Omega = \Omega_0$ and $\Omega + \mu = \Omega_1$), and the noise bands are sufficiently wide to capture the Gaussian amplitude, as in Fig. 3 (requiring $\epsilon \gtrsim 6\sigma_\omega$ to contain all but a negligible fraction of the Gaussian function). Under these assumptions, the FBS applies a unitary operation on the frequency-bin qubit states $\{|0_f\rangle, |1_f\rangle\}$. Thus, $|0_L\rangle = |\Psi_f^-\rangle$ is unaffected by this noise.

In contrast, the $|1_L\rangle$ state will be affected under the FBS. Due to the broad nature of the time bins in the fre-

quency domain, both $|0_t\rangle$ and $|1_t\rangle$ span both of the FBS bins (pink curve in Fig. 3). Therefore, the FBS does not apply a logical unitary to the time-bin qubit states, but does change the shape of their distribution (with a dependence on $\vec{\epsilon}, \theta, \phi$), as depicted in Fig. 3 and SM, Fig. S2. As with GVD, the changing time-bin state distribution increases the rate of inconclusive measurement outcomes at Bob due to the probability amplitude “leaking” outside of the logical subspace.

To quantitatively analyse the effect this has on the key rate, we consider the states measured by Bob ($|\Psi_t^-\rangle$ and $|\Psi_f^-\rangle$) and the time-bin state arriving at Bob after traversing the FBS noise, which we call $|\Psi_t'^-\rangle$. Here, we assume the encoding uses $a = 0$ for simplicity of analysis. We calculate the fidelities $\mathcal{F}(\Psi_t'^-, \Psi_t^-) = |\langle \Psi_t'^- | \Psi_t^- \rangle|^2$ and $\mathcal{F}(\Psi_t'^-, \Psi_f^-) = |\langle \Psi_t'^- | \Psi_f^- \rangle|^2$, and any phase accumulated by $|\Psi_t'^-\rangle$, as a function of $\vec{\epsilon}, \theta, \phi$, and the encoding parameters $\vec{\tau}$ and $\vec{\Omega}$. The sum of these fidelities equals the probability of Bob measuring a conclusive outcome given $|\Psi_t'^-\rangle$ arrived. $\mathcal{F}(\Psi_t'^-, \Psi_f^-)$ gives the bit error rate in the logical encoding, and the phase accumulated by $|\Psi_t'^-\rangle$ relative to $|\Psi_t^-\rangle$ and $|\Psi_f^-\rangle$ gives rise to a phase error rate.

The bit error is negligible in general and thus has negligible effect on the key rate. For example, for the experimentally reported parameters used in Fig. 4, $\mathcal{F}(\Psi_t'^-, \Psi_f^-)$ is numerically found to be 10^{-4} for varying θ, ϕ (giving less than 0.3% reduction in key rate). Thus, we will ignore the effect of this for our analysis. Further, for typical parameters (such as those used in Fig. 4), the accumulated relative phase is small and has minimal effect on the key rate. Therefore, the effect of the FBS on the key rate is dominated by $\mathcal{F}(\Psi_t'^-, \Psi_t^-)$. Further details on the accumulated phase and bit error can be found in SM, Sec. S.III B 2 and S.III C, respectively.

Fig. 4 shows the fidelity $\mathcal{F}(\Psi_t'^-, \Psi_t^-)$ of a time-bin Bell-state under an FBS, using experimentally reported values, for various noise bin widths ϵ , as a function of θ and ϕ . We observe that the state fidelity is approximately independent of the FBS dephasing angle ϕ , and reduces with FBS rotation angle θ . As ϵ decreases, the fidelity is higher for a given θ and ϕ . If the time-bin states are sufficiently wide in the frequency domain ($\propto 1/\sigma_t$) compared to ϵ , the effect of the noise is small on the time-bin states. Thus, our encoding will show a high rate of conclusive outcomes at Bob, giving high key rates, for any values of the noise parameters θ, ϕ . The detailed analytical expression for $\mathcal{F}(\Psi_t'^-, \Psi_t^-)$ and the study of further parameter dependence is presented in the SM, Sec. S.III B.

In this analysis, we demonstrated the robustness of our encoding against variations in noise parameters using fixed settings. Alternatively, our protocol can be adapted by optimising the encoding parameters to enhance robustness when noise fluctuations can be characterized, as detailed in Appendix C. The fixed-parameter

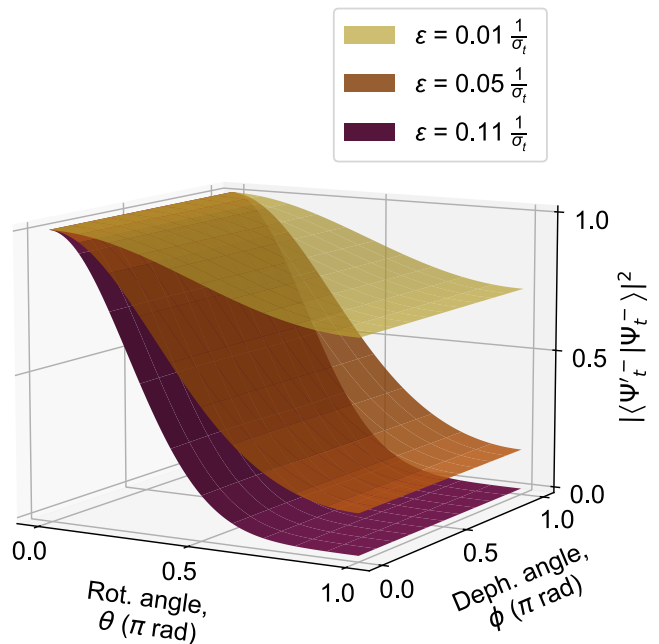


Fig. 4. **Robustness of time-bin Bell-states under the FBS noise model, for varying frequency noise bin widths.** Fidelity between the arriving state $|\Psi_t'^-\rangle$ sent by Alice through the FBS channel and the state $|\Psi_t^-\rangle$ measured by Bob. The fidelity is plotted as a function of the FBS channel parameters θ and ϕ . For the simulation, we use the time-bin parameters $\tau_0 = 0$ ps, $\tau_1 = 220$ ps, and $\sigma_t = 17$ ps (values experimentally reported in Ref [33]) and FBS noise parameters $\Omega = 195.860$ THz, $\Omega + \mu = 195.879$ THz, with varying width $\epsilon = 0.6$ GHz, 3.0 GHz, 6.6 GHz (close to experimentally reported values for a frequency-bin Bell-state encoding in Ref [34], with $\epsilon = 6\sigma_\omega$). In the legend, we express ϵ as a fraction of the time-bin state’s width in the frequency domain ($\propto \frac{1}{\sigma_t}$). We take the the central frequency of the time-bin state to equal Ω .

approach is ideal when noise characterization is impractical, while the second strategy enables fine-tuned performance in scenarios where detailed noise characterization is possible.

Overall, neglecting the effect of bit error rate, we can model the effect of the FBS noise channel on our logical qubit as an amplitude damping and decoherence channel, where the damping probability and decoherence phase are dependent on the channel noise parameters $\vec{\epsilon}, \theta, \phi$.

In Appendix D, we highlight the advantages of our proposed encoding compared to alternative continuous DoF encodings with only two photons. Specifically, we demonstrate how our use of both time-bin and frequency-bin qubits allows us to make fewer assumptions on the channel noise model.

III. SECURITY ANALYSIS

In this section, we present a comparative security analysis of our protocol against existing ones that are robust against collective unitary noise [17, 18] and the standard BB84 protocol [1] under the FBS model introduced above. We extend this model to analyse the security under experimentally realistic noise fluctuations, by using a probabilistic value for the noise parameter θ . Subsequently, we compare these schemes under a lossy channel, additionally including TF-QKD in the analysis. Despite its alternative set-up—featuring two senders and a central measuring device, unlike the prepare-and-measure BB84-type scheme used by the others—the inclusion of TF-QKD allows for a rigorous comparison of our protocol with state-of-the-art approaches. We conclude by discussing how the stabilisation techniques required for TF-QKD and BB84 affect their key rates and implementation overheads. We leave the analysis of Ref. [19] to SM, Sec. S.VII B, as it does not contribute further insights to the main discussion.

It is worth noting that the protocols in Refs. [17–19] were developed during the early years of QKD, when robustness against specific individual attacks was the primary focus. Here, we harness more recent developments in numerical techniques for QKD security analysis to provide asymptotic secure key rates valid against any collective attack. More precisely, we use the framework developed in Ref. [35] to compute an asymptotic lower bound on the secure key rates for each of the protocols listed above, as well as our proposed implementation. We provide an explanation and full details of the analysis methods used in the SM, Sec. S.V.

A. Noise-robust protocols under the FBS channel

In this subsection, we consider Refs. [1, 17–19] implemented using frequency-bin qubits (with a width less than the noise bin widths, i.e., $\epsilon \gtrsim 6\sigma_\omega$). With this encoding, their security can be analysed by examining the effects of a collective unitary operation (Appendix A) on the physical qubit states, as described in the previous section.

By contrast, the FBS channel affects our logical encoding differently, causing amplitude damping and decoherence of our logical qubit states (see Section II B 2). To evaluate the key rate of our protocol under this noise, we use the key rate of BB84 subjected to an amplitude damping and decoherence channel (given in Appendix E). The fidelities of our encoding under the FBS (Fig. 4) determine the amplitude damping, while the accumulated phases correspond to the decoherence phase for each set of noise parameters $(\vec{\epsilon}, \theta, \phi)$. Using this conversion, we can compute the key rate of our protocol for each choice

of values for the noise parameters.

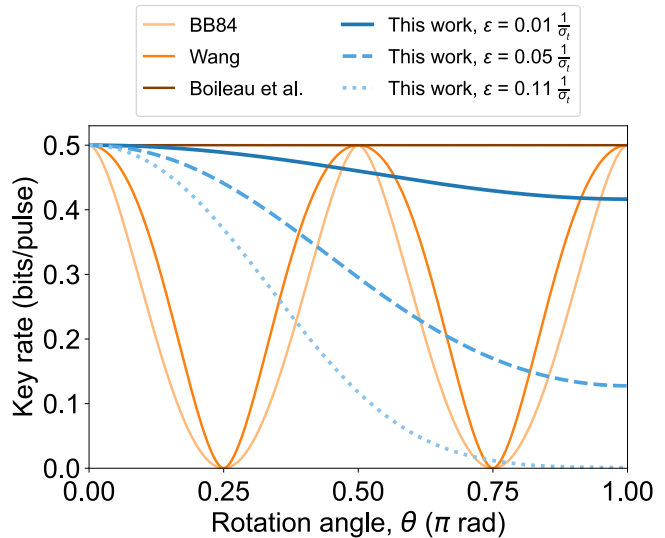


Fig 5. **Comparison of key rates as a function of FBS noise parameter θ (with $\phi = 0$) for collective unitary noise robust protocols.** Key rate in an FBS channel with unitary parameter θ of the BB84 (yellow), Wang (2005) [17], Boileau *et al.* (2004) [18] and our protocol for the states and noise outlined in Fig. 4 ($\tau_0 = 0$ ps, $\tau_1 = 220$ ps, $\sigma_t = 17$ ps, and noise parameters $\Omega = 195.860$ THz, $\Omega + \mu = \Omega_1 = 195.879$ THz, $\epsilon = 6\sigma_\omega = 0.5, 3, 6.6$ GHz). The action of the FBS on the DV protocols is analysed as a collective unitary operation on frequency-bin qubits.

Fig. 5 shows the secure key rates of the different protocols in a lossless FBS channel as a function of the unitary rotation angle θ , with other parameters fixed. The FBS noise and the encoding parameters match those of the surfaces in Fig. 4. The key rate is symmetric in θ about $\theta = \pi$ for all protocols, due to the symmetry of the FBS operation under θ . In the SM, Sec. S.VI and S.VII A, we provide an additional analysis showing the key rate’s ϕ -dependence (which is small for all protocols presented).

The three- and four-photon protocols in Ref. [18] perfectly cancel collective unitary noise, therefore their key rates are maximal for both unitary parameters (θ, ϕ) in a lossless channel. We illustrate this with the flat-line reference plot in Fig. 5, and need not consider the noise robustness further here.

We now analyse the one- and two-photon protocols. Our protocol shows a substantial improvement in key rate compared to Refs. [1, 17] for $0 < \theta \lesssim 0.4\pi$. As the noise width reduces relative to the time-bin width in the frequency domain, the key rate robustness to θ increases (blue curves in Fig. 5). With sufficiently narrow FBS noise bins or optimised σ_t of our states, the key rate of our protocol remains non-zero for all unitary parameters (θ, ϕ) , unlike Refs. [1, 17]. This, combined with preventing the accumulation of a bit error rate, is advantageous for our encoding when experimental time

variations of noise parameters are accounted for.

We demonstrate this by updating the FBS channel model to consider random mixtures of parameters instead. We now model the channel as a FBS with fixed parameter values θ_i , with probabilities p_i , so that the channel map becomes

$$\rho_N \rightarrow \sum_i p_i \hat{F}_{\theta_i}^{\otimes N} \rho_N \hat{F}_{\theta_i}^{\dagger \otimes N}, \quad (8)$$

where we define \hat{F}_θ as the action of the FBS with parameter θ and all the other unspecified parameters \vec{c}, ϕ kept fixed. In our simulation, we consider points of θ_i uniformly sampled between 0 and 2π .

Under Eq. (8), we find the key rate for both Ref. [1] and [17] vanishes. Indeed, while a positive key can be obtained both in the regime where $\theta < \frac{\pi}{4}$ and $\theta > \frac{\pi}{4}$, these two regimes correspond to Alice and Bob's bit value being correlated and anticorrelated, respectively. As a result, under a random mixture of θ , no correlation can be established. In contrast, our protocol can maintain a positive key rate since the bit values remain correlated throughout the parameter range. The dotted, dashed and solid blue lines in Fig 5 achieve rates of 0.124, 0.278, 0.457 bits/pulse, respectively.

B. Noise-robust protocols in lossy channels

We now present the analysis of different DV-QKD protocols across a loss-only channel. Fig. 6 shows the key rate dependence of our protocol, noise-robust protocols with a varying number of photons per logical state [17, 18], BB84 [1] and TF-QKD [10]. These results highlight quantitatively the loss-noise robustness trade-off discussed earlier and presented in Table I (and Appendix A). From Fig. 6 we confirm that, for a given channel loss, the key rate scales exponentially with the number of photons in a protocol. However, as seen in Fig. 5 above, reducing the number of photons in a logical state decreases the protocol's robustness to noise, underscoring the trade-off.

Our scheme requires only two photons per logical state, and thus scales better with loss than other noise-robust protocols. Meanwhile, by exploiting non-trivial encodings in continuous DoFs, it leads to an increased parameter robustness than the existing methods with two or less qubits (Fig. 5). Therefore, by optimising the encoding parameters to expected noise fluctuations (Fig. 4 and Appendix C), our approach can surpass the key rates of previously proposed noise-robust schemes.

In the SM, Sec. S.VII, we present further discussion of the observed key rates for Refs. [17–19], and compare the rates to the security predicted in their works.

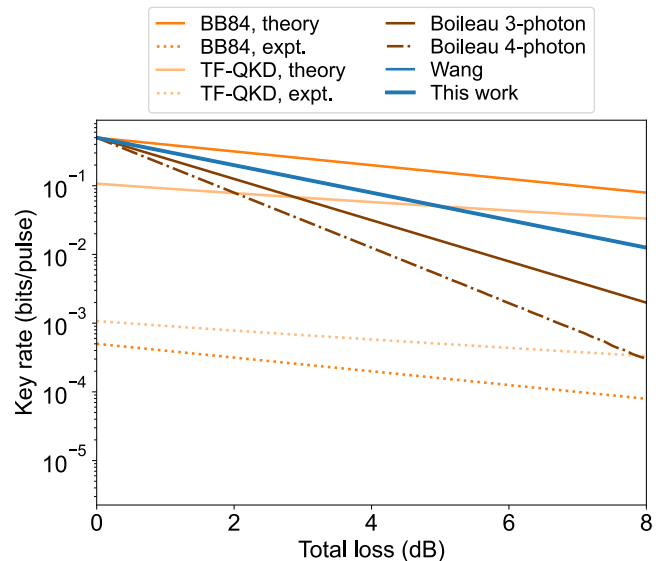


Fig 6. **Key rate as a function of channel loss in dB for collective unitary noise robust protocols and commonly implemented QKD protocols.** Comparison of the key rate scaling with loss for various protocols in a lossy but otherwise noiseless channel. Our scheme and the existing collective unitary noise-robust approaches [17, 18] show a BB84 scaling ($\sim \eta$) with loss. For these, the key rate for a given loss scales exponentially with the number of photons in the logical qubit state. Our protocol and Ref [17] use the same number of photons per logical state, and thus show the same loss dependence (thick blue line). For comparison, we also show the key rate for BB84 [1] (simulated) and TF-QKD [10] (analytically calculated in Ref. [36], with $\mu = \mu_{opt} = 0.1146$) both for their ideal theoretical implementations and with the reduction in key rate due to stabilisation techniques.

C. Compensation techniques for BB84 and TF-QKD

Fig. 6 includes the key rates of BB84 [1] and TF-QKD [10]. By construction, these schemes scale better with loss than the noise-robust protocols, achieving higher key rates over longer distances. However, implementing these protocols in practice relies on extensive compensation and stabilisation techniques to mitigate the effects of channel fluctuations (discussed further in Appendix A) [9, 11, 13–15, 37–39]. These methods require allocating a portion of the pulses to estimating the noise, reducing the fraction available for establishing a shared secret key [37–39].

To account for compensation, in Fig. 6 we include experimentally reported key rates for BB84 and TF-QKD achieved using these techniques. For BB84 with polarisation compensation, Ref. [37] presents a secret key rate of 80 bits per second with 40 dB loss and a transmission rate of 50 MHz. Converting this to a key rate in bits/pulse, and accounting for detection losses, this corresponds to an order 10^3 reduction in key rate. For TF-

QKD, Ref. [14] reports a secret key rate of 9.22×10^{-11} bits/pulse at 106 dB loss. Accounting for detection and component losses, this corresponds to an order 10^2 reduction in key rate. We illustrate these in Fig. 5. We note that experiments employing different stabilisation methods will result in slight variations of the key rate reduction factor. An exhaustive analysis of the experimentally achieved key rates would require a more open discussion on experimental downtimes, duty cycles and other factors affecting the total average key rate. Detailed data in this area is currently limited.

DISCUSSION

In this work, we introduced a novel approach to encoding logical qubits for QKD, where they are represented within subspaces of continuous photonic DoFs. Specifically, we define a non-trivial orthonormal basis in the frequency domain from superpositions of antisymmetric Bell-states defined in frequency-bin and time-bin qubits. Antisymmetry is employed for its noise-resilient properties, while the use of a continuous DoF enhances loss-robustness by reducing the number of photons per logical state. Our analysis demonstrates that this scheme offers superior resilience to loss and noise compared to existing methods under realistic noise fluctuations. Furthermore, it eliminates the need for extensive stabilization typically required in state-of-the-art protocols. We also outlined a simple experimental implementation of our protocol, showcasing the near-term applicability of these findings for scalable QKD networks.

Recent works have explored architectures for quantum repeaters based on concatenated bosonic error-correcting codes, leveraging Gottesman-Kitaev-Preskill (GKP) qubits for their inherent loss-resilient properties [40–43]. While our protocol does not rely on error correction, it shares a conceptual connection with these approaches by exploiting redundancies in continuous photonic DoFs to achieve resilience against noise. Practical realisation of GKP states, however, remains a significant experimental challenge, particularly in optical implementations, with only recent progress reported [44]. Alternative strategies, such as that proposed by Ref. [45] for optical quantum computing, address these challenges by encoding GKP qubits in a fixed number of excitations superposed across frequency and time modes, rather than the typical bosonic codes which encode qubits in superpositions of the number of excitations within a single mode. This approach provides a more experimentally feasible route to the implementation of optical bosonic error-correcting codes.

Similarly to Ref. [45], our approach employs a fixed number of excitations in a superposition across modes of a continuous photonic DoF to improve the practical feasibility. However, the encoding we propose is specifically

tailored for QKD applications, enabling the use of simpler states since only noise-robustness, rather than full error correction, is required. Our approach opens new directions for exploring alternative encodings in continuous photonic DoFs for quantum information tasks, extending beyond the scope of QKD.

A natural extension of this research would be to adapt our encoding strategy to develop a general methodology for designing implementation-specific encodings. Such a framework could be optimised for robustness against experimentally characterised noise channels and their expected noise fluctuations, while minimising the impact of loss. For example, by modelling and parameterising the noise channel, and characterising the expected fluctuations of its parameters, it could be possible to develop tools that output optimal encoding spectral functions and their parameters for a given implementation. Additionally, while our encoding is not compatible with widely used protocols like decoy-state BB84 or TF-QKD, it could hold promise for other QKD protocols, such as device-independent QKD [46].

Beyond these immediate extensions, our work reveals a counter-intuitive result: antisymmetric Bell-states in frequency-bin and time-bin modes, despite their conjugate nature, can be made perfectly orthogonal. This property may have deeper connections to foundational topics in quantum mechanics, such as the nature of EPR steering [47]. While our results clearly establish the utility of this encoding for QKD, they also suggest broader implications for leveraging foundational principles in practical quantum technologies. We envision that these ideas could inspire new approaches across the field of quantum information, bridging foundational insights with real-world applications.

ACKNOWLEDGEMENTS

We thank B. Baragiola, A. Boubriak, M. Clark, M. Jones, and P. Skrzypczyk for useful discussions. **Funding:** H.S. acknowledges financial support from EPSRC Quantum Engineering Centre for Doctoral Training grant EP/SO23607/1. E.L. acknowledges support from the Engineering and Physical Sciences Research Council (EPSRC) Hub in Quantum Computing and Simulation (EP/T001062/1). T.S. acknowledges that they received no funding in support for this research. M.P.S. acknowledges support from EPSRC Quantum Engineering Centre for Doctoral Training EP/S023607/1 and the European Commission through Starting Grant ERC-2018-STG803665 (PEQEM). G.R. acknowledges support from the Royal Commission for the Exhibition of 1851 through a Research Fellowship, from the European Commission through Starting Grant ERC-2018-STG803665 (PEQEM) and Advanced Grant ERC-2020-ADG101021085 (FLQuant). **Competing interests:**

The authors declare that they have no competing interests. **Data Availability:** All codes used to generate the data presented in this article are available at <https://github.com/hmis4/SurpassingLNTradeOffQKD>.

* Corresponding author: hannah.seabrook@bristol.ac.uk

† Corresponding author: giulia.rubino@bristol.ac.uk

- [1] C. H. Bennett and G. Brassard, Proceedings of the IEEE International Conference on Computers, Systems, and Signal Processing. (e.d Goldwasser, S.), IEEE Press, 1984.
- [2] P. W. Shor, 35th Annual Symposium on Foundations of Computer Science: Proceedings ; November 20-22, 1994, Santa Fe, New Mexico. Annual Symposium on Foundations of Computer Science : proceedings (e.d Goldwasser, S.), IEEE Computer Society Press, 1994.
- [3] A. Acín, I. Bloch, H. Buhrman, T. Calarco, C. Eichler, J. Eisert, D. Esteve, N. Gisin, S. J. Glaser, F. Jelezko, S. Kuhr, M. Lewenstein, M. F. Riedel, P. O. Schmidt, R. Thew, A. Wallraff, I. Walmsley, and F. K. Wilhelm, “The quantum technologies roadmap: a european community view,” New Journal of Physics, vol. 20, p. 080201, aug 2018.
- [4] H.-K. Lo and H. F. Chau, “Unconditional security of quantum key distribution over arbitrarily long distances,” Science, vol. 283, no. 5410, pp. 2050–2056, 1999.
- [5] D. Mayers, “Unconditional security in quantum cryptography,” J. ACM, vol. 48, p. 351–406, May 2001.
- [6] E. Diamanti, H.-K. Lo, B. Qi, and Z. Yuan, “Practical challenges in quantum key distribution,” npj Quantum Information, vol. 2, p. 16025, November 2016.
- [7] M. Peranić, M. Clark, R. Wang, S. Bahrani, O. Alia, S. Wengerowsky, A. Radman, M. Lončarić, M. Stipčević, J. Rarity, R. Nejabati, and S. K. Joshi, “A study of polarization compensation for quantum networks,” EPJ Quantum Technology, vol. 10, p. 30, Aug 2023.
- [8] J.-Y. Liu, X. Liu, W. Zhang, and Y.-D. Huang, “Impact of fiber dispersion on the performance of entanglement-based dispersive optics quantum key distribution,” Journal of Electronic Science and Technology, vol. 19, no. 4, p. 100119, 2021.
- [9] L. Zhou, J. Lin, Y. Jing, and Z. Yuan, “Twin-field quantum key distribution without optical frequency dissemination,” Nature Communications, vol. 14, p. 928, Feb 2023.
- [10] M. Lucamarini, Z. L. Yuan, J. F. Dynes, and A. J. Shields, “Overcoming the rate–distance limit of quantum key distribution without quantum repeaters,” Nature, vol. 557, pp. 400–403, May 2018.
- [11] C. Clivati, A. Meda, S. Donadello, S. Virzi, M. Genovese, F. Levi, A. Mura, M. Pittaluga, Z. Yuan, A. J. Shields, M. Lucamarini, I. P. Degiovanni, and D. Calonico, “Coherent phase transfer for real-world twin-field quantum key distribution,” Nature Communications, vol. 13, p. 157, Jan 2022.
- [12] W. Li, L. Zhang, Y. Lu, Z.-P. Li, C. Jiang, Y. Liu, J. Huang, H. Li, Z. Wang, X.-B. Wang, Q. Zhang, L. You, F. Xu, and J.-W. Pan, “Twin-field quantum key distribution without phase locking,” Phys. Rev. Lett., vol. 130, p. 250802, Jun 2023.
- [13] M. Pittaluga, M. Minder, M. Lucamarini, M. Sanzaro, R. I. Woodward, M.-J. Li, Z. Yuan, and A. J. Shields, “600-km repeater-like quantum communications with dual-band stabilization,” Nature Photonics, vol. 15, pp. 530–535, Jul 2021.
- [14] J.-P. Chen, C. Zhang, Y. Liu, C. Jiang, D.-F. Zhao, W.-J. Zhang, F.-X. Chen, H. Li, L.-X. You, Z. Wang, Y. Chen, X.-B. Wang, Q. Zhang, and J.-W. Pan, “Quantum key distribution over 658 km fiber with distributed vibration sensing,” Phys. Rev. Lett., vol. 128, p. 180502, May 2022.
- [15] S. Wang, Z.-Q. Yin, D.-Y. He, W. Chen, R.-Q. Wang, P. Ye, Y. Zhou, G.-J. Fan-Yuan, F.-X. Wang, Y.-G. Zhu, P. V. Morozov, A. V. Divochiy, Z. Zhou, G.-C. Guo, and Z.-F. Han, “Twin-field quantum key distribution over 830-km fibre,” Nature Photonics, vol. 16, pp. 154–161, Feb 2022.
- [16] J.-P. Chen, F. Zhou, C. Zhang, C. Jiang, F.-X. Chen, J. Huang, H. Li, L.-X. You, X.-B. Wang, Y. Liu, Q. Zhang, and J.-W. Pan, “Twin-field quantum key distribution with local frequency reference,” Phys. Rev. Lett., vol. 132, p. 260802, Jun 2024.
- [17] X.-B. Wang, “Fault tolerant quantum key distribution protocol with collective random unitary noise,” Phys. Rev. A, vol. 72, p. 050304, Nov 2005.
- [18] J.-C. Boileau, D. Gottesman, R. Laflamme, D. Poulin, and R. W. Spekkens, “Robust polarization-based quantum key distribution over a collective-noise channel,” Phys. Rev. Lett., vol. 92, p. 017901, Jan 2004.
- [19] X.-H. Li, F.-G. Deng, and H.-Y. Zhou, “Efficient quantum key distribution over a collective noise channel,” Phys. Rev. A, vol. 78, p. 022321, Aug 2008.
- [20] P.-L. Guo, C. Dong, Y. He, F. Jing, W.-T. He, B.-C. Ren, C.-Y. Li, and F.-G. Deng, “Efficient quantum key distribution against collective noise using polarization and transverse spatial mode of photons,” Opt. Express, vol. 28, pp. 4611–4624, Feb 2020.
- [21] Y. Sun, Q.-Y. Wen, F. Gao, and F.-C. Zhu, “Robust variations of the bennett-brassard 1984 protocol against collective noise,” Phys. Rev. A, vol. 80, p. 032321, Sep 2009.
- [22] L. Berent, T. Hillmann, J. Eisert, R. Wille, and J. Roffe, “Analog information decoding of bosonic quantum low-density parity-check codes,” PRX Quantum, vol. 5, p. 020349, May 2024.
- [23] M. A. Nielsen and I. L. Chuang, Quantum Computation and Quantum Information: 10th Anniversary Edition. Cambridge University Press, 2010.
- [24] R. Paschotta, “Chromatic dispersion.” RP Photonics Encyclopedia.
- [25] A. Willner, Y.-W. Song, J. Mcgeehan, Z. Pan, and B. Hoanca, “Dispersion management,” in Encyclopedia of Modern Optics (R. D. Guenther, ed.), pp. 353–365, Oxford: Elsevier, 2005.
- [26] J. C. Bienfang, A. J. Gross, A. Mink, B. J. Hershman, A. Nakassis, X. Tang, R. Lu, D. H. Su, C. W. Clark, C. J. Williams, E. W. Hagley, and J. Wen, “Quantum key distribution with 1.25 gbps clock synchronization,” Opt. Express, vol. 12, pp. 2011–2016, May 2004.
- [27] I. Vagniluca, B. Da Lio, D. Rusca, D. Cazzolino, Y. Ding, H. Zbinden, A. Zavatta, L. K. Oxenløwe, and D. Bacco, “Efficient time-bin encoding for practical high-dimensional quantum key distribution,” Phys. Rev. Appl., vol. 14, p. 014051, Jul 2020.
- [28] A. Boaron, B. Korzh, R. Houlmann, G. Boso, D. Rusca, S. Gray, M.-J. Li, D. Nolan, A. Martin, and H. Zbinden,

- “Simple 2.5 GHz time-bin quantum key distribution,” *Applied Physics Letters*, vol. 112, p. 171108, 04 2018.
- [29] C.-Z. Wang, Y. Li, W.-Q. Cai, W.-Y. Liu, S.-K. Liao, and C.-Z. Peng, “Synchronization using quantum photons for satellite-to-ground quantum key distribution,” *Opt. Express*, vol. 29, pp. 29595–29603, Sep 2021.
- [30] A. V. Miller, “Time synchronization in satellite quantum key distribution,” *Problems of Information Transmission*, vol. 59, pp. 225–238, Dec 2023.
- [31] P. S. André and A. N. Pinto, “Chromatic dispersion fluctuations in optical fibers due to temperature and its effects in high-speed optical communication systems,” *Optics Communications*, vol. 246, no. 4, pp. 303–311, 2005.
- [32] D. Lee, W. Shin, S. Park, J. Kim, and H. Shin, “Noon-state interference in the frequency domain,” *Light: Science & Applications*, vol. 13, p. 90, Apr 2024.
- [33] G. Finco, F. Miserocchi, A. Maeder, J. Kellner, A. Sabatti, R. J. Chapman, and R. Grange, “Time-bin entangled Bell state generation and tomography on thin-film lithium niobate,” 2024.
- [34] M. Clementi, F. A. Sabattoli, M. Borghi, L. Gianini, N. Tagliavacche, H. El Dirani, L. Youssef, N. Bergamasco, C. Petit-Etienne, E. Pargon, J. E. Sipe, M. Liscidini, C. Sciancalepore, M. Galli, and D. Bajoni, “Programmable frequency-bin quantum states in a nano-engineered silicon device,” *Nature Communications*, vol. 14, p. 176, Jan 2023.
- [35] A. Winick, N. Lütkenhaus, and P. J. Coles, “Reliable numerical key rates for quantum key distribution,” *Quantum*, vol. 2, p. 77, July 2018.
- [36] J. Lin and N. Lütkenhaus, “Simple security analysis of phase-matching measurement-device-independent quantum key distribution,” *Phys. Rev. A*, vol. 98, p. 042332, Oct 2018.
- [37] C. Agnesi, M. Avesani, L. Calderaro, A. Stanco, G. Folletto, M. Zahidy, A. Scriminich, F. Vedovato, G. Vallone, and P. Villoresi, “Simple quantum key distribution with qubit-based synchronization and a self-compensating polarization encoder,” *Optica*, vol. 7, pp. 284–290, Apr 2020.
- [38] Y.-Y. Ding, W. Chen, H. Chen, C. Wang, Y.-P. Li, S. Wang, Z.-Q. Yin, G.-C. Guo, and Z.-F. Han, “Polarization-basis tracking scheme for quantum key distribution using revealed sifted key bits,” *Opt. Lett.*, vol. 42, pp. 1023–1026, Mar 2017.
- [39] Y. Du, X. Zhu, X. Hua, Z. Zhao, X. Hu, Y. Qian, X. Xiao, and K. Wei, “Silicon-based decoder for polarization-encoding quantum key distribution,” *Chip*, vol. 2, no. 1, p. 100039, 2023.
- [40] F. Rozpędek, K. Noh, Q. Xu, S. Guha, and L. Jiang, “Quantum repeaters based on concatenated bosonic and discrete-variable quantum codes,” *npj Quantum Information*, vol. 7, p. 102, Jun 2021.
- [41] F. Schmidt, D. Miller, and P. van Loock, “Error-corrected quantum repeaters with Gottesman-Kitaev-Preskill qudits,” *Phys. Rev. A*, vol. 109, p. 042427, Apr 2024.
- [42] K. Fukui, R. N. Alexander, and P. van Loock, “All-optical long-distance quantum communication with Gottesman-Kitaev-Preskill qubits,” *Phys. Rev. Res.*, vol. 3, p. 033118, Aug 2021.
- [43] F. Rozpędek, K. P. Seshadreesan, P. Polakos, L. Jiang, and S. Guha, “All-photonic Gottesman-Kitaev-Preskill-qubit repeater using analog-information-assisted multiplexed entanglement ranking,” *Phys. Rev. Res.*, vol. 5, p. 043056, Oct 2023.
- [44] S. Konno, W. Asavanant, F. Hanamura, H. Nagayoshi, K. Fukui, A. Sakaguchi, R. Ide, F. China, M. Yabuno, S. Miki, H. Terai, K. Takase, M. Endo, P. Marek, R. Filip, P. van Loock, and A. Furusawa, “Logical states for fault-tolerant quantum computation with propagating light,” *Science*, vol. 383, no. 6680, pp. 289–293, 2024.
- [45] E. Descamps, A. Keller, and P. Milman, “Gottesman-Kitaev-Preskill encoding in continuous modal variables of single photons,” *Phys. Rev. Lett.*, vol. 132, p. 170601, Apr 2024.
- [46] V. Zapatero, T. van Leent, R. Arnon-Friedman, W.-Z. Liu, Q. Zhang, H. Weinfurter, and M. Curty, “Advances in device-independent quantum key distribution,” *npj Quantum Information*, vol. 9, p. 10, Feb 2023.
- [47] M. D. Reid, P. D. Drummond, W. P. Bowen, E. G. Cavalcanti, P. K. Lam, H. A. Bachor, U. L. Andersen, and G. Leuchs, “Colloquium: The Einstein-Podolsky-Rosen paradox: From concepts to applications,” *Rev. Mod. Phys.*, vol. 81, pp. 1727–1751, Dec 2009.
- [48] C. H. Bennett, “Quantum cryptography using any two nonorthogonal states,” *Phys. Rev. Lett.*, vol. 68, pp. 3121–3124, May 1992.
- [49] A. Cabello, “Six-qubit permutation-based decoherence-free orthogonal basis,” *Phys. Rev. A*, vol. 75, p. 020301, Feb 2007.
- [50] A. Al-Juboori, H. Z. J. Zeng, M. A. P. Nguyen, X. Ai, A. Laucht, A. Solntsev, M. Toth, R. Malaney, and I. Aharonovich, “Quantum key distribution using a quantum emitter in hexagonal boron nitride,” *Advanced Quantum Technologies*, vol. 6, no. 9, p. 2300038, 2023.
- [51] S. Slussarenko and G. J. Pryde, “Photonic quantum information processing: A concise review,” *Applied Physics Reviews*, vol. 6, p. 041303, 10 2019.
- [52] S. Seshadri, H.-H. Lu, D. E. Leaird, A. M. Weiner, and J. M. Lukens, “Complete frequency-bin bell basis synthesizer,” *Phys. Rev. Lett.*, vol. 129, p. 230505, Dec 2022.
- [53] H.-P. Lo, T. Ikuta, K. Azuma, T. Honjo, W. J. Munro, and H. Takesue, “Generation of a time-bin Greenberger-Horne-Zeilinger state with an optical switch,” *Quantum Science and Technology*, vol. 8, p. 035003, apr 2023.
- [54] A. Dosseva, L. Cincio, and A. M. Brańczyk, “Shaping the joint spectrum of down-converted photons through optimized custom poling,” *Phys. Rev. A*, vol. 93, p. 013801, Jan 2016.
- [55] F. Graffitti, D. Kundys, D. T. Reid, A. M. Brańczyk, and A. Fedrizzi, “Pure down-conversion photons through sub-coherence-length domain engineering,” *Quantum Science and Technology*, vol. 2, p. 035001, jul 2017.
- [56] R.-B. Jin, K. Tazawa, N. Asamura, M. Yabuno, S. Miki, F. China, H. Terai, K. Minoshima, and R. Shimizu, “Quantum optical synthesis in 2D time-frequency space,” *APL Photonics*, vol. 6, p. 086104, 08 2021.
- [57] T. J. Herzog, J. G. Rarity, H. Weinfurter, and A. Zeilinger, “Frustrated two-photon creation via interference,” *Phys. Rev. Lett.*, vol. 72, pp. 629–632, Jan 1994.
- [58] A. Hochrainer, M. Lahiri, M. Erhard, M. Krenn, and A. Zeilinger, “Quantum indistinguishability by path identity and with undetected photons,” *Rev. Mod. Phys.*, vol. 94, p. 025007, Jun 2022.
- [59] A. M. Yao and M. J. Padgett, “Orbital angular momentum: origins, behavior and applications,” *Adv. Opt.*

- Photon., vol. 3, pp. 161–204, Jun 2011.
- [60] J. Burniston, W. Wang, L. Kamin, J. Lin, P. Coles, E. Metodiev, I. George, N. K. H. Li, K. Fang, M. Chemtov, Y. Zhang, C. Böhm, A. Winick, T. van Himbeeck, S. Johnstun, S. Nahar, D. Tupkary, S. Pan, Z. Wang, A. Corrigan, F. Kanitschar, L. Gracie, S. Gu, N. Mathur, T. Upadhyaya, and N. Lutkenhaus, “Open QKD Security: Version 2.0.2,” Dec. 2024.
- [61] M. Tomamichel, *Quantum Rényi Divergence*, pp. 47–72. Cham: Springer International Publishing, 2016.
- [62] S. Boyd and L. Vandenberghe, *Convex Optimization*. Cambridge University Press, 2004.
- [63] P. W. Shor, “Scheme for reducing decoherence in quantum computer memory,” *Phys. Rev. A*, vol. 52, pp. R2493–R2496, Oct 1995.
- [64] W. Wang and N. Lütkenhaus, “Numerical security proof for decoy-state bb84 and measurement-device-independent qkd resistant against large basis misalignment,” 2021.
- [65] O. Gittsovich, N. J. Beaudry, V. Narasimhachar, R. R. Alvarez, T. Moroder, and N. Lütkenhaus, “Squashing model for detectors and applications to quantum-key-distribution protocols,” *Phys. Rev. A*, vol. 89, p. 012325, Jan 2014.
- [66] G. J. Milburn and S. Basiri-Esfahani, “Quantum optics with one or two photons,” *Proceedings of the Royal Society A: Mathematical, Physical and Engineering Sciences*, vol. 471, no. 2180, p. 20150208, 2015.
- [67] B. J. Smith and M. G. Raymer, “Photon wave functions, wave-packet quantization of light, and coherence theory,” *New Journal of Physics*, vol. 9, p. 414, nov 2007.
- [68] E. Hecht, *Optics*. Harlow, England: Pearson Education, fifth edition ed., 2017.
- [69] B. E. A. Saleh and M. C. Teich, *Fundamentals of Photonics*. Hoboken, NJ: Wiley, 3rd ed., 2019.
- [70] M. N. Polyanskiy, “Refractiveindex.info database of optical constants,” *Scientific Data*, vol. 11, p. 94, Jan 2024.
- [71] I. H. Malitson, “Interspecimen comparison of the refractive index of fused silica*,†,” *J. Opt. Soc. Am.*, vol. 55, pp. 1205–1209, Oct 1965.
- [72] C. Tan, “Determination of refractive index of silica glass for infrared wavelengths by ir spectroscopy,” *Journal of Non-Crystalline Solids*, vol. 223, no. 1, pp. 158–163, 1998.
- [73] R. Paschotta, “Propagation losses.” RP Photonics Encyclopedia. Available online at https://www.rp-photonics.com/propagation_losses.html.

Appendix A: Fundamental trade-off between loss-robust and noise-robust QKD

In this appendix, we outline the collective unitary noise channel and the loss channel models considered for the analysis of Refs. [17–19]. We then discuss the overheads of employing compensation techniques to mitigate noise fluctuations. Finally, we explain the loss-noise robustness trade-off in more detail. We highlight this with the specific example of protocols that exploit antisymmetry for robustness to collective unitary noise, such as those in Refs. [17–19].

1. Collective unitary noise channel

A collective unitary noise channel applies the same unknown unitary U to all qubits in a given N -qubit state, ρ_N , transforming the state as

$$\rho_N \rightarrow U^{\otimes N} \rho_N U^{\dagger \otimes N}. \quad (\text{A1})$$

2. Loss channel

A lossy channel absorbs or loses a photon in transmission with probability p . All N photons in a logical qubit state must arrive at the receiver for the state to be successfully transmitted. Under a lossy channel, the state transforms as

$$\rho_N \rightarrow p^N \rho_N + (1 - p^N) \rho_{\perp}. \quad (\text{A2})$$

We define ρ_{\perp} as a state in the subspace in which one or more photons are lost to the channel, and will result in an inconclusive measurement outcome due to loss.

3. Compensation techniques

Compensation techniques are required by protocols that do not have inherent noise-resilience, such as BB84 and TF-QKD. Without stabilisation against channel fluctuations, noise leads to an overwhelming error rate, rapidly rendering key sharing insecure. Compensating noise admits a large resource cost (such as long servo channels and active feedback loops) which limits the practical scalability of real-world implementations of QKD. For example, in TF-QKD experiments, the phase, frequency, and polarisation stabilisation of two sources arriving at a central node from different locations are all necessary. This has been achieved in various ways. For example, frequency locking has been achieved using common laser sources [14, 15]. Polarisation stabilisation was demonstrated using active feedback from the central detectors [9, 11–15]. Phase stabilisation can be implemented using time- and wavelength-multiplexing to estimate phase fluctuations of reference signals [9, 13]. Alternatively, phase fluctuations can be reconciled in post-processing by estimating the phase during reference frame time blocks to correct the phases of quantum frame time blocks [12].

In addition to the physical resources required, stabilisation techniques require continuous monitoring of channel fluctuations. Typical methods involve interleaving data and reference pulses in time [12, 13, 15], or monitoring the QBER using a significant fraction of the sifted shared key [37–39]. These methods reduce the fraction of pulses that can be used to establish a secret key and thus reduce the shared secret key rates.

4. Loss-noise robustness tradeoff

To circumvent the extensive overheads associated with compensating noise fluctuations, encoding inherently noise-resilient states can be considered. Designing a secure QKD scheme requires at least two non-orthogonal states and measurements in their respective bases [48]. Collective unitary noise-robust protocols proposed to date [17–20] use the invariant property of the antisymmetric Bell-state ($|\Psi^-\rangle = \frac{1}{\sqrt{2}}(|0\rangle|1\rangle - |1\rangle|0\rangle)$) under local unitary transformations, i.e., $(U \otimes U)|\Psi^-\rangle = e^{i\Delta}|\Psi^-\rangle$, where Δ is some unobservable U -dependent global phase factor [23]. However, $|\Psi^-\rangle$ is the only two-qubit state satisfying invariance under the action of a collective unitary [49]. Thus, two perfectly noise-cancelling non-orthogonal bases using only two qubits cannot be found. By introducing more qubits into a logical state, noise-robust subspaces of at least dimension 2 can be found. A QKD protocol perfectly noise-cancelling against collective unitary noise can be devised when the logical state contains three or four qubits, as in Ref [18].

Qubits in QKD are typically encoded in photonic degrees of freedom, since photons are natural information carriers [50, 51]. QKD protocols devised with higher noise-robustness thus use more photons per logical state. However, key rate scales exponentially with the channel loss probability of a logical qubit and loss probability scales exponentially with the number of photons (i.e. physical qubits) in the logical state [Eq. (A2)]. Therefore, we arrive at a trade-off between loss- and noise-robustness: increasing the number of physical qubits (i.e. photons) per logical qubit state for the purpose of noise-cancellation leads to an exponential decrease in the key rate for a given transmission distance. We qualitatively illustrate this trade-off in Table I. To overcome this trade-off, we encode a fixed number of photons in a continuous DoF, rather than the tensor product space of many qubit Hilbert spaces, in a conceptually similar manner to bosonic codes [40, 45].

Appendix B: State generation and measurement

Implementing our protocol requires generating antisymmetric Bell-states in frequency bins and time bins, and superpositions of these. Antisymmetric Bell-states in frequency bins can be produced through spontaneous parametric down-conversion [52] or spontaneous four-wave mixing [34], i.e. processes that involve pumping non-linear crystals. Entangled time-bin qubit states can be created using optical switches [53]. However, similarly to frequency-bin states, time-bin Bell-states can also be generated by pumping a domain-engineered non-linear crystal [54, 55] (or by performing quantum optical synthesis in two-dimensional time-frequency space [56]).

By producing the antisymmetric time-bin Bell-state in this way, superpositions of the frequency-bin and time-bin states can be made by coherently pumping crystals with different domain engineering, and implementing a set phase relation between these crystals [57, 58] (see Fig. 7(a)).

Performing measurements in the logical Z_L and X_L bases is a harder challenge to tackle. Here, we outline one possible method for performing the measurements, based on reverse-engineering the state generation process. For example, consider making a measurement to distinguish $|-_L\rangle = 1/\sqrt{2}(|\Psi_f^-\rangle - |\Psi_{\perp f}^-\rangle)$ from $|+_L\rangle = 1/\sqrt{2}(|\Psi_f^-\rangle + |\Psi_{\perp f}^-\rangle)$. To do this, Bob generates the state $|+_L\rangle$ by coherently pumping domain-engineered crystals with the correct relative phase (as proposed above for state preparation). This set-up is aligned such that it has the opposite phase to the incoming signal and thus destructively interferes with the incoming state. If the state $|+_L\rangle$ has been sent by Alice, the two states will destructively interfere [57] and a loss will be measured. If instead the state $|-_L\rangle$ is sent on the set-up generating state $|+_L\rangle$, then part of the amplitude will constructively interfere and photons will be measured at the detector. Therefore, if photons are detected out of the set-up generating the state $|+_L\rangle$, Bob concludes that the state sent was $|-_L\rangle$, whereas if a loss is measured, the result is inconclusive. To make this a balanced measurement, Bob should generate $|+_L\rangle$ only 50% of the time. The other 50% of the time, Bob generates $|-_L\rangle$ to infer if the state $|+_L\rangle$ was sent or not. Identically, this process could be used to perform the Z_L basis measurement. This measurement process works with an incurred 50% loss, thus the key rate is reduced by a factor of a half, but the scaling of key rate with channel loss is identical ($\sim \eta^2$). This measurement scheme is illustrated in Fig. 7(b).

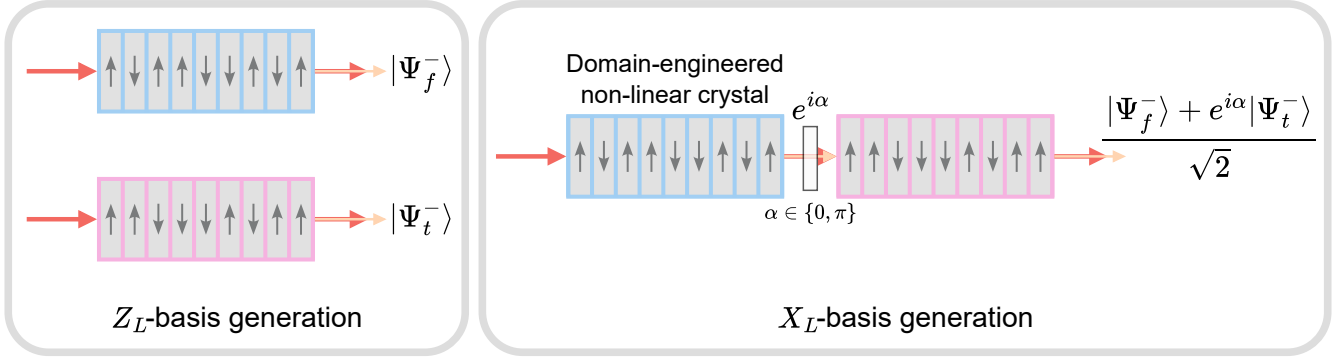
The proposed scheme requires a simple experimental set-up, though is not perfectly faithful to our theoretical model. Specifically, it allows Z_L and X_L basis measurements to be made, but does not distinguish inconclusive outcomes (i.e., the projector $|\perp_L\rangle\langle\perp_L|$) which instead manifest as bit errors for this implementation.

This set-up underscores the experimental feasibility of our protocol. Its simplicity highlights the practical potential for near-term applications. Optimizing this measurement scheme to account for inconclusive outcomes due to noise is beyond the present scope, and would merit a dedicated study. This proposal provides a valuable foundation for further progress towards this goal.

Appendix C: Optimisation of encoding parameters of FBS noise fluctuations

In Fig. 8, we present the fidelity $\mathcal{F}(\Psi_t'^-, \Psi_t^-)$ of a time-bin Bell-state with varying widths, σ_t , under the FBS

a Generation scheme



b Measurement scheme

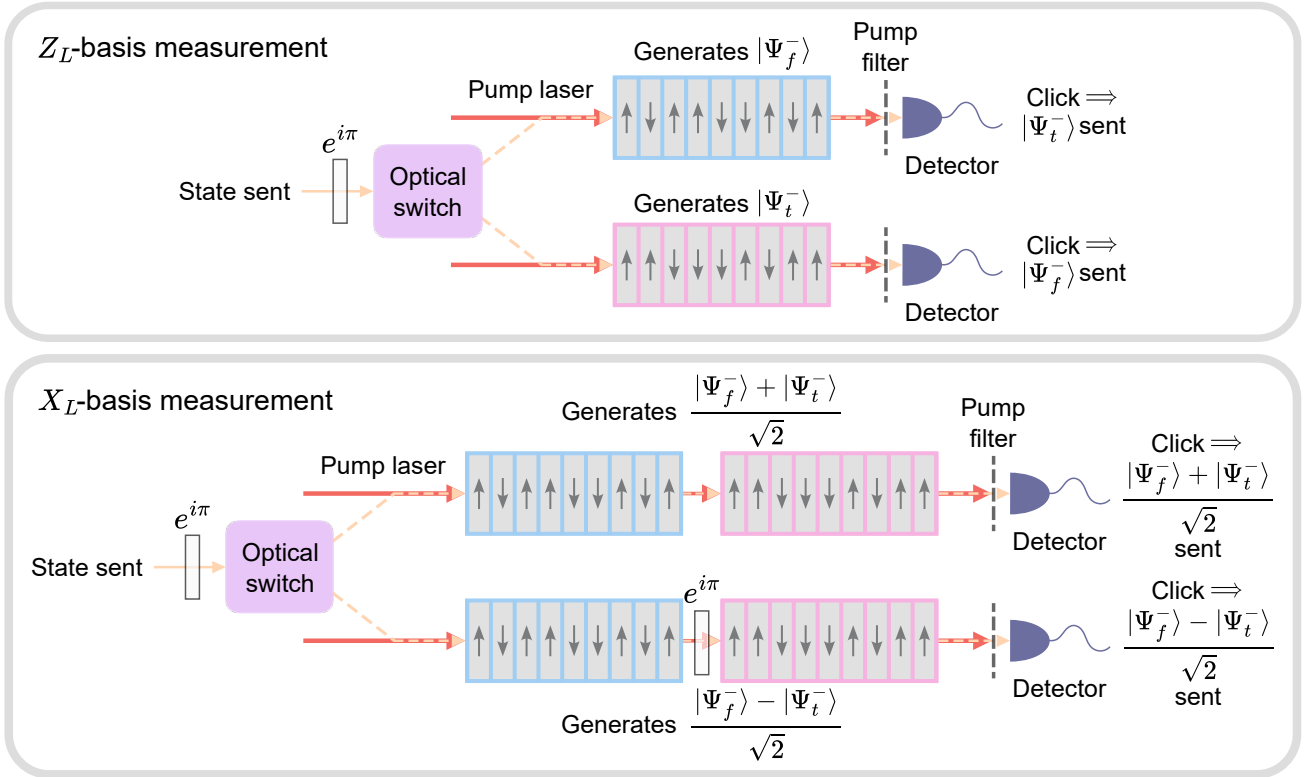


Fig 7. Illustration of the proposed measurement and generation schemes for the logical Z and X basis states. (a) Antisymmetric frequency-bin and time-bin Bell-states can be generated through domain engineering non-linear crystals and pump engineering. Superpositions of the frequency-bin and time-bin antisymmetric Bell-states can be generated by precisely tuning the phase difference α of the pump between the two domain engineered crystals for the time-bin and frequency-bin state. (b) A logical Z basis measurement and logical X basis measurement can be made with a 50% incurred loss, by destructively interfering the incoming states with one of the basis states. An optical switch is used to randomly measure for either the $|0_L\rangle$ or the $|1_L\rangle$ states in the Z_L basis or randomly measure for either the $|+_L\rangle$ or the $|-_L\rangle$ states in the X_L basis. If the incoming state is in the same state as the photon pair being generated, there will be no click at the detector (this cannot be distinguished from channel loss). Conversely, if there is a click at the detector, Bob infers that the state sent by Alice is opposite to the state generated by the detector's associated set-up. (In this figure, we have assumed $\langle \Psi_f^- | \Psi_t^- \rangle \approx 0$.)

for a range of noise bin widths ϵ , and rotation angles θ . By finding the fidelity over a range of FBS variables and varying the Bell-state parameters, this highlights how the encoding can be optimised for robustness to characterised fluctuations in the noise parameters. Here, we observe increasing fidelity over the range of FBS variables given as σ_t decreases. Therefore, for noise fluctuates over the ranges given for ϵ and θ in Fig. 8, σ_t is optimised when it is sufficiently small to ensure the fidelity never falls to zero, giving non-zero key rates without compensation.

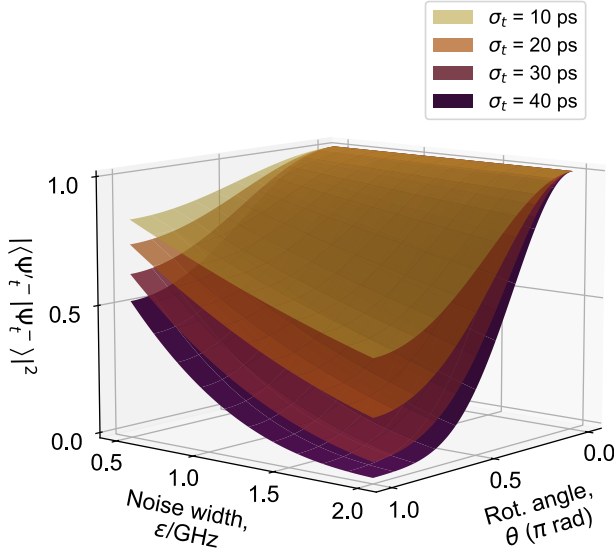


Fig 8. **Robustness of time-bin Bell-states with varying bin width under the FBS noise model, as a function of noise bin width and rotation angle.** Fidelity between the arriving state $|\Psi_t^-\rangle$ sent by Alice through the FBS channel and the state $|\Psi_t^-\rangle$ measured by Bob. The fidelity is plotted as a function of the FBS channel parameters ϵ and θ . For the simulation, we use the time-bin parameters $\tau_0 = 0$ ps, $\tau_1 = 220$ ps, and (values experimentally reported in Ref [33]), with a central frequency assumed at 195.860 THz and varying $\sigma_t = 10, 20, 30, 40$ ps. The fixed FBS noise parameters are $\Omega = 195.860$ THz, $\Omega + \mu = 195.879$ THz, and $\phi = 0$ and varying width $\epsilon = 0.6$ GHz, 3.0 GHz, 6.6 GHz (close to experimentally reported values for a frequency-bin Bell-state encoding in Ref [34], with $\epsilon = 6\sigma_\omega$). The key rate can be optimised by reducing σ_t .

Appendix D: Comparison of our encoding to alternative continuous DoF encoding schemes

Given that the time-bin states are not perfectly robust against the FBS noise model, it is worth comparing our encoding scheme to alternative but similar encodings in the continuous space. The advantage of our protocol is that fewer assumption on the noise model are needed compared to other continuous DoF encodings, whilst still achieving a robust key rate. We highlight this with a

couple of example cases.

Firstly, let us consider instead encoding purely in Bell-states of two pairs of frequency bins, such that $|0_L\rangle = |\Psi_f^-\rangle_{01,AB}$ and $|1_L\rangle = |\Psi_f^-\rangle_{23,AB}$, where $|\Psi_f^-\rangle_{ab,AB} = \frac{|a_f\rangle_A |b_f\rangle_B - |b_f\rangle_A |a_f\rangle_B}{\sqrt{2}}$. $|0_L\rangle$ is thus the antisymmetric frequency-bin Bell-state on modes A and B over frequency-bin states $|0_f\rangle = |\Omega_0\rangle$ and $|1_f\rangle = |\Omega_1\rangle$ and $|1_L\rangle$ is the antisymmetric frequency-bin Bell-state on modes A and B over new frequency-bin states $|2_f\rangle = |\Omega_2\rangle$ and $|3_f\rangle = |\Omega_3\rangle$. To have no logical bit error rate on this basis, this encoding makes the assumption that the FBS acts between states $|0_f\rangle$ and $|1_f\rangle$ and between $|2_f\rangle$ and $|3_f\rangle$ only (or outside of this subspace). If we instead allow the noise to act across these the two frequency-bin Bell-states (e.g. between states $|0_f\rangle$ and $|2_f\rangle$ and between states $|1_f\rangle$ and $|3_f\rangle$), the protocol accrues a bit error rate and an incurred loss at the measurement stage. In contrast, if we allow this model of unitary noise on our proposed encoding (i.e. the FBS noise acting between the encoded frequency bins and frequency bins outside of that space) negligible bit error rate and only an extra loss at measurement is incurred. We quantify this in SM, Sec. S.IX A.

Our chosen encoding also allows us to alleviate another assumption on the noise channel. We assumed in Section II B that the noise acts between frequency bins. By encoding one basis state in frequency bins and one basis state in time bins, we allow the possibility that the noise acts between time bins instead, whilst maintaining the robustness of the encoding. In contrast, the fidelity of the above encoding would degrade more than our proposed encoding. Thus, our encoding is more robust under fewer noise constraints.

If the channel takes the states $|0_f\rangle$ to $|0_t\rangle$ and $|1_f\rangle$ to $|1_t\rangle$, our encoding is no longer robust. In this case however, a simple change in measurement choice at Bob allows for a perfectly noise-robust single-qubit encoding to be appropriate. Designing an encoding robust against such a model is beyond the scope considered in this paper.

Appendix E: BB84 key rate under amplitude damping and decoherence channel

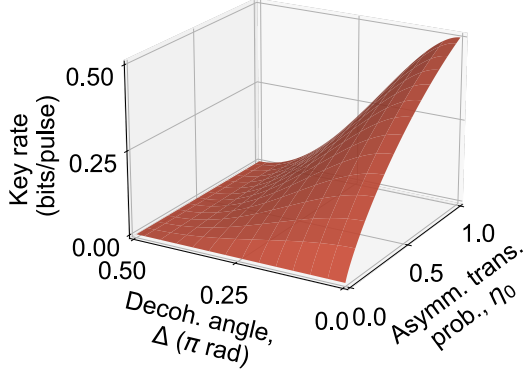
As outlined in Section II B 2, the effect of the FBS (and dispersion – see SM, Sec. S.VIII) on our encoding is equivalent to an amplitude damping and decoherence channel. To simplify the analysis, we make the approximation $\langle \Psi_f^- | \Psi_t^- \rangle = 0$, such that $|1_L\rangle = |\Psi_t^- \rangle$, as justified in Section I and SM, Sec. S.II. The FBS applies a unitary on the frequency-bin qubits, leaving the state $|0_L\rangle = |\Psi_f^- \rangle$ unchanged. Meanwhile, the transformed state $|1_L\rangle$ will have a reduced fidelity and a phase relative to Bob’s measurement states. This amplitude damping

and decoherence channel can be written as

$$|0_L\rangle \rightarrow |0_L\rangle \quad |1_L\rangle \rightarrow \sqrt{\eta_0}e^{i\Delta} |1_L\rangle \quad (\text{E1})$$

where η_0 is the transmission probability of state $|1_L\rangle$ and Δ is the decoherence phase acquired. To analyse the effect of this on key rate, we analyse the key rate of BB84 in an amplitude damping and decoherence channel with η_0 between 0 and 1, and Δ between 0 and $\pi/2$, as shown in Fig. 9. The key rate is mirrored about the $\Delta = \pi/2$ axis for $\pi/2 < \Delta \leq \pi$.

a



b

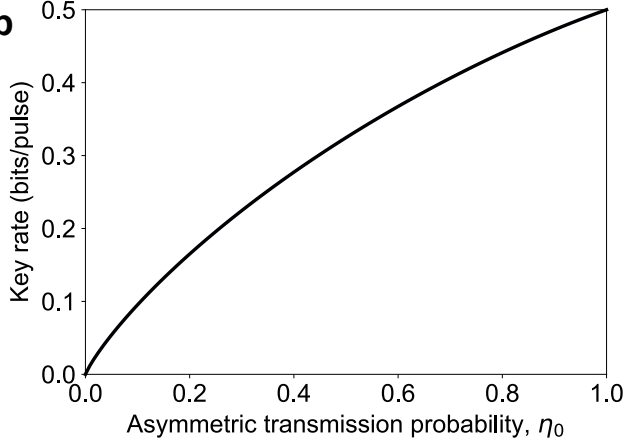


Fig 9. Key rate for BB84 under an amplitude damping and decoherence channel. Our encoding under the FBS operation is a amplitude damping and decoherence channel on the logical qubit state [Eq. (E1)]. (a) Key rate as a function of transmission probability η_0 , and decoherence angle Δ . (b) Key rate as a function of η_0 for fixed $\Delta = 0$. For small Δ , the relation between the key rate and measurement probability is greater than a linear relation, meaning a substantial key rate can be achieved for even a high state-dependent loss.

As seen in Fig. 9(b), the relationship of key rate to the probability of measuring $|1_L\rangle$, η_0 , shows a relationship above linear. This means a significant key rate can be obtained for a highly state-dependent loss.

Supplementary Material

S.I. REVIEW OF COLLECTIVE UNITARY NOISE-ROBUST PROTOCOLS

We provide a brief description of key protocols that are robust to collective unitary noise. In the main text, we studied the schemes in Refs. [17–19], which we will describe here. Further protocols were presented by Sun *et al.* (2009) [21] who made improvements on Cabello (2007) [49]. These methods, however, require more qubits than the ones we analysed, making them far more susceptible to channel loss. Therefore, we present only Refs. [17–19], as the others do not contribute further insights to the discussion. Additionally, we will outline another scheme presented by Guo *et al.* (2020) [20] that requires only two photons for the logical encoding. However, as we will explain, this requires strict assumptions on the noise model, limiting its applicability to real scenarios, and uses a specific photonic encoding that cannot be compared under the FBS model. Hence, we do not analyse it further.

A. Boileau *et al.* (2004)

Two protocols were proposed in Ref. [18] — the first requiring four physical qubits (i.e. photons), and the second requiring only three physical qubits. For the first, Ref. [18] proposed encoding logical states in four-qubit states generated by pairs of antisymmetric Bell-states. By varying the pairing of the four physical qubits (distinguished by a temporal or spatial label, for example), three distinct noise robust states can be generated:

$$|\psi_1\rangle = |\Psi^-\rangle_{12} \otimes |\Psi^-\rangle_{34}, \quad (\text{S1a})$$

$$|\psi_2\rangle = |\Psi^-\rangle_{13} \otimes |\Psi^-\rangle_{24}, \quad (\text{S1b})$$

$$|\psi_3\rangle = |\Psi^-\rangle_{14} \otimes |\Psi^-\rangle_{23}. \quad (\text{S1c})$$

These states perfectly cancel collective unitary noise. Furthermore, these states are mutually-unbiased, i.e., $|\langle\psi_i|\psi_j\rangle| = 1/2$ for $i \neq j$ and thus can be used to generate two non-orthogonal, mutually unbiased bases: a key basis $\{|\psi_1\rangle, |\psi_2\rangle\}$ and a test basis $\{|\psi_2\rangle, |\psi_3\rangle\}$. By measuring the four physical qubits either all in the Z or all in the X basis, randomly, the state sent by Alice can be determined by Bob with a 50% conclusive probability once Alice has announced her basis. The second protocol presented in Ref. [18] uses the same encoding as above, however, Alice discards the fourth qubit (creating mixed states) before sending the state on to Bob.

B. Li *et al.* (2008)

Ref. [19] proposed a modified version of the protocol in Ref. [18], that increases the measurement efficiency by eliminating inconclusive outcomes at Bob. This comes at the cost of offering either rotation-only noise cancellation (independence of θ in the unitary in Eq. (S16) in SM, Sec. S.V) or dephasing-only noise cancellation (independence of ϕ in Eq. (S16) in SM, Sec. S.V) but not the cancellation of a general unitary, as in Ref. [18]. Ref. [19] achieves this by encoding four physical qubits in pairs of rotation-only ($|\Psi^-\rangle, |\Phi^+\rangle$) or dephasing-only ($|\Psi^-\rangle, |\Psi^+\rangle$) noise-cancelling two-qubit states. In the rotation-only noise-robust scheme, the key basis states ($|\Psi_0^{\text{rot}}\rangle, |\Psi_1^{\text{rot}}\rangle$) and the test basis states ($|\Phi_0^{\text{rot}}\rangle, |\Phi_1^{\text{rot}}\rangle$) are given by:

$$|\Psi_0^{\text{rot}}\rangle = |\Phi^+\rangle_{12} \otimes |\Phi^+\rangle_{34}, \quad (\text{S2a})$$

$$|\Psi_1^{\text{rot}}\rangle = |\Psi^-\rangle_{12} \otimes |\Psi^-\rangle_{34}, \quad (\text{S2b})$$

$$|\Phi_0^{\text{rot}}\rangle = |\Phi^+\rangle_{13} \otimes |\Phi^+\rangle_{24}, \quad (\text{S2c})$$

$$|\Phi_1^{\text{rot}}\rangle = |\Psi^-\rangle_{13} \otimes |\Psi^-\rangle_{24}. \quad (\text{S2d})$$

The dephasing-only noise-robust protocol, replaces $|\Phi^+\rangle$ with $|\Psi^+\rangle$.

As in Ref. [18], Bob measures the four physical qubits either all in the Z or all in the X basis randomly. Bob can determine the state sent by Alice perfectly once Alice has announced her basis. The advantage of using this protocol is its efficient encoding scheme which doubles the key rate (see Fig. S10 in SM, Sec. S.VII A) compared to those which discard measurement outcomes due to a mismatch in sent and received bases (BB84) or due to inconclusive outcomes (Ref. [18]). The drawbacks are the more restrictive noise assumptions, and highly loss-dependent key rate.

C. Wang (2005)

In contrast to the use of perfectly noise-cancelling states in Refs. [18, 19], Ref. [17] presented an error rejection scheme that uses fault-tolerant states. Ref. [17] proposed a logical state BB84 protocol, requiring two physical qubits (i.e. photons) per logical state. Here, the logical qubit states are encoded in the two-qubit subspace $\{|01\rangle, |10\rangle\}$. The key basis is given by $\{|01\rangle, |10\rangle\}$, with a computational basis measurement at Bob, and the test basis is given by the Bell-states $\{|\Psi^\pm\rangle = \frac{1}{\sqrt{2}}(|01\rangle \pm |10\rangle)\}$, with a Bell-state measurement at Bob. Unitary rotation noise can push these states outside of the $\{|01\rangle, |10\rangle\}$ two-qubit subspace. At the measurement stage, Alice and Bob discard outcomes corresponding to lying outside of this subspace.

The original version of the protocol is perfectly independent of dephasing-only noise, but not of rotations. Ref. [17] additionally presented a rotation-only noise-robust version of their scheme (similarly to Ref. [19]), at the expense of dephasing robustness. In this, they replace the logical qubit basis with the Bell-states $\{|\Phi^+\rangle, |\Psi^-\rangle\}$. For the logical key basis measurements, both qubits are measured in the Z basis. For the logical test basis, the first qubit is measured in the Z basis, and the second is measured in the X basis, allowing the states to be distinguished. We focus on the dephasing-only version of Ref. [17], since it allows a more clear comparison to the BB84 and our method, which also both show minimal dephasing dependence.

Ref. [17] uses only two photons to encode logical qubits, reducing the susceptibility of the protocol to channel loss compared to Refs. [18, 19]. However, unlike Ref. [18], this does not perfectly cancel the rotation noise. Nonetheless, this scheme is more robust to rotation noise than BB84 (see Fig. 5 in the main text).

D. Guo *et al* (2020)

Ref [20] proposed an efficient protocol robust against collective rotation noise. This is identical to 4-photon scheme in Ref [19], however, it requires only two photons by encoding the physical qubits in hyperentangled orbital angular momentum (OAM) and polarisation states. This requires the assumption that both the OAM and polarisation degrees of freedom experience the same rotation. Whilst this is true for a rotation in free space or for a misalignment of reference frames, this assumption does not hold in general. For example, in optical fibres, birefringence acts only on the polarisation degree of freedom, and thus the OAM modes and polarisation modes will experience different noise [59]. Similarly, astigmatism affects OAM modes, but has no effect on the polarization [59]. Thus, the implementation of this protocol is limited to free space channels, meaning it can be applied to fewer scenarios than Refs [17–19] and our protocol.

S.II. OVERLAP OF ANTISYMMETRIC FREQUENCY-BIN AND TIME-BIN BELL-STATES

Here, we demonstrate that the frequency-bin and time-bin antisymmetric Bell-states can be made perfectly orthogonal.

We start by defining the Gaussian amplitude that we use for the frequency-bin and time-bin states. The state-normalised Gaussian function of the frequency-bin states in the frequency domain is given by

$$f_{\Omega_i, \sigma_\omega}(\omega) = \pi^{-1/4} \sigma_\omega^{-1/2} \exp\left(-\frac{(\omega - \Omega_i)^2}{2\sigma_\omega^2}\right). \quad (\text{S1})$$

and the Fourier transform of the time-bin state-normalised Gaussian functions, such that they can also be represented in the frequency domain, is given by

$$\begin{aligned} F_{\tau_i, \sigma_t}(\omega) &= \frac{1}{\sqrt{2\pi}} \int_{-\infty}^{\infty} dt f_{\tau_i, \sigma_t}(t) e^{-i\omega t} \\ &= \pi^{-1/4} \sigma_t^{1/2} \exp(-i\omega\tau_i) \exp\left(-\frac{\sigma_t^2 \omega^2}{2}\right), \end{aligned} \quad (\text{S2})$$

where ω is defined relative to the central frequency of the time-bin states.

Using the bosonic creation operators defined in Section I of the main text, the time-bin and frequency-bin bi-photon antisymmetric Bell-states can be generally written as

$$|\Psi_x^-\rangle = A(\mu_0, \mu_1, \sigma)(a_{\mu_0, A}^\dagger a_{\mu_1, B}^\dagger - a_{\mu_1, A}^\dagger a_{\mu_0, B}^\dagger) |\emptyset\rangle \quad (\text{S3})$$

$$(\text{S4})$$

where x is f or t and μ_i represents Ω_i for $x = f$ and τ_i for $x = t$. σ is the bin width and $A(\mu_0, \mu_1, \sigma)$ is the normalisation factors for the continuous DoF state, depending on the frequencies and times of the frequency- and time bins defining the qubit and their widths. For the model of Gaussian pulses that we consider above, the normalisation factors are

$$A(\mu_0, \mu_1, \sigma) = \frac{1}{\sqrt{2 \left[1 - \exp \left[-\frac{(\mu_0 - \mu_1)^2}{2\sigma^2} \right] \right]}} \quad (\text{S5})$$

which tend to $\frac{1}{\sqrt{2}}$ when the frequency bins and time bins are sufficiently well separated (i.e. $\mu_1 - \mu_0 \gg \sigma$ such that $\langle 0_x | 1_x \rangle_A \approx 0$), in agreement with Eq. (4) the main text.

Expanding out the expressions for the mode operators and applying the single frequency mode operators to the vacuum state, we can write these states as

$$\begin{aligned} |\Psi_f^-\rangle &= \int_{-\infty}^{\infty} d\omega_1 \int_{-\infty}^{\infty} d\omega_2 \Psi_f^-(\omega_1, \omega_2) |\omega_1\rangle_A |\omega_2\rangle_B \\ &= A(\Omega_0, \Omega_1, \sigma_\omega) \int_{-\infty}^{\infty} d\omega_1 \int_{-\infty}^{\infty} d\omega_2 [f_{\Omega_0, \sigma_\omega}(\omega_1) f_{\Omega_1, \sigma_\omega}(\omega_2) - f_{\Omega_1, \sigma_\omega}(\omega_1) f_{\Omega_0, \sigma_\omega}(\omega_2)] |\omega_1\rangle_A |\omega_2\rangle_B, \end{aligned} \quad (\text{S6})$$

$$\begin{aligned} |\Psi_t^-\rangle &= \int_{-\infty}^{\infty} d\omega_1 \int_{-\infty}^{\infty} d\omega_2 \Psi_t^-(\omega_1, \omega_2) |\omega_1\rangle_A |\omega_2\rangle_B \\ &= A(\tau_0, \tau_1, \sigma_t) \int_{-\infty}^{\infty} d\omega_1 \int_{-\infty}^{\infty} d\omega_2 [F_{\tau_0, \sigma_t}(\omega_1) F_{\tau_1, \sigma_t}(\omega_2) - F_{\tau_1, \sigma_t}(\omega_1) F_{\tau_0, \sigma_t}(\omega_2)] |\omega_1\rangle_A |\omega_2\rangle_B. \end{aligned} \quad (\text{S7})$$

For this, Ω_0 and Ω_1 are defined relative to the central frequency of the time-bin state, such that the frequency variable ω is zero at the central frequency of the time-bin state. Here, we have implicitly defined the bi-photon wavefunctions $\Psi_f^-(\omega_1, \omega_2)$ and $\Psi_t^-(\omega_1, \omega_2)$ of the frequency-bin and time-bin antisymmetric Bell-states, respectively, in the frequency domain.

The overlap between these states can be calculated and is found to be

$$\begin{aligned} \langle \Psi_f^- | \Psi_t^- \rangle &= \int_{-\infty}^{\infty} d\omega_1 \int_{-\infty}^{\infty} d\omega_2 \Psi_f^{-*}(\omega_1, \omega_2) \Psi_t^-(\omega_1, \omega_2) \\ &= A(\Omega_0, \Omega_1, \sigma_\omega) A(\tau_0, \tau_1, \sigma_t) \frac{4\pi\sigma_\omega^2\sigma_t^2}{1 + \sigma_\omega^2\sigma_t^2} \exp \left[-\frac{(\Omega_0^2 + \Omega_1^2)\sigma_t^2 + (\tau_0^2 + \tau_1^2)\sigma_\omega^2}{2(1 + \sigma_\omega^2\sigma_t^2)} \right] \times \\ &\quad \left(\exp \left[-i\frac{\Omega_0\tau_0 + \Omega_1\tau_1}{(1 + \sigma_\omega^2\sigma_t^2)} \right] - \exp \left[-i\frac{\Omega_0\tau_1 + \Omega_1\tau_0}{(1 + \sigma_\omega^2\sigma_t^2)} \right] \right). \end{aligned} \quad (\text{S8})$$

Taking the modulus squared and substituting in the expressions for $A(\Omega_0, \Omega_1, \sigma_\omega)$ and $A(\tau_0, \tau_1, \sigma_t)$, the probability of measuring $|\Psi_f^-\rangle$ given $|\Psi_t^-\rangle$ (or vice versa) is

$$\begin{aligned} |a|^2 = |\langle \Psi_f^- | \Psi_t^- \rangle|^2 &= \frac{1}{\left[1 - \exp \left[-\frac{(\Omega_0 - \Omega_1)^2}{2\sigma_\omega^2} \right] \right]} \frac{1}{\left[1 - \exp \left[-\frac{(\tau_0 - \tau_1)^2}{2\sigma_t^2} \right] \right]} \frac{8\sigma_\omega^2\sigma_t^2}{(1 + \sigma_\omega^2\sigma_t^2)^2} \times \\ &\quad \exp \left[-\frac{(\Omega_0^2 + \Omega_1^2)\sigma_t^2 + (\tau_0^2 + \tau_1^2)\sigma_\omega^2}{(1 + \sigma_\omega^2\sigma_t^2)} \right] \left(1 - \cos \left[\frac{(\Omega_1 - \Omega_0)(\tau_1 - \tau_0)}{(1 + \sigma_\omega^2\sigma_t^2)} \right] \right). \end{aligned} \quad (\text{S9})$$

Thus, if the frequency-bin and time-bin state parameters are selected such that $\frac{(\Omega_1 - \Omega_0)(\tau_1 - \tau_0)}{(1 + \sigma_\omega^2\sigma_t^2)} = 2n\pi$ where $n \in \mathbb{Z}$, the overlap of the time-bin and frequency-bin states is zero, and the states are perfectly orthogonal. If this condition is satisfied, $|\Psi_f^-\rangle$ and $|\Psi_t^-\rangle$ therefore form an orthonormal basis.

We can interpret this conclusion from an intuitive perspective by observing the 2D temporal or frequency spectra of the two states (see Fig. S1). For example, let us observe both states in the frequency domain, as in Figs. S1(b) and (d). By varying the parameters $\Omega_0, \Omega_1, \sigma_\omega$, the peaks of the frequency-bin states can be positioned on the zero points of the time-bin fringes in the frequency domain, resulting in zero overlap and an orthonormal basis. Furthermore, the exponential term in Eq. S9 typically results in only a very small overlap between the two states, meaning $|\Psi_f^-\rangle$ and $|\Psi_t^-\rangle$ are approximately orthonormal in general.

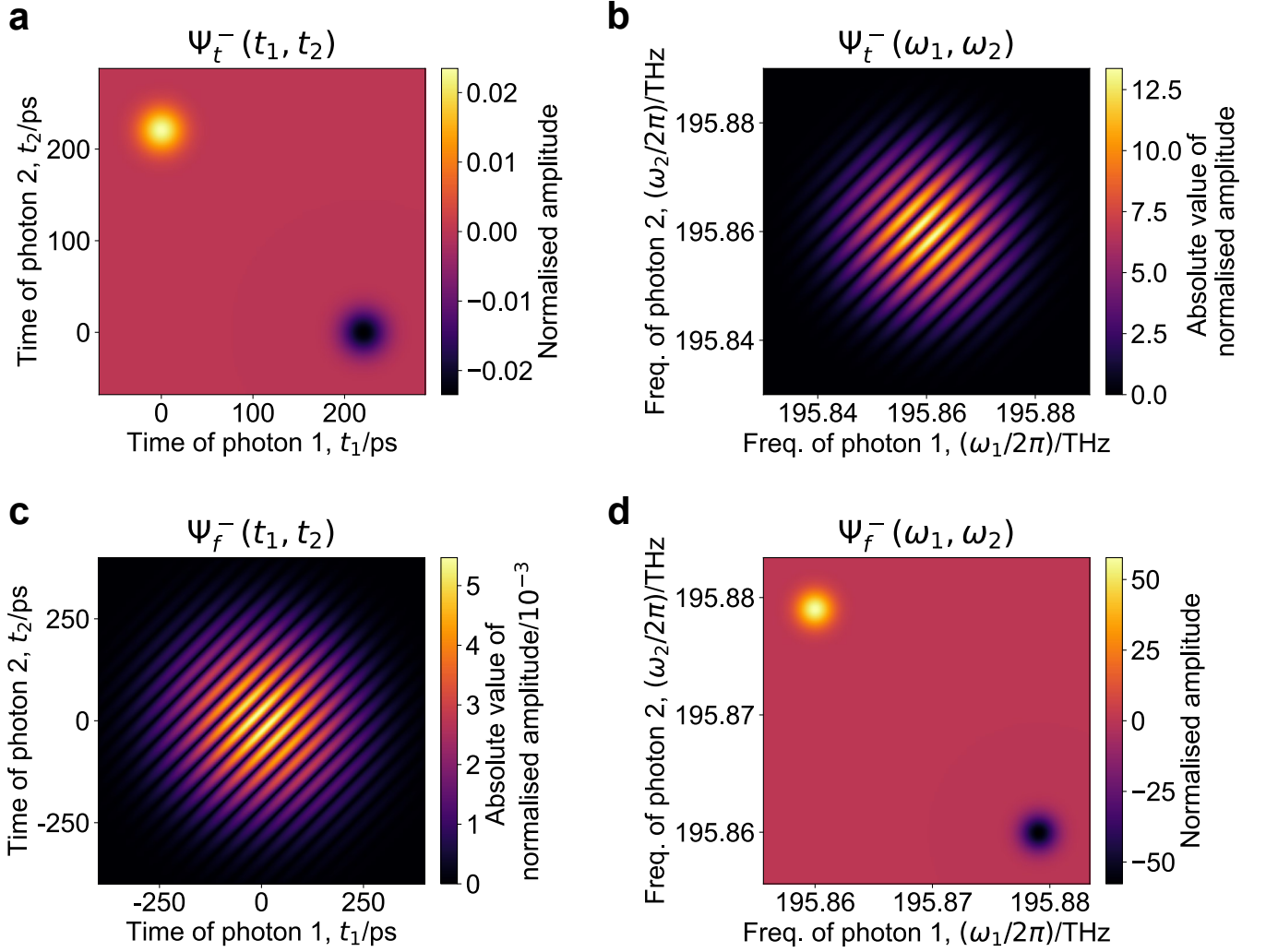


Fig S1. **2D joint temporal and frequency spectra of the time-bin and frequency-bin encoded antisymmetric Bell-states used to form the logical qubit states $|0_L\rangle$ and $|1_L\rangle$ in our encoding.** (a) Normalised bi-photon wavefunction amplitude of the antisymmetric time-bin encoded Bell-state visualised in the time domain, with $\tau_0 = 0$ ps, $\tau_1 = 220$ ps, and $\sigma_t = 17$ ps as in the main text and reported in [33]. (b) Absolute value of the normalised wavefunction of the antisymmetric time-bin encoded Bell-state in (a) visualised in the frequency domain, offset to the Ω_0 of the states in (c) and (d). (c) Absolute value of the normalised bi-photon wavefunction amplitude of the antisymmetric frequency-bin encoded Bell-state visualised in the time domain, with $\Omega_0 = 195.860$ THz, $\Omega_1 = 195.879$ THz, $\sigma_\omega = 1.1$ GHz (as in the main text and close to the experimentally reported values in [34]). (d) Normalised bi-photon wavefunction amplitude of the antisymmetric frequency-bin encoded Bell-state from (c) visualised in the frequency domain.

S.III. CV MODEL OF FBS NOISE ON THE TIME-BIN STATES

We present the mathematical model of the FBS noise model, described in Section II B of the main text. We then use this model to present mathematically the impact of FBS noise on the time-bin states $|\Psi_t^-\rangle$ used in our encoding. We relate this to the effect on our logical qubit encoding by analytically deriving the fidelity of the transformed state with the original time-bin state $|\Psi_t^-\rangle$ and frequency-bin state $|\Psi_f^-\rangle$ which form Bob's measurement basis (corresponding to the logical amplitude damping and bit error rate, respectively) and numerically calculating the global phase acquired by the transformed state (logical state decoherence).

A. Mathematical description of FBS noise model

As described in Section II B of the main text, we assume that the BS acts on bins in the frequency domain that have width ϵ , and frequency separation $\mu(> \epsilon)$, with the central frequency of the first bin at Ω . We assume that the regions outside of the relevant bins are unaffected. Further, we assume that the functions within the bins (in the ranges $\Omega - \epsilon/2 < \omega < \Omega + \epsilon/2$ and $\Omega - \epsilon/2 < \omega < \Omega + \epsilon/2$), become superposed according to the U_{BS} mode operator described in the main text. Thus, the FBS acts a BS operation between single frequency modes at frequencies $\Omega - \epsilon/2$ and $\Omega + \mu - \epsilon/2$ and on each single frequency mode pair (separated by μ) up to the pair $\Omega + \epsilon/2$ and $\Omega + \mu + \epsilon/2$ (Fig. 3 in the main text).

Overall, the action of this noise mathematically takes a general wavefunction $y(\omega)$ to the function $z(\omega)$ according to

$$z(\omega) = \begin{cases} y(\omega) & \omega \leq \Omega - \epsilon/2 \\ \cos \theta y(\omega) - e^{-i\phi} \sin \theta y(\omega + \mu) & \Omega - \epsilon/2 < \omega \leq \Omega + \epsilon/2 \\ y(\omega) & \Omega + \epsilon/2 < \omega \leq \Omega + \mu - \epsilon/2 \\ \cos \theta y(\omega) + e^{i\phi} \sin \theta y(\omega - \mu) & \Omega + \mu - \epsilon/2 < \omega \leq \Omega + \mu + \epsilon/2 \\ y(\omega) & \omega > \Omega + \mu + \epsilon/2. \end{cases} \quad (\text{S1})$$

It would be interesting to extend this to a more general and more physically realised model, in which a smooth tail-off of the frequency noise bins, rather than a discontinuous jump, is considered. This analysis is outside our current focus and is left for subsequent research. However, we predict that a smooth tail-off would have a less degrading effect on the time-bin state, since only a fraction of the original state in the tails would be transformed by the noise.

B. Overlap of transformed time-bin state with original time-bin state

We now derive the effect of this noise on the logical $|1_L\rangle$ state, i.e. the antisymmetric Bell-states in time-bins. We must calculate the fidelity between the transformed (sent by Alice) and original (measured by Bob) states $|\langle \Psi_t'^- | \Psi_t^- \rangle|^2$ (corresponding to amplitude damping on the logical encoding). Similarly, we must deduce the global phase accumulated by the state relative to the measured state under the transformation (corresponding to decoherence on the logical encoding, since $|\Psi_f^- \rangle$ is unaffected by the noise, as explained in the main text). Hence, we derive the overlap function $\langle \Psi_t'^- | \Psi_t^- \rangle$.

In the frequency domain, the antisymmetric time-bin Bell-state is given by

$$\Psi_t^-(\omega_1, \omega_2) = A(\tau_0, \tau_1, \sigma_t) [F_{\tau_0, \sigma_t}(\omega_1) F_{\tau_1, \sigma_t}(\omega_2) - F_{\tau_1, \sigma_t}(\omega_1) F_{\tau_0, \sigma_t}(\omega_2)] \quad (\text{S2})$$

where $F_{\tau_i, \sigma_t}(\omega)$ is defined in Eq. (S2) of the previous section and describes the spectral probability amplitude of a single time-bin qubit state $|i_t\rangle$ (for $i = \{0, 1\}$).

The FBS channel transforms the single qubit states $F_{\tau, \sigma}(\omega)$ into states $G_{\tau, \sigma, \Omega, \mu, \epsilon, \theta, \phi}(\omega)$, as described in Section S.III A, such that

$$G_{\tau, \sigma_t, \Omega, \mu, \epsilon, \theta, \phi}(\omega) = \begin{cases} F_{\tau, \sigma_t}(\omega) & \omega \leq \Omega - \epsilon/2 \\ \cos \theta F_{\tau, \sigma_t}(\omega) - e^{-i\phi} \sin \theta F_{\tau, \sigma_t}(\omega + \mu) & \Omega - \epsilon/2 < \omega \leq \Omega + \epsilon/2 \\ F_{\tau, \sigma_t}(\omega) & \Omega + \epsilon/2 < \omega \leq \Omega + \mu - \epsilon/2 \\ \cos \theta F_{\tau, \sigma_t}(\omega) + e^{i\phi} \sin \theta F_{\tau, \sigma_t}(\omega - \mu) & \Omega + \mu - \epsilon/2 < \omega \leq \Omega + \mu + \epsilon/2 \\ F_{\tau, \sigma_t}(\omega) & \omega > \Omega + \mu + \epsilon/2, \end{cases} \quad (\text{S3})$$

where again, Ω is defined relative to the central frequency of the time-bin state, such that $F_{\tau, \sigma_t}(\omega)$ is centred at $\omega = 0$ THz. The effect of the FBS on a single photon time-bin qubit states in the time domain is visualised in Fig. S2. When the time-bin Bell-state has travelled down the channel, it becomes:

$$\Psi_t'^-(\omega_1, \omega_2) = A(\tau_0, \tau_1, \sigma_t) [G_{\tau_0, \sigma_t, \Omega, \mu, \epsilon, \theta, \phi}(\omega_1) G_{\tau_1, \sigma_t, \Omega, \mu, \epsilon, \theta, \phi}(\omega_2) - G_{\tau_1, \sigma_t, \Omega, \mu, \epsilon, \theta, \phi}(\omega_1) G_{\tau_0, \sigma_t, \Omega, \mu, \epsilon, \theta, \phi}(\omega_2)] \quad (\text{S4})$$

It can be verified that the normalisation factor $A(\tau_0, \tau_1, \sigma_t)$ does not change.

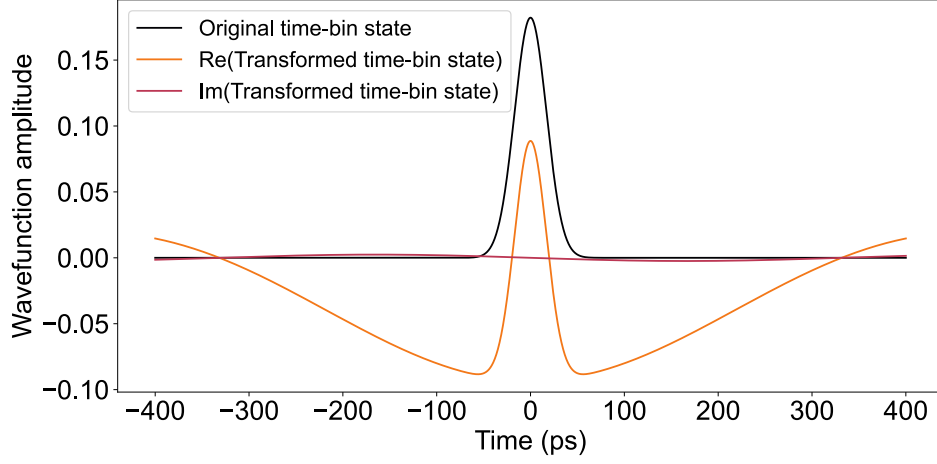


Fig S2. **Effect of the frequency beamsplitter operation on the time-bin state.** The black curve shows the wavefunction as a function of time for the $|0_t\rangle$ time-bin state with $\tau = 0$ ps and $\sigma_t = 17$ ps (with central frequency 194.86 THz). The orange and red curves show the real and imaginary parts respectively of the wavefunction in time for the black state transformed by a frequency beamsplitter operation with noise bins at $\Omega_0 = 195.86$ THz, $\Omega_1 = 195.879$ THz, $\sigma_\omega = 0.5$ GHz, with $\theta = \pi$, $\phi = \pi/2$.

The overlap function $\langle \Psi_t^- | \Psi_t^- \rangle$ therefore depends on the overlap between the transformed and original single qubit states $G_{\tau,\sigma,\Omega,\mu,\epsilon,\theta,\phi}(\omega)$ and $F_{\tau',\sigma}(\omega)$. We calculate explicitly the 1D overlap between these single photon amplitudes to be,

$$\begin{aligned}
& H(\tau, \tau', \sigma, \Omega, \mu, \epsilon, \theta, \phi) \\
&= \int_{-\infty}^{\infty} F_{\tau',\sigma}(\omega)^* G_{\tau,\sigma,\Omega,\mu,\epsilon,\theta,\phi}(\omega) d\omega \\
&= \frac{1}{2} \exp\left(-\frac{(\tau - \tau')^2}{4\sigma^2}\right) \\
&\quad \times \left[\left[2 + \operatorname{erf}\left(\sigma\left(\Omega - \epsilon/2 + \frac{i}{2\sigma^2}(\tau - \tau')\right)\right) - \operatorname{erf}\left(\sigma\left(\Omega + \mu + \epsilon/2 + \frac{i}{2\sigma^2}(\tau - \tau')\right)\right) \right. \right. \\
&\quad \left. \left. + \operatorname{erf}\left(\sigma\left(\Omega + \mu - \epsilon/2 + \frac{i}{2\sigma^2}(\tau - \tau')\right)\right) - \operatorname{erf}\left(\sigma\left(\Omega + \epsilon/2 + \frac{i}{2\sigma^2}(\tau - \tau')\right)\right) \right] \\
&\quad + \cos\theta \left[\operatorname{erf}\left(\sigma\left(\Omega + \epsilon/2 + \frac{i}{2\sigma^2}(\tau - \tau')\right)\right) - \operatorname{erf}\left(\sigma\left(\Omega - \epsilon/2 + \frac{i}{2\sigma^2}(\tau - \tau')\right)\right) \right] \\
&\quad + \cos\theta \left[\operatorname{erf}\left(\sigma\left(\Omega + \mu + \epsilon/2 + \frac{i}{2\sigma^2}(\tau - \tau')\right)\right) - \operatorname{erf}\left(\sigma\left(\Omega + \mu - \epsilon/2 + \frac{i}{2\sigma^2}(\tau - \tau')\right)\right) \right] \\
&\quad - e^{-i\phi} \sin\theta \exp\left(-i\frac{\mu}{2}(\tau + \tau')\right) \exp\left(-\frac{\sigma^2\mu^2}{4}\right) \left[\operatorname{erf}\left(\sigma\left(\Omega + \epsilon/2 + \frac{\mu}{2} + \frac{i}{2\sigma^2}(\tau - \tau')\right)\right) \right. \\
&\quad \left. - \operatorname{erf}\left(\sigma\left(\Omega - \epsilon/2 + \frac{\mu}{2} + \frac{i}{2\sigma^2}(\tau - \tau')\right)\right) \right] \\
&\quad + e^{i\phi} \sin\theta \exp\left(+i\frac{\mu}{2}(\tau + \tau')\right) \exp\left(-\frac{\sigma^2\mu^2}{4}\right) \left[\operatorname{erf}\left(\sigma\left(\Omega + \epsilon/2 + \frac{\mu}{2} + \frac{i}{2\sigma^2}(\tau - \tau')\right)\right) \right. \\
&\quad \left. - \operatorname{erf}\left(\sigma\left(\Omega - \epsilon/2 + \frac{\mu}{2} + \frac{i}{2\sigma^2}(\tau - \tau')\right)\right) \right] \Bigg], \tag{S5}
\end{aligned}$$

where $\operatorname{erf}(z)$ is the error function of the Gaussian integral, defined as,

$$\operatorname{erf}(z) = \frac{2}{\sqrt{\pi}} \int_0^z dx \exp(-x^2). \tag{S6}$$

The total 2D overlap between the transformed and original state is then

$$\begin{aligned} \langle \Psi_t'^- | \Psi_t^- \rangle &= \int_{-\infty}^{\infty} d\omega_1 \int_{-\infty}^{\infty} d\omega_2 \Psi_t'^-(\omega_1, \omega_2)^* \Psi_t^-(\omega_1, \omega_2) \\ &= 2|A(\tau_0, \tau_1, \sigma_t)|^2 [H(\tau_0, \tau_0, \sigma_t, \Omega, \mu, \epsilon, \theta, \phi) H(\tau_1, \tau_1, \sigma_t, \Omega, \mu, \epsilon, \theta, \phi) \\ &\quad - H(\tau_0, \tau_1, \sigma_t, \Omega, \mu, \epsilon, \theta, \phi) H(\tau_1, \tau_0, \sigma_t, \Omega, \mu, \epsilon, \theta, \phi)]. \end{aligned} \quad (\text{S7})$$

This 2D overlap function is complex and 8-variate involving the error function, making it challenging to analyse. Nonetheless, we can draw some general conclusions about the dependence of the measurement probability of the time-bin state on different parameters, which we do in the following section.

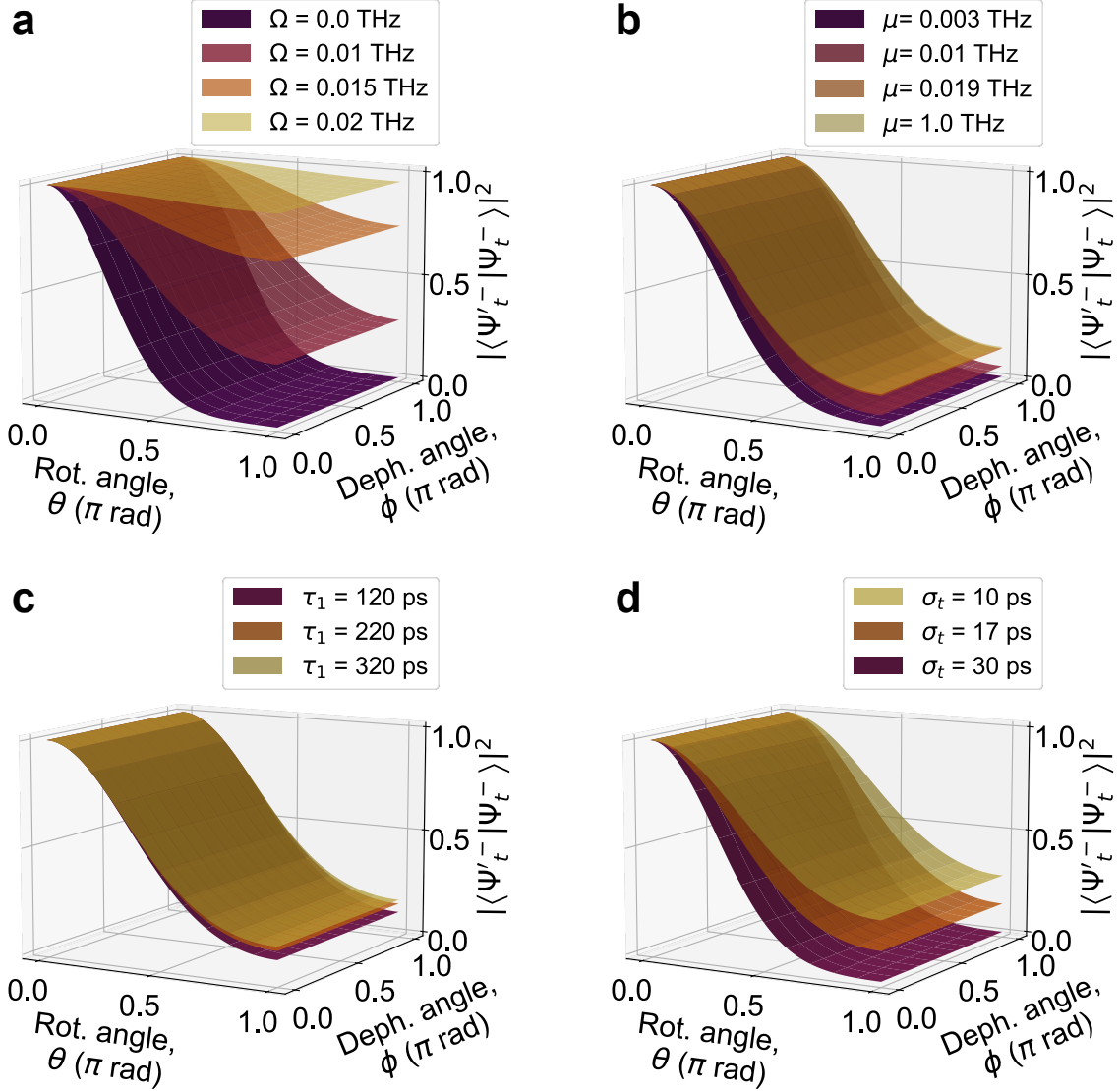


Fig S3. **Robustness of time-bin Bell-state to the frequency beamsplitter operation with different parameters.**

(a) Robustness of the time-bin Bell-state with $\tau_0 = 0$ ps, $\tau_1 = 220$ ps, $\sigma_t = 17$ ps, to a frequency beamsplitter operation $U(\theta, \phi)$ acting on frequency bins with $\epsilon = 6.6$ GHz, a frequency separation of $\mu = 19$ GHz, and varying frequency of the first bin Ω_0 (relative to the central frequency of the time-bin state in frequency), with $\Omega_0 = 0, 10, 15, 20$ GHz. (b) Robustness for $\tau_0 = 0$ ps, $\tau_1 = 220$ ps, $\sigma_t = 17$ ps, with $\epsilon = 3.0$ GHz, $\Omega_0 = 0$ GHz, and varying frequency separation $\mu = 3, 10, 19, 1000$ GHz. (c) Robustness for parameters $\tau_0 = 0$ ps, $\sigma_t = 17$ ps, and varying $\tau_1 = 120, 220, 320$ ps, to the noise parameters $\epsilon = 6.6$ GHz, $\Omega_0 = 0$ GHz, and $\mu = 19$ GHz. (d) Robustness of the time-bin Bell-state with $\tau_0 = 0$ ps, $\tau_1 = 220$ ps, and varying $\sigma_t = 10, 17, 30$ ps to an FBS on bins with $\epsilon = 6.6$ GHz, $\Omega_0 = 0$ GHz, and $\mu = 19$ GHz.

1. Fidelity between arriving and measured time-bin state under the FBS

In Fig. S3, we present the robustness of the time-bin Bell-state to different FBS noise parameters. In Fig. 4 in the main text, and Fig. S3 here, we see that, generally, the time-bin Bell-state robustness to the FBS is approximately independent of the dephasing angle ϕ and dominated by the rotation angle θ of the unitary.

Fig. S3(a) shows that there is a large increase in robustness against noise as the offset of the frequency noise bins from the central frequency of the time-bin increases (i.e. as Ω increases). We can understand this heuristically, as follows. As Ω increases, the noise bins move further into the tails of the time-bin state in the frequency domain. The time-bin wavefunction amplitude is lower in the tails, so the FBS has a smaller effect on the state amplitude.

Fig. S3(b) shows that the robustness generally increases only marginally as the separation between the noise bins μ increases. We can understand this again by relating the gap μ to the “second” noise bin moving further into the tail of the time-bin state. However, since Fig. S3(b) is modelled with the first bin at the central frequency of the time-bin state, the effect of varying μ has a smaller effect on the fidelity than varying Ω (which shifts both of the noise bins). Further, we verify this by noticing that there is negligible effect on the fidelity with θ above $\mu \approx 18$ GHz, which we relate to the second noise bin being far into the time-bin tail where the amplitude is roughly constant, at zero.

We now look at the effect of changing the time-bin Bell-state parameters. Fig. S3(c) shows that the fidelity is barely affected by a changing the delay of the second time-bin relative to the first. This can be understood as τ_1 does not alter the absolute value of the time-bin state in the frequency domain. Changing τ_1 simply varies the phase modulation across the bin in the frequency-bin state.

Finally, Fig. S3(d) shows that the fidelity with θ generally decreases as the time-bin width increases. Increasing the time-bin width makes the corresponding state in the frequency domain narrower. Thus, similarly to the variation of Ω , the amplitude of the state within the noise bins is higher as σ_t increases, resulting in a larger impact on the time-bin states.

2. Phase between arriving and measured time-bin state under the FBS

In Fig. S4, we present the phase accumulated by the time-bin under the FBS noise channel relative to the untransformed basis states for the time-bin Bell-states and noise considered in Fig. 4 of the main text. To find this, we numerically calculate the phase on the 2D overlap function $\langle \Psi_t^- | \Psi_t^- \rangle$, given in Eq. (S7), for varying parameters θ and ϕ .

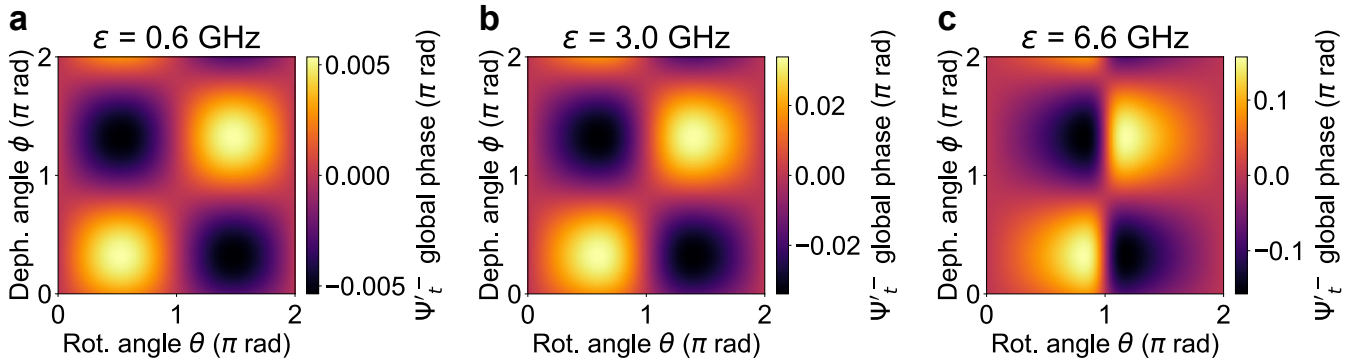


Fig S4. **Accumulated phase on the time-bin Bell-state under the frequency beamsplitter model as a function of θ and ϕ for varying noise bin widths.** The phase accumulated by the antisymmetric time-bin Bell-state Ψ_t^- , with parameters $\tau_0 = 0$ ps, $\tau_1 = 220$ ps and $\sigma_t = 17$ ps, as it traverses the FBS channel with $\Omega = 0$ THz relative to the central frequency of the time-bin state, $\mu = 0.019$ THz and varying noise bin widths (a) $\epsilon = 0.6$ GHz, (b) $\epsilon = 3.0$ GHz, (c) $\epsilon = 6.6$ GHz.

For the parameters used in Fig. S4, we see that the phase shows an oscillating pattern. The maximum value the phase increases as the noise bin width increases for the parameters considered here. However, the maximum phase is only a fraction of $\pi/2$, i.e. the value of phase at which the key rate would fall to zero (Fig. 9 in Appendix E). Therefore, for small values of ϵ , the phase imparted by the FBS has a negligible effect on the overall key rate for given θ and ϕ values.

C. Overlap of transformed time-bin state with frequency-bin state

In the previous subsection, we analysed the action of the FBS on the time-bin Bell-state to find the fidelity between the original and transformed state and the (logical decoherence) phase. We now perform a similar analysis to find the fidelity between the transformed time-bin Bell-state and the frequency-bin Bell-state, $|\langle \Psi_f^- | \Psi_t'^- \rangle|^2$. This gives us the bit error rate of our logical encoding.

To calculate the fidelity, we first find an expression for the 1D overlap between the single photon frequency-bin state centred at frequency Δ (relative to the central frequency of the time-bin state), with the frequency-bin wavefunction given by $f_{\Delta, \sigma_\omega}(\omega)$, as defined in Eq. (S1) in the previous section, and the transformed single photon time-bin state centred at τ , given by $G_{\tau, \sigma, \Omega, \mu, \epsilon, \theta, \phi}(\omega)$ from the previous subsection. We find the 1D overlap function to be

$$\begin{aligned}
I(\Delta, \tau, \sigma_\omega, \sigma_t, \Omega, \mu, \epsilon, \theta, \phi) &= \int_{-\infty}^{\infty} f_{\Delta, \sigma_\omega}(\omega)^* G_{\tau, \sigma_t, \Omega, \mu, \epsilon, \theta, \phi}(\omega) d\omega \\
&= \sqrt{\frac{\sigma_\omega \sigma_t}{2(1 + \sigma_t^2 \sigma_\omega^2)}} \exp\left(-\frac{i\Delta\tau}{1 + \sigma_\omega^2 \sigma_t^2}\right) \exp\left(-\frac{\Delta^2 \sigma_t^2}{2(1 + \sigma_\omega^2 \sigma_t^2)}\right) \exp\left(-\frac{\sigma_\omega^2 \tau^2}{2(1 + \sigma_\omega^2 \sigma_t^2)}\right) \\
&\quad \times \left[\left[2 + \operatorname{erf}\left(\sqrt{\frac{1 + \sigma_t^2 \sigma_\omega^2}{2\sigma_\omega^2}} \left(\Omega - \epsilon/2 + \frac{(i\sigma_\omega^2 \tau + \alpha\sigma_\omega^2 \sigma_t^2 - \Delta)}{1 + \sigma_\omega^2 \sigma_t^2}\right)\right) \right] \right. \\
&\quad - \operatorname{erf}\left(\sqrt{\frac{1 + \sigma_t^2 \sigma_\omega^2}{2\sigma_\omega^2}} \left(\Omega + \mu + \epsilon/2 + \frac{(i\sigma_\omega^2 \tau + \alpha\sigma_\omega^2 \sigma_t^2 - \Delta)}{1 + \sigma_\omega^2 \sigma_t^2}\right)\right) \\
&\quad + \operatorname{erf}\left(\sqrt{\frac{1 + \sigma_t^2 \sigma_\omega^2}{2\sigma_\omega^2}} \left(\Omega + \mu - \epsilon/2 + \frac{(i\sigma_\omega^2 \tau + \alpha\sigma_\omega^2 \sigma_t^2 - \Delta)}{1 + \sigma_\omega^2 \sigma_t^2}\right)\right) \\
&\quad \left. - \operatorname{erf}\left(\sqrt{\frac{1 + \sigma_t^2 \sigma_\omega^2}{2\sigma_\omega^2}} \left(\Omega + \epsilon/2 + \frac{(i\sigma_\omega^2 \tau + \alpha\sigma_\omega^2 \sigma_t^2 - \Delta)}{1 + \sigma_\omega^2 \sigma_t^2}\right)\right) \right] \\
&\quad + \cos\theta \left[\operatorname{erf}\left(\sqrt{\frac{1 + \sigma_t^2 \sigma_\omega^2}{2\sigma_\omega^2}} \left(\Omega + \epsilon/2 + \frac{(i\sigma_\omega^2 \tau + \alpha\sigma_\omega^2 \sigma_t^2 - \Delta)}{1 + \sigma_\omega^2 \sigma_t^2}\right)\right) \right. \\
&\quad \left. - \operatorname{erf}\left(\sqrt{\frac{1 + \sigma_t^2 \sigma_\omega^2}{2\sigma_\omega^2}} \left(\Omega - \epsilon/2 + \frac{(i\sigma_\omega^2 \tau + \alpha\sigma_\omega^2 \sigma_t^2 - \Delta)}{1 + \sigma_\omega^2 \sigma_t^2}\right)\right) \right] \\
&\quad + \cos\theta \left[\operatorname{erf}\left(\sqrt{\frac{1 + \sigma_t^2 \sigma_\omega^2}{2\sigma_\omega^2}} \left(\Omega + \mu + \epsilon/2 + \frac{(i\sigma_\omega^2 \tau + \alpha\sigma_\omega^2 \sigma_t^2 - \Delta)}{1 + \sigma_\omega^2 \sigma_t^2}\right)\right) \right. \\
&\quad \left. - \operatorname{erf}\left(\sqrt{\frac{1 + \sigma_t^2 \sigma_\omega^2}{2\sigma_\omega^2}} \left(\Omega + \mu - \epsilon/2 + \frac{(i\sigma_\omega^2 \tau + \alpha\sigma_\omega^2 \sigma_t^2 - \Delta)}{1 + \sigma_\omega^2 \sigma_t^2}\right)\right) \right] \\
&\quad - e^{-i\phi} \sin\theta \exp\left(-\frac{\Delta\mu\sigma_t^2}{(1 + \sigma_\omega^2 \sigma_t^2)}\right) \exp\left(-\frac{\sigma_t^2 \mu^2 (1 - \sigma_\omega^2 + \sigma_t^2 \sigma_\omega^2)}{2(1 + \sigma_\omega^2 \sigma_t^2)}\right) \exp\left(-\frac{i\mu\tau}{1 + \sigma_\omega^2 \sigma_t^2}\right) \\
&\quad \times \left[\operatorname{erf}\left(\sqrt{\frac{1 + \sigma_t^2 \sigma_\omega^2}{2\sigma_\omega^2}} \left(\Omega + \epsilon/2 + \frac{(i\sigma_\omega^2 \tau + \mu\sigma_\omega^2 \sigma_t^2 - \Delta)}{1 + \sigma_\omega^2 \sigma_t^2}\right)\right) \right. \\
&\quad \left. - \operatorname{erf}\left(\sqrt{\frac{1 + \sigma_t^2 \sigma_\omega^2}{2\sigma_\omega^2}} \left(\Omega - \epsilon/2 + \frac{(i\sigma_\omega^2 \tau + \mu\sigma_\omega^2 \sigma_t^2 - \Delta)}{1 + \sigma_\omega^2 \sigma_t^2}\right)\right) \right] \\
&\quad + e^{i\phi} \sin\theta \exp\left(+\frac{\Delta\mu\sigma_t^2}{(1 + \sigma_\omega^2 \sigma_t^2)}\right) \exp\left(-\frac{\sigma_t^2 \mu^2 (1 - \sigma_\omega^2 + \sigma_t^2 \sigma_\omega^2)}{2(1 + \sigma_\omega^2 \sigma_t^2)}\right) \exp\left(+\frac{i\mu\tau}{1 + \sigma_\omega^2 \sigma_t^2}\right) \\
&\quad \times \left[\operatorname{erf}\left(\sqrt{\frac{1 + \sigma_t^2 \sigma_\omega^2}{2\sigma_\omega^2}} \left(\Omega + \mu + \epsilon/2 + \frac{(i\sigma_\omega^2 \tau - \mu\sigma_\omega^2 \sigma_t^2 - \Delta)}{1 + \sigma_\omega^2 \sigma_t^2}\right)\right) \right. \\
&\quad \left. - \operatorname{erf}\left(\sqrt{\frac{1 + \sigma_t^2 \sigma_\omega^2}{2\sigma_\omega^2}} \left(\Omega + \mu - \epsilon/2 + \frac{(i\sigma_\omega^2 \tau - \mu\sigma_\omega^2 \sigma_t^2 - \Delta)}{1 + \sigma_\omega^2 \sigma_t^2}\right)\right) \right] \Big]. \tag{S8}
\end{aligned}$$

From this, we calculate the total 2D overlap between the transformed time-bin state and the original frequency state measured by Bob. This is given by

$$\begin{aligned}
\langle \Psi_f^- | \Psi_t'^- \rangle &= \int_{-\infty}^{\infty} d\omega_1 \int_{-\infty}^{\infty} d\omega_2 \Psi_f^-(\omega_1, \omega_2) \Psi_t'^-(\omega_1, \omega_2) \\
&= 2A^*(\Omega_0, \Omega_1, \sigma_\omega) A(\tau_0, \tau_1, \sigma_t) [I(\Omega_0, \tau_0, \sigma_\omega, \sigma_t, \Omega, \mu, \epsilon, \theta, \phi) I(\Omega_1, \tau_1, \sigma_\omega, \sigma_t, \Omega, \mu, \epsilon, \theta, \phi) \\
&\quad - I(\Omega_0, \tau_1, \sigma_\omega, \sigma_t, \Omega, \mu, \epsilon, \theta, \phi) I(\Omega_1, \tau_0, \sigma_\omega, \sigma_t, \Omega, \mu, \epsilon, \theta, \phi)].
\end{aligned} \tag{S9}$$

Calculating the modulus-squared value of this expression for different parameters, we find that the bit error probability is typically negligible. For example, in Fig. S5 we show that the bit error rate is $\lesssim 10^{-4}$ for the states and noise considered in Fig. 4 of the main text. Therefore, the impact of bit error on the overall key rate is negligible and outweighed by the effect of amplitude damping.

In Fig. S5, we used $\epsilon = 6\sigma_\omega$ and $\Omega = \Omega_0$, $\Omega_1 - \Omega_0 = \mu$. In this way, we were assuming that the FBS would also be acting a unitary on the frequency-bin Bell-states $|\Psi_f^-\rangle$, if Alice had sent that instead of $|\Psi_t^-\rangle$.

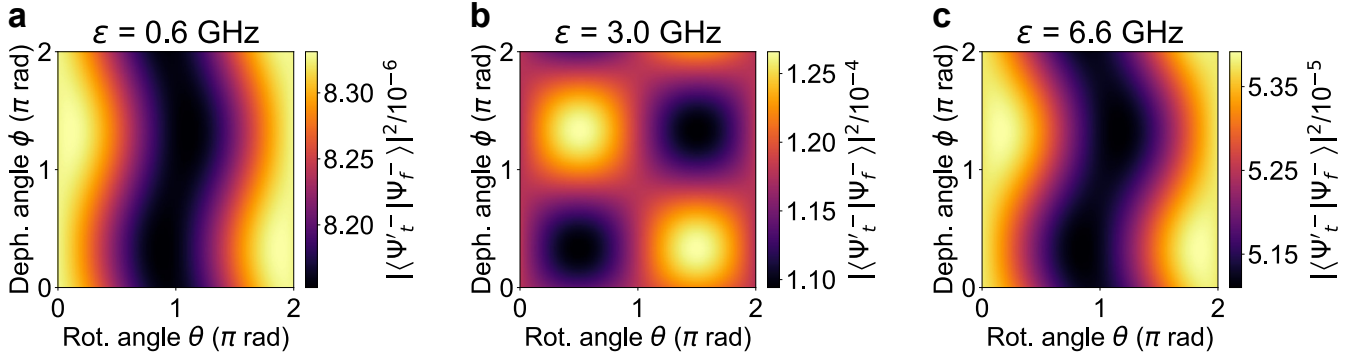


Fig S5. **Bit error rate of the encoding as a function of the beamsplitter channel parameters θ and ϕ for varying noise bin widths.** The bit error rate of our encoding when sending the antisymmetric time-bin Bell-state Ψ_t^- , with parameters $\tau_0 = 0$ ps, $\tau_1 = 220$ ps and $\sigma_t = 17$ ps, sent down a the frequency beamsplitter channel with $\Omega = 0$ THz relative to the central frequency of the time-bin state, $\mu = 0.019$ THz and varying noise bin widths (a) $\epsilon = 0.6$ GHz, (b) $\epsilon = 3.0$ GHz, (c) $\epsilon = 6.6$ GHz. The antisymmetric frequency-bin Bell-state measured here has parameters matching the frequency beamsplitter parameters, i.e. $\Omega_0 = 195.86$ THz (which we take to be the central frequency of the time-bin states), $\Omega_1 = 195.879$ THz, and $\sigma_\omega = \epsilon/6$ for each ϵ .

S.IV. MULTIPLE FBS PAIRS CHANNEL ROBUSTNESS

We extend the FBS model from the previous section further. We now include additional FBS operations acting on frequency bins outside of the $\{|0_f\rangle, |1_f\rangle\}$ basis states. With this, we further probe the robustness of our protocol to an increased level of noise.

For simplicity, let us highlight the new model considering just two pairs of bins, that are ordered in frequency $\Omega_0 < \Omega_1 < \Omega_2 < \Omega_3$ such that a single frequency pair FBS operation acts between Ω_0 and Ω_1 (with $\mu_1 = \Omega_1 - \Omega_0$, width ϵ_1 and θ_1, ϕ_1) and between Ω_2 and Ω_3 (with $\mu_2 = \Omega_3 - \Omega_2$, width ϵ_2 and θ_2, ϕ_2). In this case, we can write the

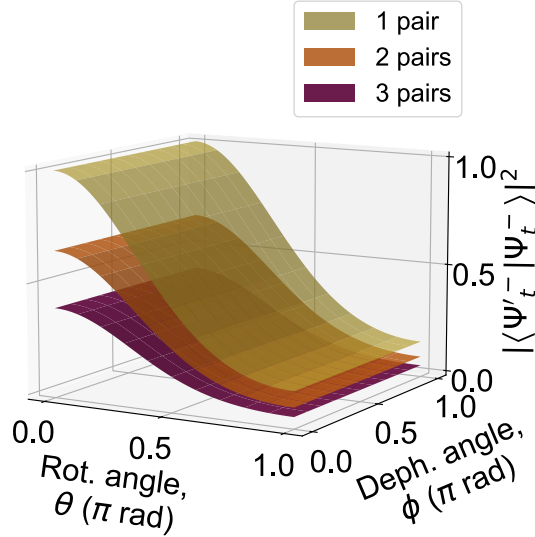


Fig S6. **Robustness of time-bin Bell-states under frequency beamsplitter operation, for varying numbers of operations.** (a) Probability of measuring the state $|\Psi_t^-\rangle$ as a function of unitary parameters θ and ϕ , given the state $|\Psi_t^-\rangle$ with fixed parameters $\tau_0 = 0$ ps, $\tau_1 = 220$ ps, $\sigma_t = 17$ ps (equivalent to the state in Fig. 4 in the main text) was sent down a channel applying a frequency beamsplitter operation $U(\theta, \phi)$ on the frequency bins $\Omega_0 = 195.860$ THz, $\Omega_1 = 195.879$ THz, and varying the width of the frequency bins $\epsilon_1 = 3.0$ GHz (yellow curve) and an additional beamsplitter operation with $\theta = \frac{\pi}{2}$, $\phi = \frac{\pi}{2}$ on the frequency noise bins $\Omega_2 = 195.834$ THz, $\Omega_3 = 195.853$ THz, $\epsilon_2 = 3.0$ GHz (orange curve), and a further additional beamsplitter operation with $\theta = \frac{\pi}{2}$, $\phi = \frac{\pi}{2}$ on the frequency bin $\Omega_4 = 195.867$ THz, $\Omega_5 = 195.866$ THz, $\epsilon_3 = 3.0$ GHz (purple curve).

action of the extended model as taking the general wavefunction $y(\omega)$ to the function $z(\omega)$ according to

$$z(\omega) = \begin{cases} y(\omega) & \omega \leq \Omega_0 - \epsilon_1/2 \\ \cos \theta_1 y(\omega) - e^{-i\phi_1} \sin \theta_1 y(\omega + \mu_1) & \Omega_0 - \epsilon_1/2 < \omega \leq \Omega_0 + \epsilon_1/2 \\ y(\omega) & \Omega_0 + \epsilon_1/2 < \omega \leq \Omega_1 - \epsilon_1/2 \\ \cos \theta_1 y(\omega) + e^{i\phi_1} \sin \theta_1 y(\omega - \mu_1) & \Omega_1 - \epsilon_1/2 < \omega \leq \Omega_1 + \epsilon_1/2 \\ y(\omega) & \Omega_1 + \epsilon_1/2 < \omega \leq \Omega_2 - \epsilon_2/2 \\ \cos \theta_2 y(\omega) - e^{-i\phi_2} \sin \theta_2 y(\omega + \mu_2) & \Omega_2 - \epsilon_2/2 < \omega \leq \Omega_2 + \epsilon_2/2 \\ y(\omega) & \Omega_2 + \epsilon_2/2 < \omega \leq \Omega_3 - \epsilon_2/2 \\ \cos \theta_2 y(\omega) + e^{i\phi_2} \sin \theta_2 y(\omega - \mu_2) & \Omega_3 - \epsilon_2/2 < \omega \leq \Omega_3 + \epsilon_2/2 \\ y(\omega) & \omega > \Omega_3 + \epsilon_2/2. \end{cases} \quad (\text{S1})$$

More generally, we can increase the number of pairs and remove the restriction that they are ordered.

In Fig. S6, we present the effect of this extended noise channel with FBS operations acting across one, two and three different pairs of frequency noise bins on the $|\Psi_t^-\rangle$ state, with the parameters $\theta = \phi = \pi/2$ (equivalent to a bit-flip, Pauli X) for extra FBS pairs. As one could predict, the fidelity $|\langle \Psi_t^- | \Psi_t^- \rangle|^2$ is reduced by the action of these additional operations. However, we see that the fidelity is still greater than zero and non-negligible for a range of rotation and dephasing angles as the number of FBS operations increases. This allows a shared secret key to be established under less restrictive, noisier conditions, highlighting the utility of our scheme.

S.V. SECURITY ANALYSIS METHOD

In this section, we outline the technique used to perform a rigorous security analysis of the protocols considered in the main text (except TF-QKD, for which we used the analytically derived key rates from existing literature [36]). Specifically, the numerical analysis used Version 1 of the Open QKD Security package [35, 60]. First, we rephrase the method from Ref [35] for completeness. We then outline the corresponding mathematical elements of each protocol required to perform this analysis.

A. Security framework

In a typical prepare-and-measure protocol, Alice prepares a state from a set $|\varphi_i\rangle$ with probability p_i , effectively sending a mixed state $\sum_i p_i |\varphi_i\rangle\langle\varphi_i|$ through a quantum channel to Bob, who then measures the incoming state. It is often more convenient to describe this in the *entanglement-based picture*, where Alice prepares instead a purification $|\psi\rangle_{AA'} = \sum_i \sqrt{p_i} |i\rangle_A |\varphi_i\rangle_{A'}$. She then sends the system A' to Bob and measures the system A in the computational basis, thus preparing the state $|\varphi_i\rangle$ when the outcome i is observed. During the transmission over the channel, the system A' is transformed into system B received by Bob, and their shared state is generally mixed, described by ρ_{AB} .

The description of this state contains information about potential tampering on the channel, and the statistics observed by Alice and Bob limit the possible action an eavesdropper could have had. Since the system A is kept securely by Alice and inaccessible to the eavesdropper, Alice's partial state has the additional constraint $\rho_A = \text{tr}_B(\rho_{AB}) = \text{tr}_{A'}(|\psi\rangle\langle\psi|_{AA'})$. Typically, security analyses based on numerical methods consist in an optimisation over all possible bipartite quantum states ρ_{AB} that are compatible with the observed statistics, and maximise the amount of information leaked to an eavesdropper.

Here, we consider the security in the *device-dependent* case, where Alice's and Bob's systems are completely characterised, and the operations they perform are POVMs denoted by P_A^i, P_B^j for Alice and Bob respectively. After the measurement, Alice and Bob assign to each of their outcomes i, j , an announcement value \tilde{a}, \tilde{b} and a secret value \bar{a}, \bar{b} , which are stored respectively in registers $\tilde{A}, \tilde{B}, \bar{A}, \bar{B}$. To simplify the notation, we directly label the measurement operators using the announcement and secret values instead of the outcome index, and we denote them $P_A^{\tilde{a}\bar{a}}, P_B^{\tilde{b}\bar{b}}$.

The action of measuring the system and recording the announcement and secret value in new registers can be seen as a channel $\mathcal{A}(\rho_{AB})$ described by the Kraus operators $K_{\tilde{a}} \otimes K_{\tilde{b}}$, where:

$$K_{\tilde{a}} = \sum_{\bar{a}} \sqrt{P_A^{\tilde{a}\bar{a}}} |\tilde{a}\rangle_{\tilde{A}} |\bar{a}\rangle_{\bar{A}} \quad (\text{S1a})$$

$$K_{\tilde{b}} = \sum_{\bar{b}} \sqrt{P_B^{\tilde{b}\bar{b}}} |\tilde{b}\rangle_{\tilde{B}} |\bar{b}\rangle_{\bar{B}}. \quad (\text{S1b})$$

After each transmission and measurement, Alice and Bob publicly communicate their announcement values. Depending on the announced values, the round may be discarded, for instance if Alice's and Bob's basis choice do not match, or if the outcome measured by Bob is inconclusive. This can be seen as a post-selection map:

$$\Pi = \sum_{(\tilde{a}, \tilde{b}) \in \text{A}} |\tilde{a}\rangle\langle\tilde{a}|_{\tilde{A}} \otimes |\tilde{b}\rangle\langle\tilde{b}|_{\tilde{B}} \otimes \mathbb{I}_{AB\bar{A}\bar{B}}, \quad (\text{S2})$$

where A is the ensemble of accepted announcement values.

The secret key is defined by either Alice or Bob using the publicly available announcement values, and their secret value using a key map. The key map is given by either a function $g(\tilde{a}, \tilde{b}, \bar{a})$ (direct reconciliation) or $g(\tilde{a}, \tilde{b}, \bar{b})$ (reverse reconciliation). The value of the secret bit is written in a register R using the isometry V , where for instance in the case of direct reconciliation:

$$V = \sum_{\tilde{a}\tilde{b}\bar{a}} |g(\tilde{a}, \tilde{b}, \bar{a})\rangle_R \otimes |\tilde{a}\rangle\langle\tilde{a}|_{\tilde{A}} \otimes |\tilde{b}\rangle\langle\tilde{b}|_{\tilde{B}} \otimes |\bar{a}\rangle\langle\bar{a}|_{\bar{A}}. \quad (\text{S3})$$

Then, following again the notation from Ref. [35], we define two quantum channels:

$$\mathcal{G}(\rho_{AB}) = V\Pi\mathcal{A}(\rho_{AB})\Pi V^\dagger, \quad (\text{S4a})$$

$$\mathcal{Z}(\sigma) = \sum_k (|k\rangle\langle k|_R \otimes \mathbb{I}_{A\tilde{A}\bar{A}B\tilde{B}\bar{B}}) \sigma (|k\rangle\langle k|_R \otimes \mathbb{I}_{A\tilde{A}\bar{A}B\tilde{B}\bar{B}}), \quad (\text{S4b})$$

where $\mathcal{Z}(\sigma)$ is a pinching channel and $|k\rangle_R$ is the canonical basis for system R .

Finally, a lower bound on the asymptotic secure key rate is given by

$$\mathcal{D}(\mathcal{G}(\rho_{AB}) || (\mathcal{Z} \circ \mathcal{G})(\rho_{AB})) - p_{\text{concl}} \text{leak}_{EC}, \quad (\text{S5})$$

where $p_{\text{concl}} = \text{tr}(\mathcal{A}(\rho_{AB})\Pi)$ is the conclusive rate of the protocol, leak_{EC} is the amount of information required for error correction in conclusive rounds, and $\mathcal{D}(\rho||\tau)$ is the quantum divergence (also called the Umegaki relative entropy) defined as [61]

$$\mathcal{D}(\rho||\tau) = \text{tr}(\rho \log \rho) - \text{tr}(\rho \log \tau). \quad (\text{S6})$$

While the second half of Eq. (S5) can be computed directly from Alice's and Bob's observed statistics (in this paper, we consider the error correction at the Shannon limit), the first half involves the actual state ρ_{AB} shared between them, which results from the interaction between Alice's prepared state and the communication channel. Since the structure of this state is not known directly, it rather has to be optimised over all possible quantum states compatible with the observed statistics so as to minimise the achievable key rate. The benefit of the formulation of Eq. (S5) is that it corresponds to a convex optimisation problem which can be solved efficiently using well known techniques [62]. Since any solver with a finite precision will eventually return a result which is slightly higher than the true minimum, Ref. [35] also introduced an extra step to convert such a suboptimal solution into a valid lower bound on the key rate using duality arguments.

Using this framework, the security analysis of QKD protocols is reduced to a numerical computation of a lower bound on the achievable secure key rate. For each protocol we are considering in this paper, we simply need to specify the states Alice is preparing ($|\varphi_i\rangle$), the measurements Bob is performing (P_B^{bb}), the post-selection map (Π), the key map ($g(\tilde{a}, \tilde{b}, \tilde{a})$ or $g(\tilde{a}, \tilde{b}, \tilde{b})$) and a reasonable channel model to simulate statistics. In practice, the post-selection map can be included implicitly in the definition of the Kraus operators, or sometimes also in the definition of the key map where values that are not mapped are implicitly discarded. The other quantities are summarised in the next section for each protocol.

B. Protocol description

1. States

Here, we define several states that are useful to describe concisely the protocols under study later on. First, single qubit states are defined in the well known \mathcal{Z} and \mathcal{X} bases as $|0\rangle, |1\rangle$ and $|\pm\rangle = \frac{1}{\sqrt{2}}(|0\rangle \pm |1\rangle)$ respectively.

Next, two-qubit states are constructed similar to a repetition code [63] where the first system corresponds to the reference qubit, and the second system is repeated. The single qubit system can be seen as a physical qubit (i.e. the discrete encoding of a single photon), while any state of more qubits can be seen as the encoding of a single logical qubit. We indicate if the repetition is correct or flipped using a lower-script s_0 , which takes the value of 0 or 1 respectively. Here, we also indicate the number of physical qubits in the logical state (i.e., the number of photons) using a super-script. Note that it is omitted whenever there is only one photon for simplicity. In the \mathcal{Z} basis, this defines the states:

$$|x\rangle_{s_0}^{(2)} = |x\rangle |x + s_0\rangle; x \in \{0, 1\}, s_0 \in \{0, 1\}, \quad (\text{S7})$$

where the addition between binary digits x and s_0 is taken modulo 2.

Similarly, the \mathcal{X} basis states are defined after performing a Hadamard on the \mathcal{Z} basis states:

$$|+\rangle_{s_0}^{(2)} = (H \otimes H) |0\rangle_{s_0}^{(2)} \quad (\text{S8})$$

$$|-\rangle_{s_0}^{(2)} = (H \otimes H) |1\rangle_{s_0}^{(2)} \quad (\text{S9})$$

Then, we define logical states made of four physical qubits as a repetition of two-qubit states. Hence, the way the states are defined can be seen as a concatenation of repetition codes. We keep track of the *syndrome* of the code, i.e. whether the repeated bit is correct or flipped, at each stage. The first bit of the syndrome corresponds to a flip in the inner two-qubit logical state encoding, while the second bit corresponds to a flip in the outer logical encoding.

In the \mathcal{Z} basis, this defines the following states:

$$|x\rangle_{s_0 s_1}^{(4)} = |x\rangle_{s_0}^{(2)} |x + s_1\rangle_{s_0}^{(2)}; x \in \{0, 1\}, s = s_0 s_1 \in \{00, 01, 10, 11\} \quad (\text{S10})$$

and similarly for states in the \mathcal{X} basis. Here the basis change is at the level of the physical qubit and not at the level of the logical qubit, e.g. $|+\rangle_0^{(2)} = |++\rangle \neq \frac{1}{\sqrt{2}}(|0\rangle_0^{(2)} + |1\rangle_0^{(2)})$. In the rest of this section, we denote the syndrome by $s = s_0 s_1$, taking values in the ensemble $\{00, 01, 10, 11\}$, or equivalently if written in decimal $\{0, 1, 2, 3\}$.

In some of the protocols under study, the information is encoded in the syndrome rather than in the value of the reference bit. Therefore, it is more convenient to consider the following states:

$$|s\rangle_{\mathcal{Z}}^{(4)} = \frac{1}{\sqrt{2}}(|0\rangle_s^{(4)} + |1\rangle_s^{(4)}), \quad (\text{S11})$$

$$|s\rangle_{\mathcal{X}}^{(4)} = \frac{1}{\sqrt{2}}(|+\rangle_s^{(4)} + |-\rangle_s^{(4)}). \quad (\text{S12})$$

\tilde{a}	\bar{a}	BB84	Our prot.	Wang	Boileau (4 photons)	Li (dephasing)	Li (rotation)
0	0	$ 0\rangle$	$ 0_L\rangle$	$ 10\rangle$	$\frac{1}{\sqrt{2}}(2\rangle_{\mathcal{Z}}^{(4)} - 3\rangle_{\mathcal{Z}}^{(4)})$	$\frac{1}{\sqrt{2}}(0\rangle_{\mathcal{X}}^{(4)} - 1\rangle_{\mathcal{X}}^{(4)})$	$\frac{1}{\sqrt{2}}(0\rangle_{\mathcal{Z}}^{(4)} + 1\rangle_{\mathcal{Z}}^{(4)})$
0	1	$ 1\rangle$	$ 1_L\rangle$	$ 01\rangle$	$\frac{1}{\sqrt{2}}(1\rangle_{\mathcal{Z}}^{(4)} - 3\rangle_{\mathcal{Z}}^{(4)})$	$\frac{1}{\sqrt{2}}(2\rangle_{\mathcal{X}}^{(4)} - 3\rangle_{\mathcal{X}}^{(4)})$	$\frac{1}{\sqrt{2}}(2\rangle_{\mathcal{Z}}^{(4)} - 3\rangle_{\mathcal{Z}}^{(4)})$
1	0	$ +\rangle$	$ +_L\rangle$	$ \psi^+\rangle$	$\frac{1}{\sqrt{2}}(1\rangle_{\mathcal{Z}}^{(4)} - 3\rangle_{\mathcal{Z}}^{(4)})$	$\frac{1}{\sqrt{2}}(0\rangle_{\mathcal{X}}^{(4)} - 2\rangle_{\mathcal{X}}^{(4)})$	$\frac{1}{\sqrt{2}}(0\rangle_{\mathcal{Z}}^{(4)} + 2\rangle_{\mathcal{Z}}^{(4)})$
1	1	$ -\rangle$	$ -_L\rangle$	$ \psi^-\rangle$	$\frac{1}{\sqrt{2}}(2\rangle_{\mathcal{Z}}^{(4)} - 1\rangle_{\mathcal{Z}}^{(4)})$	$\frac{1}{\sqrt{2}}(1\rangle_{\mathcal{X}}^{(4)} - 3\rangle_{\mathcal{X}}^{(4)})$	$\frac{1}{\sqrt{2}}(1\rangle_{\mathcal{Z}}^{(4)} - 3\rangle_{\mathcal{Z}}^{(4)})$

TABLE S1. **Prepared states and Alice’s information.** All states are prepared with uniform probability, and for each state, Alice records the associated announcement value \tilde{a} and secret value \bar{a} .

For each protocol under study in this paper, we summarise Alice’s prepared states and associated announcement and secret values in Table S1. The 3-photon version of the protocol in Ref. [18] is obtained by tracing out the fourth photon of the 4-photon scheme, which corresponds to Alice preparing mixed states. In the implementation, we consider instead a purification of these mixed states by duplicating each signal state with an extra qubit register, and assigning each purified state to the same announcement and secret value.

2. Measurement

Typically, Bob’s measurement is designed to discriminate which state Alice prepared, possibly with some inconclusive outcome. Here, it is essentially composed of projectors onto the states that Alice prepared, or states related to them.

We define a few additional four-photon projectors:

$$\Pi_{s,\mathcal{Z}} = |0\rangle\langle 0|_s^{(4)} + |1\rangle\langle 1|_s^{(4)} \quad (\text{S13})$$

$$\Pi_{s,\mathcal{X}} = |+\rangle\langle +|_s^{(4)} + |-\rangle\langle -|_s^{(4)} \quad (\text{S14})$$

They are used to discriminate the states $|s\rangle_{\mathcal{Z}}$ and $|s\rangle_{\mathcal{X}}$ respectively. Those are not projectors onto these states though, but rather a pinched version since the coherence terms are missing. They are easier to implement as they are composed only of \mathcal{Z} or \mathcal{X} basis measurements on the physical qubits.

We assume that a photon loss can always be detected at the receiver, which will output a special “no-click” character, \emptyset . This is a common approach (see for instance Refs. [35, 64], which are based on an argument from Ref. [65]), and it is modelled by considering that the channel is moving the signal state onto a dimension $|\perp\rangle$, orthogonal to the signal space. In practice, it means that all POVM matrices are defined with an extra dimension to account for the no-click outcome. For instance in a qubit protocol (where \oplus represents here the direct sum of vectors) :

$$|+\rangle\langle +| \oplus 0 = \frac{1}{2} \begin{pmatrix} 1 & 1 & 0 \\ 1 & 1 & 0 \\ 0 & 0 & 0 \end{pmatrix}, \text{ and the projector } |\perp\rangle\langle \perp| = \begin{pmatrix} 0 & 0 & 0 \\ 0 & 0 & 0 \\ 0 & 0 & 1 \end{pmatrix} \text{ reads the orthogonal dimension to determine if a}$$

no-click event has occurred. We use the same notation $|\perp\rangle\langle \perp|$ for the loss outcome in all the protocols under study to keep the notation simple, even though the dimension of the actual operator is not always the same, and depends on the dimension of the signal space.

For each protocol under study, we summarise Bob’s measurement operators and associated announcement value and secret value in Table S2. The 3-photon version of the protocol in Ref. [18] is obtained by removing the measurement on the fourth system of the 4-photon scheme, all the POVMs are otherwise identical.

3. Key map

Usually, writing the key map is straightforward for most protocols. This is the case for instance for the BB84 protocol where the secret bit is usually defined to be Alice’s secret value whenever the announcement values match. This corresponds to Bob trying to guess Alice’s secret bit with his measurement whenever their basis choices match. However here, in the four-photon protocols under study, it is actually easier to define the key map from Bob’s perspective. This is because the information encoded in Alice’s states seems to be in the syndrome of the logical encoding, rather than only in either her secret bit or basis choice. As a result, it is only after Bob records his outcome and relates it to Alice’s announcement value that the round can be classified as conclusive or inconclusive.

\tilde{b}	\bar{b}	BB84	Our protocol	Wang	Boileau, Li (dephasing, rotation)
0	0	$\frac{1}{2} 0\rangle\langle 0 $	$\frac{1}{2} 0_L\rangle\langle 0_L $	$\frac{1}{2} 10\rangle\langle 10 $	$\frac{1}{2}\Pi_{0,\mathcal{Z}}$
0	1	$\frac{1}{2} 1\rangle\langle 1 $	$\frac{1}{2} 1_L\rangle\langle 1_L $	$\frac{1}{2} 01\rangle\langle 01 $	$\frac{1}{2}\Pi_{1,\mathcal{Z}}$
0	2	N/A	N/A	N/A	$\frac{1}{2}\Pi_{2,\mathcal{Z}}$
0	3	N/A	N/A	N/A	$\frac{1}{2}\Pi_{3,\mathcal{Z}}$
1	0	$\frac{1}{2} +\rangle\langle + $	$\frac{1}{2} +_L\rangle\langle +_L $	$\frac{1}{2} \psi^+\rangle\langle \psi^+ $	$\frac{1}{2}\Pi_{0,\mathcal{X}}$
1	1	$\frac{1}{2} -\rangle\langle - $	$\frac{1}{2} -_L\rangle\langle -_L $	$\frac{1}{2} \psi^-\rangle\langle \psi^- $	$\frac{1}{2}\Pi_{1,\mathcal{X}}$
1	2	N/A	N/A	N/A	$\frac{1}{2}\Pi_{2,\mathcal{X}}$
1	3	N/A	N/A	N/A	$\frac{1}{2}\Pi_{3,\mathcal{X}}$
2	0	N/A	N/A	$ 00\rangle\langle 00 + 11\rangle\langle 11 $	rest
3	0	$ \perp\rangle\langle \perp $	$ \perp\rangle\langle \perp $	$ \perp\rangle\langle \perp $	$ \perp\rangle\langle \perp $

TABLE S2. **Bob’s measurement and information.** For each measurement, Bob records the announcement value \tilde{b} and secret value \bar{b} associated with the outcome. The announcement $\tilde{b} = 2$ always corresponds to inconclusive rounds, while other values may correspond to conclusive or inconclusive rounds depending on the protocol. The key map defined in Table S3 clarifies which sets of values $(\tilde{a}, \tilde{b}, \bar{b})$ correspond to conclusive rounds. The notation “rest” indicates any other operator such that overall the sum of all operators is identity as to define a valid measurement.

r	0	1
BB84	(0, 0, 0), (1, 1, 0)	(0, 0, 1), (1, 1, 1)
Our protocol	(0, 0, 0), (1, 1, 0)	(0, 0, 1), (1, 1, 1)
Wang	(0, 0, 0), (1, 1, 0)	(0, 0, 1), (1, 1, 1)
Boileau	(0, 0, 2), (0, 1, 2) (1, 0, 3), (1, 1, 3)	(0, 0, 1), (0, 1, 1) (1, 0, 2), (1, 1, 2)
Li (dephasing)	(0, 1, 0), (0, 1, 1) (1, 1, 0), (1, 1, 2)	(0, 1, 2), (0, 1, 3) (1, 1, 1), (1, 1, 3)
Li (rotation)	(0, 0, 0), (0, 0, 1), (0, 1, 0), (0, 1, 1), (1, 0, 0), (1, 0, 2), (1, 1, 0), (1, 1, 2)	(0, 0, 2), (0, 0, 3) (0, 1, 2), (0, 1, 3) (1, 0, 1), (1, 0, 3) (1, 1, 1), (1, 1, 3)

TABLE S3. **Key map** $r = g(\tilde{a}, \tilde{b}, \bar{b})$. This defines the secret bit from the announcement values and Bob’s secret value.

In Table S3, we summarise all the possible values of $(\tilde{a}, \tilde{b}, \bar{b})$ resulting in a value $r = 0$ or $r = 1$. Any other combination is implicitly assumed to be inconclusive. The classical reconciliation (error correction and privacy amplification) is then performed between the classical registers R for Bob and \bar{A} for Alice.

C. Channel models

The FBS channel acts as a unitary operation on frequency-bin encoded qubits. To analyse the collective unitary noise-robust protocols [17–19] (given in Sec. S.I of the SM) when encoded in frequency-bins, we use the noise models outlined in Appendix A. Combining both the collective unitary noise channel and the loss channel from Appendix A, the general model used is given by

$$\rho_N \rightarrow p^N U^{\otimes N} \rho_N U^{\dagger \otimes N} + (1 - p^N) \rho_{\perp}, \quad (\text{S15})$$

where ρ_{\perp} is the state that gives an inconclusive outcome due to loss, p is the single photon loss probability, and N is the number of photons in the logical state ρ_N . Here U is some unknown unitary, parameterised by the FBS noise parameters θ and ϕ as

$$U = \begin{pmatrix} \cos \theta & -e^{-i\phi} \sin \theta \\ e^{i\phi} \sin \theta & \cos \theta \end{pmatrix}. \quad (\text{S16})$$

Here we have defined U only over the space that does not result in a conclusive outcome (i.e., does not include the dimension for $|\perp\rangle$). An extra row and column is added to the operation $U^{\otimes N}$ to account for this additional dimension.

For our protocol, the FBS channel imparts an amplitude damping and decoherence operation on the states (outlined in Appendix E), rather than a collective unitary operation of the form U from the previous equation. The general channel model used to analyse our protocol thus takes the form

$$\rho \rightarrow p^2(E_0\rho E_0^\dagger + E_1\rho E_1^\dagger) + (1 - p^2)\rho_\perp \quad (\text{S17})$$

where E_0 and E_1 are the channel Kraus operators given by

$$E_0 = \begin{pmatrix} 0 & 0 & 0 \\ 0 & 0 & 0 \\ 0 & \sqrt{1-\eta_0} & 0 \end{pmatrix} \quad E_1 = \begin{pmatrix} 1 & 0 & 0 \\ 0 & \sqrt{\eta_0}e^{i\Delta} & 0 \\ 0 & 0 & 1 \end{pmatrix}. \quad (\text{S18})$$

η_0 and Δ are the amplitude damping and decoherence parameters outlined in Appendix E. The Kraus operators are 3×3 , with the dimensions corresponding to the $|0_L\rangle, |1_L\rangle$ states, and the inconclusive state $|\perp\rangle$, respectively. Thus, the state ρ_\perp now corresponds to the that that gives an inconclusive outcomes due to both loss and noise operations leading to leakage from the logical subspace. The squared factor on the loss probability corresponds to our logical states being encoded in two photons.

S.VI. KEY RATE DEPENDENCE OF OUR PROTOCOL ON ϕ

In Fig. S7, we present the key rate of our protocol under the FBS channel for the full range of rotation angles θ and dephasing angles ϕ . We observe that there is negligible dependence on ϕ for the parameters shown. Hence, the key rate can be most easily analysed for the parameters chosen by considering a fixed ϕ and varying θ only, as in the main text.

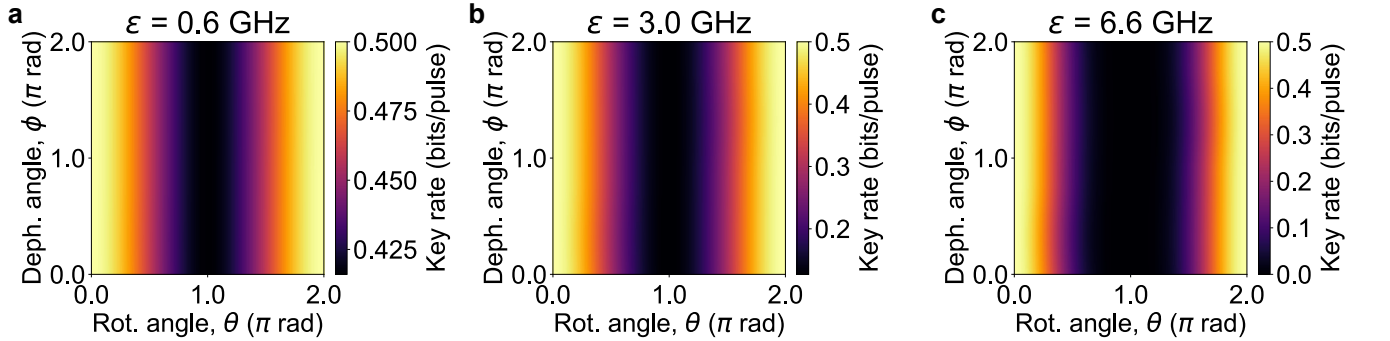


Fig S7. **Key rate of our protocol under FBS channel with rotation angle θ and dephasing angle ϕ .** Key rate of our encoding for unitary parameters θ and ϕ for varying FBS noise bin width, ϵ , for (a) $\epsilon = 0.01 \times \frac{1}{\sigma_t} = 0.6$ GHz, (b) $\epsilon = 0.05 \times \frac{1}{\sigma_t} = 3.0$ GHz, and (c) $\epsilon = 0.11 \times \frac{1}{\sigma_t} = 6.6$ GHz. The other parameters match those of Fig. 4 in the main text, i.e. the encoding parameters are $\tau_0 = 0$ ps, $\tau_1 = 220$ ps, and $\sigma_t = 17$ ps, with a central frequency of 195.860 THz, and FBS noise parameters $\Omega = 195.860$ THz, $\Omega + \mu = 195.879$ THz.

As also shown in Fig. 5 of the main text, the smaller the value of ϵ , the larger the lower bound on key rate across the range θ (found for $\theta = \pi$).

S.VII. KEY RATES OF DV-ENCODED PROTOCOLS

In this section, we discuss the key rates presented in Figs. 5 and 6 in the main text for the existing collective unitary noise-robust protocols in Refs. [17–19] and BB84 [1]. Further, we provide additional figures of the noise resilience of these protocols over unitary channels including dephasing angle ϕ dependence, and present the security of Ref. [19] under a loss-only channel. Further, we compare the key rate to the rates predicted within their work.

A. Key rates in collective unitary channels of BB84 and Wang

Ref [17] demonstrated that their encoding was perfectly robust against dephasing-only (ϕ) noise and outlined its increased robustness to rotation noise (θ) in terms of bit error rates. They showed that the bit error rate goes as $\sin^2 \theta / (\cos^4 \theta + \sin^4 \theta)$, compared to $\sin^2 \theta$ for BB84. From Fig. S9, we see that Ref [17] is indeed perfectly resilient to dephasing-only noise, demonstrated by the independence of the key rate on ϕ . As shown in Fig. 5 in the main text, the key rate of Ref [17] shows a trend matching that predicted by the simple bit error rate analysis. The key rate for BB84 is lower than the key rate for Ref [17] for all θ parameters, thus demonstrating the predicted improvement.

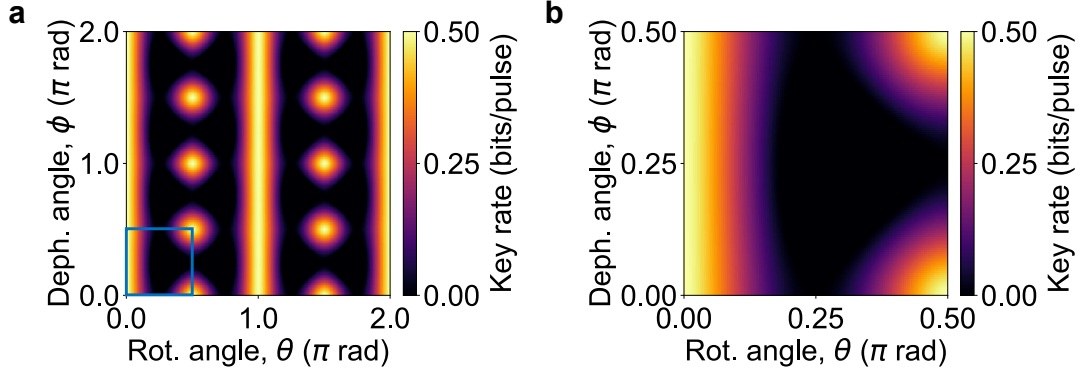


Fig S8. **Key rate of BB84 under a collective unitary channel with rotation angle θ and dephasing angle ϕ .** Key rate of BB84 for unitary parameters θ and ϕ over range (a) $[0, 2\pi)$ and (b) $[0, \pi/2)$. The key rate is symmetric (mirrored) about the $\pi/2$ line and about π in both θ and ϕ . The blue square in (a) highlights the range of the simulation covered in (b).

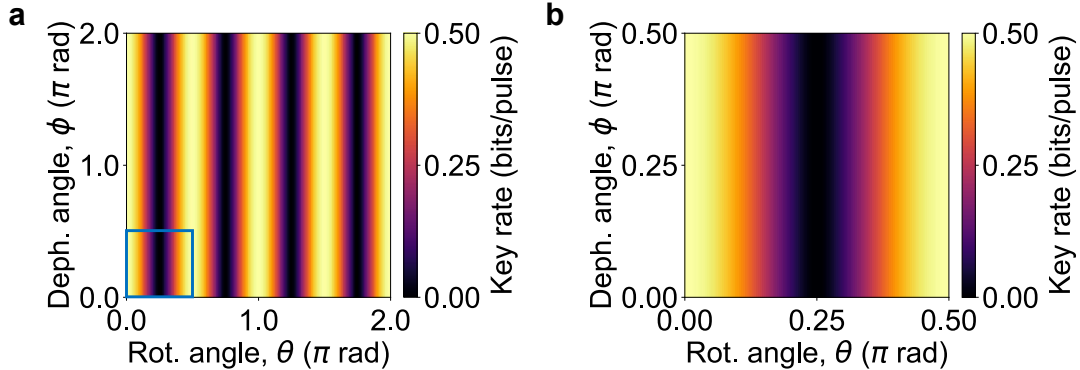


Fig S9. **Key rate of Wang (2005) [17] under a collective unitary channel with rotation angle θ and dephasing angle ϕ .** Key rate of Ref. [17] for unitary parameters θ and ϕ over range (a) $[0, 2\pi)$ and (b) $[0, \pi/2)$. This is symmetric (mirrored) about the $\pi/2$ line and about π in both θ and ϕ . Further, the key rate is independent of the dephasing angle ϕ . The blue square in (a) indicates the range of the simulation for (b).

For $0 < \theta < \pi/4$ and $3\pi/4 < \theta < \pi$, for both BB84 and Ref. [17], Alice and Bob's outcomes are correlated. For $\pi/4 < \theta < 3\pi/4$, before post-processing, Alice and Bob's outcomes will be anticorrelated. In post-processing, the bit value is flipped so that Alice and Bob have matching bits. However, it is this effect that gives rise to the zero key rate when θ is not constant but allowed to vary over its full range (Sec. II A in the main text), as would be expected experimentally without stabilisation techniques.

B. Key rate comparison of the 4-photon protocols Boileau *et al.* (2004) and Li *et al.* (2008)

Ref. [18] predicted that their two protocols would show B92-like security [48]. Instead, our analysis shows BB84-like scaling with loss. This realisation was aided by the improved understanding of security analysis and standard techniques now available.

In Fig. S10, we present the key rate for the protocol in Ref. [19] compared to the 4-photon protocol of Ref. [18]. Ref. [19] outlined that their efficient measurement technique (that does not discard outcomes) would double their key rate. We observe this in Fig. S10 for the rotation-only protocol, verifying the claim. It should be noted, that for the dephasing-only approach, we do not observe this improvement. This is due to extracting key from both bases in our analysis. For the dephasing-only protocol, the bit values at Bob can only be determined for Z measurements and not for the X measurements, whereas key can be extracted from either measurement basis for the rotation-only scheme.

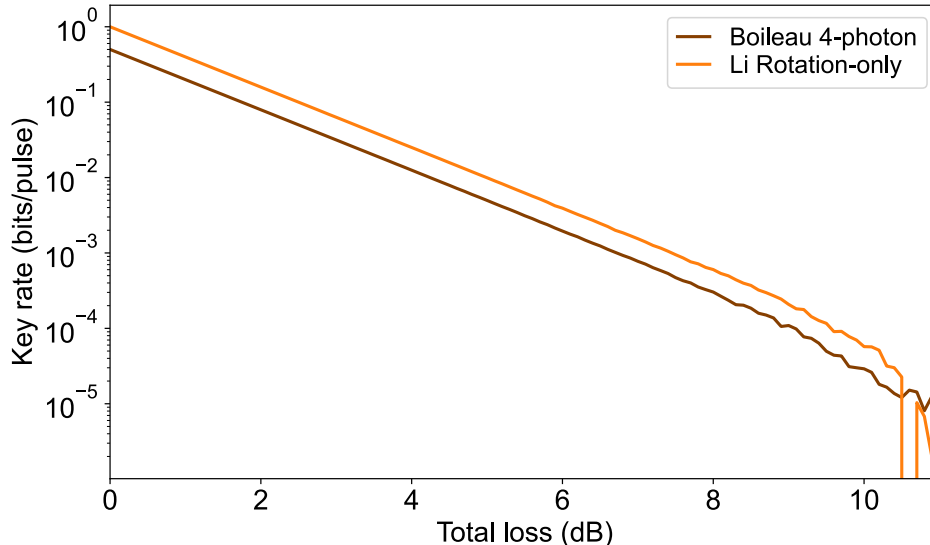


Fig S10. **Key rate for the 4-photon protocols in Li *et al.* (2008) and Boileau *et al.* (2004) as a function of loss.** The key rate as a function of loss for two 4-photon protocols that are robust to collective unitary noise. The protocol by Li *et al.* (2008) achieves double the key rate of Boileau *et al.* (2004) due to its efficient measurement scheme, at the cost of general unitary noise robustness.

For the 4-photon protocols in Fig. S10, instability and a reduction in key rate beyond the expected η^4 scaling appears at higher losses. This is attributed to the numerical instabilities of the key rate simulation, which uses a coordinate descent solver, at small key rate values. We justify this claim in Fig. S11 by simulating BB84 and Ref. [17] at high losses. As for Refs. [18] and [19], we also observe instabilities and a drop below the expected scaling once the key rate becomes small (on the order of 10^{-6}). Additionally, the high dimension of the 4-photon states used, adds extra uncertainty into the simulation, giving rise to these instabilities at larger values of key rate (on the order of 10^{-4}).

S.VIII. DISPERSION NOISE MODEL

A. Outline of chromatic dispersion model derivation

Single photons can be defined as positive frequency excitations of the electromagnetic field [66]. As a result, the quantum state $|\psi\rangle$ of a photon as a function of space and time (\mathbf{x}, t) can be written as

$$|\psi\rangle = \int_0^\infty d\omega g(\omega) e^{i(\omega t - \mathbf{k} \cdot \mathbf{x})} \hat{a}^\dagger(\omega) |\emptyset\rangle, \quad (\text{S1})$$

where $g(\omega)$ is a wavefunction as a function of frequency ω , and \mathbf{k} is the wavevector, given by $k = |\mathbf{k}| = n\omega/c$. Here, n is the refractive index of the medium being traversed [67].

Chromatic dispersion is an effect that arises when the refractive index (and correspondingly the wavevector) are frequency-dependent (i.e. $n(\omega), k(\omega)$ respectively). This occurs when a medium has electronic resonances [68]. Expressions for $k(\omega)$ for different media can be found, for example, through Sellmeier equations [69]. By performing a

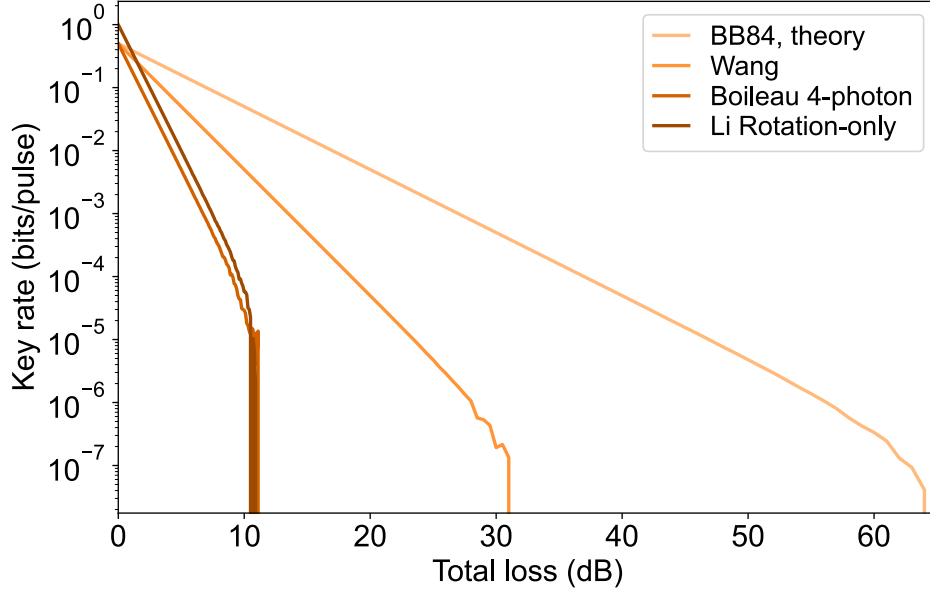


Fig S11. **Key rate for collective unitary noise-robust protocols as a function of loss.** At high loss values, when the key rate is small, instabilities appear in the numerical solver. Additionally, the smaller the dimension of the logical state, the smaller the key rate can be before the instabilities appear.

Taylor expansion of $k(\omega)$ about a central frequency ω_0 , such that we write

$$k(\omega) = \sum_{n=0}^{\infty} \frac{1}{n!} \left. \frac{\partial^n k}{\partial \omega^n} \right|_{\omega_0} (\omega - \omega_0)^n, \quad (\text{S2})$$

we see that the wavefunction of a photon state [Eq. (S1)] will accumulate a phase that depends on the frequency to different polynomial orders [24]. This is the effect of dispersion. Therefore, if only the n -th term is non-zero, we arrive at Eq. (7) in the main text, to describe the effect of dispersion on the spectral wavefunction, with $\alpha_n = \frac{1}{n!} \left. \frac{\partial^n k}{\partial \omega^n} \right|_{\omega_0}$.

Using the equation for the channel model given in Eq. (7) in the main text, we can write the effect of the channel noise model on the frequency-bin and time-bin Bell-state wavefunctions analytically. The transformed Bell-states are given by

$$\begin{aligned} \Psi_f'^- &= e^{i\alpha_n((\omega_1-\omega_0)^n + (\omega_2-\omega_0)^n)} \Psi_f^- \\ &= e^{i\alpha_n((\omega_1-\omega_0)^n + (\omega_2-\omega_0)^n)} A(\Omega_0, \Omega_1, \sigma_\omega) [f_{\Omega_0, \sigma_\omega}(\omega_1) f_{\Omega_1, \sigma_\omega}(\omega_2) - f_{\Omega_1, \sigma_\omega}(\omega_1) f_{\Omega_0, \sigma_\omega}(\omega_2)], \end{aligned} \quad (\text{S3})$$

$$\begin{aligned} \Psi_t'^- &= e^{i\alpha_n((\omega_1-\omega_0)^n + (\omega_2-\omega_0)^n)} \Psi_t^- \\ &= e^{i\alpha_n((\omega_1-\omega_0)^n + (\omega_2-\omega_0)^n)} A(\tau_0, \tau_1, \sigma_t) [F_{\tau_0, \sigma_t}(\omega_1) F_{\tau_1, \sigma_t}(\omega_2) - F_{\tau_1, \sigma_t}(\omega_1) F_{\tau_0, \sigma_t}(\omega_2)], \end{aligned} \quad (\text{S4})$$

where $f_{\Omega, \sigma_\omega}(\omega)$ and $F_{\tau, \sigma_t}(\omega)$ are the single-photon frequency-bin and time-bin states given by Eqs. (S1) and (S2), respectively, and $\Omega_0, \Omega_1, \omega_0$ are defined relative to the central frequency of the time-bin states, such that $\omega = 0$ THz at the centre of the time-bin state as defined in the frequency domain. Analysing the effect of this noise on our encoding requires calculating the fidelities and global phases (as for the FBS model), such that we can find key rates. Calculating the fidelities of the transformed states with the states measured by Bob ($|\langle \Psi_x'^- | \Psi_x^- \rangle|^2$ where x is f or t) and the bit error under the operation of the channel ($|\langle \Psi_t'^- | \Psi_f^- \rangle|^2$) therefore requires evaluating the 1D overlap terms

$$\begin{aligned} &\int_{-\infty}^{\infty} d\omega \exp(i\alpha_n(\omega - \omega_0)^n) f_{\Omega, \sigma_\omega}(\omega) f_{\Omega', \sigma_\omega}(\omega)^*, \\ &\int_{-\infty}^{\infty} d\omega \exp(i\alpha_n(\omega - \omega_0)^n) F_{\tau, \sigma_t}(\omega) F_{\tau', \sigma_t}(\omega)^*, \\ &\int_{-\infty}^{\infty} d\omega \exp(i\alpha_n(\omega - \omega_0)^n) f_{\Omega, \sigma_\omega}(\omega) F_{\tau, \sigma_t}(\omega)^*. \end{aligned}$$

In the next subsections, we calculate these terms for the first order dispersion ($n = 1$) and use these to calculate the fidelities and phases. We analyse these and convert them into key rates. Subsequently, we perform similar calculations for the second order dispersion term ($n = 2$). We give a heuristic understanding of the effect of chromatic dispersion on the states in the small α_n regime.

B. Linear dispersion ($n = 1$)

For the $n = 1$ case, we calculate the 1D overlap functions to be

$$\begin{aligned} & \int_{-\infty}^{\infty} d\omega \exp(i\alpha_1(\omega - \omega_0)) f_{\Omega, \sigma_\omega}(\omega) f_{\Omega', \sigma_\omega}(\omega)^* \\ &= \exp(-i\alpha_1\omega_0) \exp\left(-\frac{(\Omega - \Omega')^2}{4\sigma_\omega^2}\right) \exp\left(-\frac{\alpha_1^2\sigma_\omega^2}{4}\right) \exp\left(\frac{i\alpha_1(\Omega + \Omega')}{2}\right), \end{aligned} \quad (\text{S5})$$

$$\int_{-\infty}^{\infty} d\omega \exp(i\alpha_1(\omega - \omega_0)) F_{\tau, \sigma_t}(\omega) F_{\tau', \sigma_t}(\omega)^* = \exp(-i\alpha_1\omega_0) \exp\left(-\frac{(\alpha_1 + \tau' - \tau)^2}{4\sigma_t^2}\right). \quad (\text{S6})$$

$$\begin{aligned} & \int_{-\infty}^{\infty} d\omega \exp(i\alpha_1(\omega - \omega_0)) f_{\Omega, \sigma_\omega}(\omega) F_{\tau, \sigma_t}(\omega)^* \\ &= \sqrt{\frac{2\sigma_\omega\sigma_t}{1 + \sigma_\omega^2\sigma_t^2}} \exp(-i\alpha_1\omega_0) \exp\left(-\frac{\sigma_t^2\Omega^2}{2(1 + \sigma_\omega^2\sigma_t^2)}\right) \exp\left(-\frac{\sigma_\omega^2(\alpha_1 + \tau)^2}{2(1 + \sigma_\omega^2\sigma_t^2)}\right) \exp\left(\frac{i\Omega(\alpha_1 + \tau)}{(1 + \sigma_\omega^2\sigma_t^2)}\right), \end{aligned} \quad (\text{S7})$$

From these expressions, we calculate the fidelities between Bob's measurement state and the state sent by Alice (corresponding to Bob's measurement outcome probability), i.e. $|\langle \Psi'_x | \Psi_x^- \rangle|^2$ for x is f or t , as

$$|\langle \Psi'_f | \Psi_f^- \rangle|^2 = \exp(-\alpha_1^2\sigma_\omega^2), \quad (\text{S8})$$

$$|\langle \Psi'_t | \Psi_t^- \rangle|^2 = \exp\left(-\frac{\alpha_1^2}{\sigma_t^2}\right), \quad (\text{S9})$$

and the bit error rate between the bit sent by Alice and Bob's measurement, i.e. $|\langle \Psi'_t | \Psi_f^- \rangle|^2$, as

$$\begin{aligned} |\langle \Psi'_t | \Psi_f^- \rangle|^2 &= \frac{8\sigma_\omega^2\sigma_t^2}{(1 + \sigma_\omega^2\sigma_t^2)^2} \frac{1}{1 - \exp\left(-\frac{(\tau_0 - \tau_1)^2}{2\sigma_t^2}\right)} \frac{1}{1 - \exp\left(-\frac{(\Omega_0 - \Omega_1)^2}{2\sigma_\omega^2}\right)} \\ &\quad \times \exp\left(-\frac{\sigma_t^2(\Omega_0^2 + \Omega_1^2)}{(1 + \sigma_\omega^2\sigma_t^2)}\right) \exp\left(-\frac{\sigma_\omega^2[(\alpha_1 + \tau_0)^2 + (\alpha_1 + \tau_1)^2]}{(1 + \sigma_\omega^2\sigma_t^2)}\right) \\ &\quad \times \left[1 - \cos\left(\frac{(\Omega_1 - \Omega_0)(\tau_1 - \tau_0)}{(1 + \sigma_\omega^2\sigma_t^2)}\right)\right]. \end{aligned} \quad (\text{S10})$$

In Fig. S12, we present these fidelities as a function of α_1 for the states used in Fig. 4 of the main text.

First, we observe that the fidelities of both the frequency-bin and time-bin states with their untransformed states decay exponentially in α_1 and the bin width in the frequency domain (i.e. σ_ω and $1/\sigma_t$, respectively). We also see that σ_t and σ_ω have an inverse effect to each other on the fidelity between their original and noise-affected states, as expected from the properties of the Fourier transform on the time-bin state.

The bit error rate given in Eq. (S10) takes a maximum value at $\alpha_1 = -(\tau_0 + \tau_1)/2$. Thus, the bit error probability is upper bounded. In general, the upper bound will be small due to the decaying exponential terms, making the bit error rate negligible for all values of α_1 . For example, the bit error rate of the states shown in Fig. 4 in the main text (which have experimentally plausible parameters) is $\lesssim 10^{-4}$ for all α_1 .

To calculate the key rate, we must also consider any decoherence between the two logical states, which contributes to a phase error rate. To find the decoherence phase, we calculate the 2D overlap functions directly from the 1D overlap functions. The time-bin Bell-state accumulates no phase under this channel. We can explain this heuristically

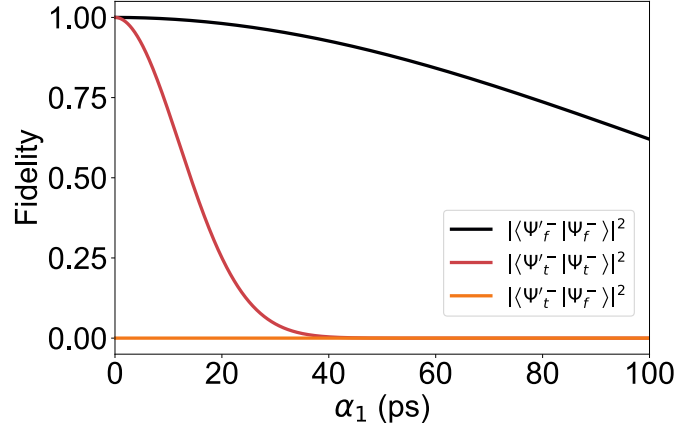


Fig S12. **Overlap fidelities at Bob given a state by Alice under the linear dispersion channel.** The state fidelities as a function of the linear dispersion parameter α_1 , for the parameters of Fig. 4 in the main text ($\tau_0 = 0$ ps, $\tau_1 = 220$ ps, $\sigma_t = 17$ ps, $\Omega_0 = 195.86$ THz, $\Omega_1 = 195.879$ THz, $\sigma_\omega = 1.1$ GHz). We have taken ω_0 and Ω_0 to be equal to the central frequency of the time-bin states.

as follows. In the small α_n regime, or if the states are sufficiently narrow in the frequency domain, the phase factor across a bin due to α_n can be taken to be approximately constant. Since the time-bin qubit states are centred around the same frequency, the channel approximates to an identity on the time-bin qubits. For the frequency-bin qubits, the phase factor on the two bins will be different, due to the separation of the central frequencies. Therefore, the frequency-bin Bell-state does accumulate a phase, which is given by $\alpha_1(\Omega_0 + \Omega_1)$. This results in a phase on the antisymmetric frequency-bin Bell-state and thus contributes to a decoherence between the logical $|0_L\rangle$ and $|1_L\rangle$ states, that depends linearly on the noise parameter α_1 . As the width of the qubit bins in the frequency domain increases, the contributions due to a varying phase across the bins must be accounted for, reducing the fidelity between the transmitted and arriving state as described above.

We now combine these results to calculate the key rate under the linear dispersion channel. The channel results in decaying fidelities, which correspond to an incurred total loss, and an additional asymmetric loss (amplitude damping), and decoherence. As we saw above, there is negligible bit error. Therefore, as for the FBS model, we can utilise the key rate conversion for an amplitude damping and decoherence channel, as outlined in Appendix E, to obtain a key rate for the encoding as a function of α_1 . The effect of the noise channel is $|0_L\rangle \rightarrow \exp(-\alpha_1^2 \sigma_\omega^2 / 2) \exp(i\alpha_1(\Omega_0 + \Omega_1)) |0_L\rangle$ and $|1_L\rangle \rightarrow \exp(-\alpha_1^2 / (2\sigma_t^2)) |1_L\rangle$. To convert this to a key rate, we must convert the channel into an expression obeying the form $|0_L\rangle \rightarrow |0_L\rangle$ and $|1_L\rangle \rightarrow \sqrt{\eta_0} e^{i\Delta} |1_L\rangle$, as used in Appendix E. We do this for the states shown in Fig. 4 of the main text (and SM, Fig. S12) with varying time-bin width, with parameters $\tau_0 = 0$ ps, $\tau_1 = 220$ ps, $\sigma_t = 10, 17, 30$ ps, $\Omega_0 = 195.86$ THz, $\Omega_1 = 195.879$ THz, and $\sigma_\omega = 1.1$ GHz, assuming the central frequency of the time-bin states is equal to ω_0 and the frequency of the first frequency-bin, Ω_0 . Similarly, setting $\sigma_t = 30$ ps, we vary $\Omega_1 = 0.01, 0.015, 0.2$ THz with respect to the central time-bin frequency.

To perform this conversion, we first take the incurred loss on both states due to inconclusive outcomes as an inherent overall loss. For the states we are considering, $\exp(-\alpha_1^2 / (2\sigma_t^2)) \leq \exp(-\alpha_1^2 \sigma_\omega^2 / 2)$ for all α_1 . Thus, the overall loss on the protocol equal to $1 - \exp(-\alpha_1^2 \sigma_\omega^2)$. We renormalise the operation of the channel by this factor, such that now $|0_L\rangle \rightarrow \exp(i\alpha_1(\Omega_0 + \Omega_1)) |0_L\rangle$ and $|1_L\rangle \rightarrow \exp(-\alpha_1^2 / (2\sigma_t^2)) / \exp(-\alpha_1^2 \sigma_\omega^2 / 2) |1_L\rangle$. We then use the equivalence of quantum states under a global phase and the symmetry of the key rate dependence on phase about the decoherence phase $\Delta = 0$, to reformulate this as an amplitude damping and decoherence channel $|0_L\rangle \rightarrow |0_L\rangle$ and $|1_L\rangle \rightarrow \exp(-\alpha_1^2 / (2\sigma_t^2)) / \exp(-\alpha_1^2 \sigma_\omega^2 / 2) \exp(i\alpha_1(\Omega_0 + \Omega_1)) |1_L\rangle$, with inherent loss $1 - \exp(-\alpha_1^2 \sigma_\omega^2)$. This is now written in the form given in Appendix E, and we can calculate the key rate as a function of α_1 . We present the key rates in Fig. S13 for varying time-bin widths σ_t .

Fig. S13(a) shows key rate decays faster as the σ_t decreases, as expected from Eq. (S6). Further, the key rate shows oscillations, taking zeros values. These correspond to the points at which the linear phase $\alpha_1(\Omega_0 + \Omega_1)$ is an odd multiple of $\pi/2$. In Fig. S13(b), we show that, by varying Ω_1 , the key rate can be optimised over a fluctuation range of α_1 , such that the average α_1 value is centred on a key rate peak, and avoid zeros in key rate over a selected range of α_1 . Therefore, if α_1 is allowed to fluctuate but within certain bounds, the key rate will remain close to a peak value. Hence, significant key rate can be achieved under this channel noise, by optimising the encoding parameters.

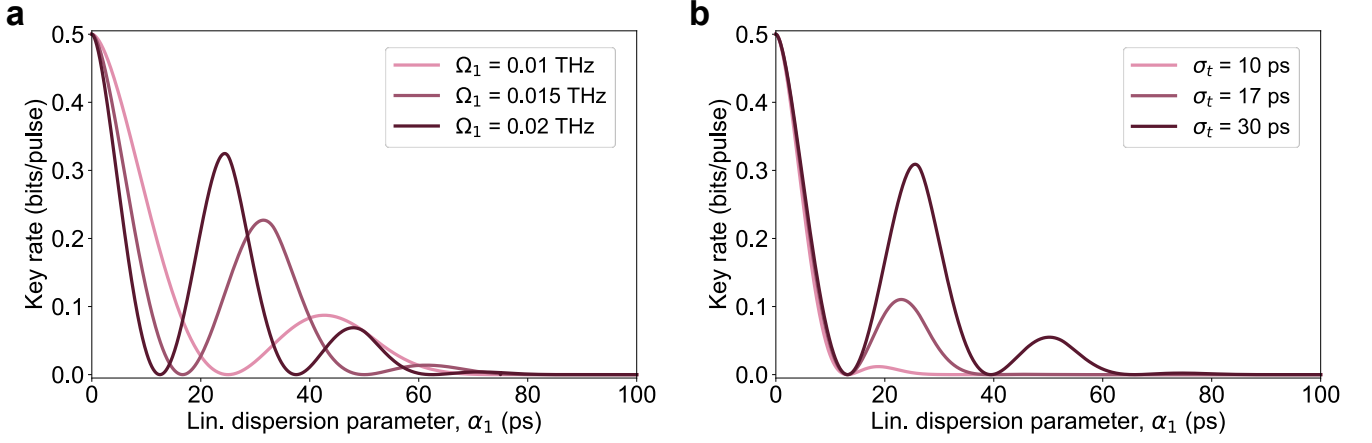


Fig S13. **Key rate as a function of the linear dispersion parameter.** The key rate as a function of the linear dispersion parameter α_1 with varying encoding variables. (a) Key rate for varying $\sigma_t = 10, 17, 30$ ps. The other encoding parameters are fixed, with $\Omega_0 = 19.86$ THz $\Omega_1 = 195.879$ THz, $\sigma_\omega = 1.1$ GHz, $\tau_0 = 0$ ps and $\tau_1 = 220$ ps, and ω_0 and Ω_0 are set equal to the central time-bin state frequency. (b) Key rate for varying $\Omega_1 = 0.01, 0.015, 0.02$ THz, with respect to the central time-bin frequency, keeping the other parameters from (a) the same, and setting $\sigma_t = 30$ ps.

C. Quadratic (group velocity) dispersion ($n = 2$)

We now perform the same calculations for the $n = 2$ case. The 1D overlap functions are now given by

$$\begin{aligned} & \int_{-\infty}^{\infty} d\omega \exp(i\alpha_2(\omega - \omega_0)^2) f_{\Omega, \sigma_\omega}(\omega) f_{\Omega', \sigma_\omega}(\omega)^* \\ &= \sqrt{\frac{1}{1 - i\alpha_2\sigma_\omega^2}} \exp(i\alpha_2\omega_0^2) \exp\left(-\frac{(\Omega^2 + \Omega'^2)}{2\sigma_\omega^2}\right) \exp\left(\frac{(\Omega + \Omega' - 2i\alpha_2\omega_0\sigma_\omega^2)^2}{4\sigma_\omega^2(1 - i\alpha_2\sigma_\omega^2)}\right), \end{aligned} \quad (\text{S11})$$

$$\begin{aligned} & \int_{-\infty}^{\infty} d\omega \exp(i\alpha_2(\omega - \omega_0)^2) F_{\tau, \sigma_t}(\omega) F_{\tau', \sigma_t}(\omega)^* \\ &= \sigma_t \sqrt{\frac{1}{\sigma_t^2 - i\alpha_2}} \exp(i\alpha_2\omega_0^2) \exp\left(-\frac{(\tau - \tau' + 2\alpha_2\omega_0)^2}{4(\sigma_t^2 - i\alpha_2)}\right), \end{aligned} \quad (\text{S12})$$

$$\begin{aligned} & \int_{-\infty}^{\infty} d\omega \exp(i\alpha_2(\omega - \omega_0)^2) f_{\Omega, \sigma_\omega}(\omega) F_{\tau, \sigma_t}(\omega)^* \\ &= \sqrt{\frac{2\sigma_\omega\sigma_t}{1 + \sigma_\omega^2\sigma_t^2 - 2i\sigma_\omega^2\alpha_2}} \exp(i\alpha_2\omega_0^2) \exp\left(-\frac{(\sigma_t^2 - 2i\alpha_2)\Omega^2}{2(1 + \sigma_\omega^2\sigma_t^2 - 2i\sigma_\omega^2\alpha_2)}\right) \\ & \quad \times \exp\left(-\frac{\sigma_\omega^2\tau^2}{2(1 + \sigma_\omega^2\sigma_t^2 - 2i\sigma_\omega^2\alpha_2)}\right) \exp\left(\frac{i\Omega\tau}{(1 + \sigma_\omega^2\sigma_t^2 - 2i\sigma_\omega^2\alpha_2)}\right) \\ & \quad \times \exp\left(-\frac{2i\alpha_2\omega_0\Omega}{(1 + \sigma_\omega^2\sigma_t^2 - 2i\sigma_\omega^2\alpha_2)}\right) \exp\left(\frac{2\sigma_\omega^2\alpha_2\omega_0\tau}{(1 + \sigma_\omega^2\sigma_t^2 - 2i\sigma_\omega^2\alpha_2)}\right) \exp\left(-\frac{2\sigma_\omega^2\alpha_2^2\omega_0^2}{(1 + \sigma_\omega^2\sigma_t^2 - 2i\sigma_\omega^2\alpha_2)}\right). \end{aligned} \quad (\text{S13})$$

As before, we use these to calculate the fidelities between Bob's measurement state and the state sent by Alice, which correspond to probabilities of Bob's measurement outcomes. To keep the expressions simpler, we take the case in which $\omega_0 = 0$ THz (i.e. $k(\omega)$ is expanded about the central frequency of the time-bin states). The fidelities are

then given by

$$|\langle \Psi_f'^- | \Psi_f^- \rangle|^2 = \frac{1}{\left[1 - \exp\left(-\frac{(\Omega_0 - \Omega_1)^2}{2\sigma_\omega^2}\right)\right]^2} \frac{1}{1 + \alpha_2^2 \sigma_\omega^4} \exp\left(-\frac{2\alpha_2^2 \sigma_\omega^2 (\Omega_0^2 + \Omega_1^2)}{1 + \alpha_2^2 \sigma_\omega^4}\right) \times \left[1 + \exp\left(-\frac{(\Omega_0 - \Omega_1)^2}{(1 + \alpha_2^2 \sigma_\omega^4) \sigma_\omega^2}\right) - 2 \exp\left(-\frac{(\Omega_0 - \Omega_1)^2}{2(1 + \alpha_2^2 \sigma_\omega^4) \sigma_\omega^2}\right) \cos\left(\frac{\alpha_2 (\Omega_0 - \Omega_1)^2}{2(1 + \alpha_2^2 \sigma_\omega^4)}\right)\right], \quad (\text{S14})$$

$$|\langle \Psi_t'^- | \Psi_t^- \rangle|^2 = \frac{1}{\left[1 - \exp\left(-\frac{(\tau_0 - \tau_1)^2}{2\sigma_t^2}\right)\right]^2} \frac{\sigma_t^4}{\sigma_t^4 + \alpha_2^2} \times \left[1 + \exp\left(-\frac{\sigma_t^2 (\tau_0 - \tau_1)^2}{(\sigma_t^4 + \alpha_2^2)}\right) - 2 \exp\left(-\frac{\sigma_t^2 (\tau_0 - \tau_1)^2}{2(\sigma_t^4 + \alpha_2^2)}\right) \cos\left(\frac{\alpha_2 (\tau_0 - \tau_1)^2}{2(\sigma_t^4 + \alpha_2^2)}\right)\right], \quad (\text{S15})$$

$$|\langle \Psi_t'^- | \Psi_f^- \rangle|^2 = \frac{1}{\left[1 - \exp\left(-\frac{(\tau_0 - \tau_1)^2}{2\sigma_t^2}\right)\right]} \frac{1}{\left[1 - \exp\left(-\frac{(\Omega_0 - \Omega_1)^2}{2\sigma_\omega^2}\right)\right]} \frac{4\sigma_t^2 \sigma_\omega^2}{(1 + \sigma_t^2 \sigma_\omega^2)^2 + 4\sigma_\omega^4 \alpha_2^2} \times \exp\left(-\frac{[\sigma_t^2 (1 + \sigma_t^2 \sigma_\omega^2) + 4\sigma_\omega^2 \alpha_2^2] (\Omega_0^2 + \Omega_1^2)}{(1 + \sigma_t^2 \sigma_\omega^2)^2 + 4\sigma_\omega^4 \alpha_2^2}\right) \exp\left(-\frac{\sigma_\omega^2 (1 + \sigma_t^2 \sigma_\omega^2) (\tau_0^2 + \tau_1^2)}{(1 + \sigma_t^2 \sigma_\omega^2)^2 + 4\sigma_\omega^4 \alpha_2^2}\right) \times \left[\exp\left(-\frac{4\sigma_\omega^2 \alpha_2 (\Omega_0 \tau_0 + \Omega_1 \tau_1)}{(1 + \sigma_t^2 \sigma_\omega^2)^2 + 4\sigma_\omega^4 \alpha_2^2}\right) + \exp\left(-\frac{4\sigma_\omega^2 \alpha_2 (\Omega_0 \tau_1 + \Omega_1 \tau_0)}{(1 + \sigma_t^2 \sigma_\omega^2)^2 + 4\sigma_\omega^4 \alpha_2^2}\right) - 2 \exp\left(-\frac{2\sigma_\omega^2 \alpha_2 (\Omega_0 + \Omega_1) (\tau_0 + \tau_1)}{(1 + \sigma_t^2 \sigma_\omega^2)^2 + 4\sigma_\omega^4 \alpha_2^2}\right) \cos\left(\frac{(1 + \sigma_\omega^2 \sigma_t^2) (\Omega_1 - \Omega_0) (\tau_1 - \tau_0)}{(1 + \sigma_t^2 \sigma_\omega^2)^2 + 4\sigma_\omega^4 \alpha_2^2}\right)\right]. \quad (\text{S16})$$

We observe that σ_t and σ_ω again play the same roles in the fidelities $|\langle \Psi_f'^- | \Psi_f^- \rangle|^2$ and $|\langle \Psi_t'^- | \Psi_t^- \rangle|^2$, with an inverse effect for σ_t due to the Fourier transform. In Fig. S14, we show these measurement probabilities as a function of α_2 for the states used in Fig. 4 of the main text ($\tau_0 = 0$ ps, $\tau_1 = 220$ ps, $\sigma_t = 17$ ps, $\Omega_0 = 195.86$ THz, $\Omega_1 = 195.879$ THz, and $\sigma_\omega = 1.1$ GHz, taking the central frequency of the time-bin states to equal Ω_0). As for linear dispersion, we find that the bit error rate is negligible ($\lesssim 10^{-4}$) compared to the asymmetric loss. Further, we see that probabilities decay an order of magnitude more slowly for the absolute value of the α_2 parameter than α_1 .

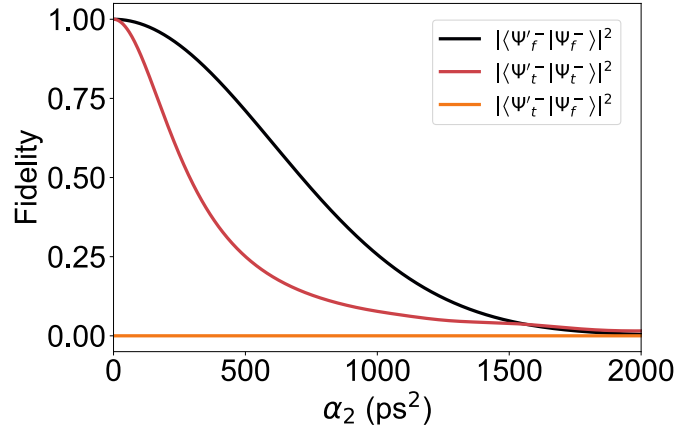


Fig S14. **Overlap fidelities at Bob given a state by Alice under the quadratic dispersion channel.** The state fidelities as a function of the quadratic dispersion parameter α_2 , for the parameters of Fig. 4 in the main text ($\tau_0 = 0$ ps, $\tau_1 = 220$ ps, $\sigma_t = 17$ ps, $\Omega_0 = 195.86$ THz, $\Omega_1 = 195.879$ THz, $\sigma_\omega = 1.1$ GHz). We have taken ω_0 and Ω_0 to be equal to the central frequency of the time-bin states.

To understand the parameter dependence of Equations (S14) and (S15) further, we visualise the dependence of the fidelities $|\langle \Psi_f'^- | \Psi_f^- \rangle|^2$ and $|\langle \Psi_t'^- | \Psi_t^- \rangle|^2$ on α_2 for varying parameters in Figs. S15 - S17.

Fig. S15 shows the fidelities as a function of α_2 for varying bin widths. As for linear dispersion, as the frequency-bin width σ_ω increases, the decay rate of frequency-bin state fidelity increases. Meanwhile, as the time-bin width σ_t increases, the time-bin state fidelity decays less rapidly.

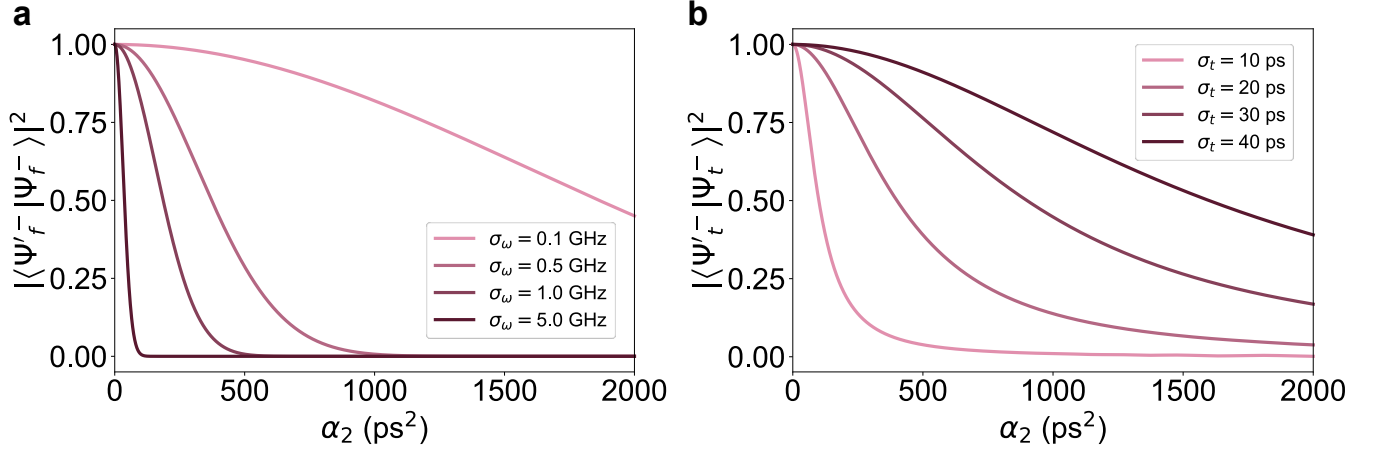


Fig S15. **Fidelity of the state arriving at Bob given a state sent down a quadratic dispersion channel by Alice for varying encoding bin widths.** (a) The frequency-bin state fidelity $|\langle \Psi'_f | \Psi_f^- \rangle|^2$ as a function of the quadratic dispersion parameter α_2 , for various frequency-bin widths σ_ω . The fixed frequency-bin parameters are $\Omega_0 = 195.86$ THz, $\Omega_1 = 195.94$ THz. (b) The time-bin state fidelity $|\langle \Psi'_t | \Psi_t^- \rangle|^2$ as a function of α_2 , for various time-bin widths σ_t . The time-bins are at times $\tau_0 = 0$ ps and $\tau_1 = 320$ ps. For both, the central time-bin state frequency is set equal to ω_0 and Ω_0 .

In Fig. S16, we present the fidelity of the frequency-bin state for varying Ω_0 (a) and varying Ω_1 (b) with σ_ω fixed. As Ω_0 and Ω_1 increase (relative to the central frequency of the time-bin state), the fidelity of the arriving state decreases. This can be understood from the exponential prefactor in Eq. (S14), which dominates the Ω_0 - and Ω_1 -dependence. The other exponential terms are approximately zero since $(\Omega_1 - \Omega_0) \geq 6\sigma_\omega$ is required for frequency-bins to form an approximate orthonormal basis. Thus, in the large α_2 limit, the fidelity decays exponentially with increasing Ω_0 and Ω_1 . For the small α_2 limit, we can understand Eq. (S14) using the heuristic explanation given in Section II A of the main text.

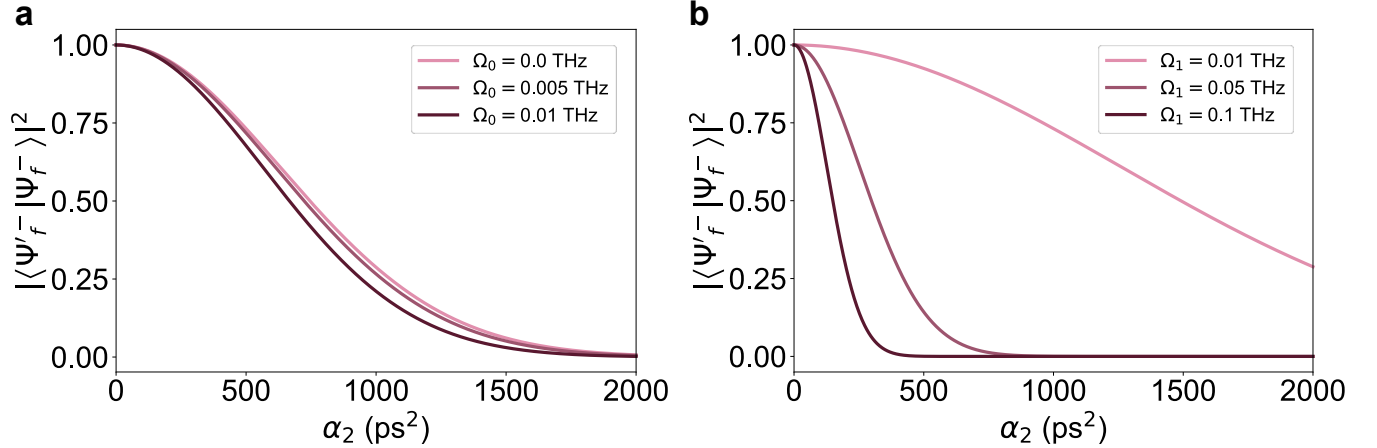


Fig S16. **Fidelity of the frequency-bin state arriving at Bob given a frequency-bin state sent down a quadratic dispersion channel by Alice for varying frequency-bin parameters Ω_0 and Ω_1 .** (a) The frequency-bin state fidelity $|\langle \Psi'_f | \Psi_f^- \rangle|^2$ as a function of the quadratic dispersion parameter α_2 , for $\Omega_0 = 0, 0.005, 0.1$ THz, relative to the central frequency of the time-bin states (which is set to be 195.86 THz). The fixed parameters are $\Omega_1 = 195.94$ THz and $\sigma_\omega = 1$ GHz. (b) The frequency-bin state fidelity as a function of α_2 , for $\Omega_1 = 0.01, 0.05, 0.1$ THz, relative to the central frequency of the time-bin states (again, set to be 195.86 THz). The fixed parameters are $\Omega_0 = 0$ THz (relative to the time-bin central frequency) and $\sigma_\omega = 1$ GHz.

In Fig. S17, we investigate the fidelity of the time-bin state for varying τ_0 (a) and varying τ_1 (b) with σ_t fixed. The fidelity shows minimal dependence on τ_0 and τ_1 . We can interpret this from the exponential terms in Eq. (S15). As for the frequency-bin states, these terms are approximately zero since $(\tau_1 - \tau_0) \geq 6\sigma_t$ is required to have time-bin distinguishability. Therefore, the fidelity falls approximately as $1/(1 + \alpha_2^2/\sigma_t^4)$, which is independent of τ_0 and τ_1 .

Small deviations can be seen in the large α_2 limit, where the exponential terms become non-negligible.

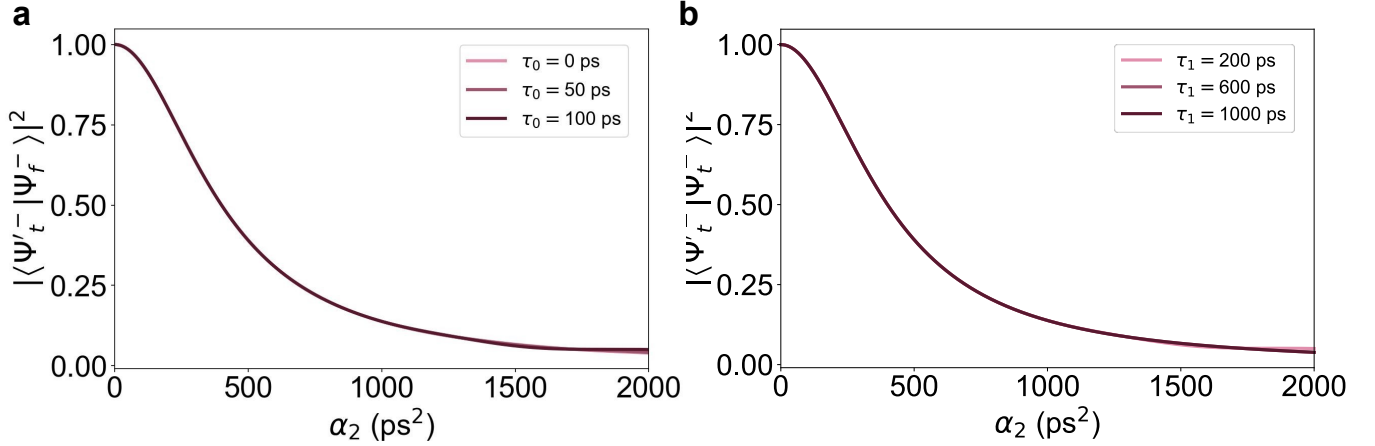


Fig S17. Fidelity of the time-bin state arriving at Bob given a time-bin state sent down a quadratic dispersion channel by Alice for varying time-bin parameters τ_0 and τ_1 . (a) The time-bin state fidelity $|\langle \Psi_t^- | \Psi_f^- \rangle|^2$ as a function of the quadratic dispersion parameter α_2 , for $\tau_0 = 0, 50, 100$ ps. The fixed parameters are $\tau_1 = 300$ ps and $\sigma_t = 20$ ps. (b) The time-bin state fidelity as a function of α_2 , for $\tau_1 = 200, 600, 1000$ ps. The fixed parameters are $\tau_0 = 0$ ps and $\sigma_t = 20$ ps.

Before calculating the key rate, we again briefly consider the logical decoherence. By studying Equations (S11) and (S12), we can see that the logical decoherence phase will take a more complex dependence on α_2 , with dependence on all encoding parameters $\Omega_0, \Omega_1, \sigma_\omega, \tau_0, \tau_1, \sigma_t$. We can understand the decoherence phase with the same general intuition given for the $n = 1$ case (but now for the time-bin states, there will also be an accumulated global phase relative to their untransformed states measured by Bob).

We now calculate the key rate of our encoding under quadratic dispersion now. We use the same method as for the $n = 1$ case (though now slightly more involved). To do this, we convert the incurred loss, amplitude damping and decoherence phase to key rates using Appendix E for the states of Fig. 4 in the main text (and SM, Fig. S14) with varying time-bin width and varying Ω_1 . As before, for each α_2 , we assume that there is an inherent channel loss given by the fidelity for each α_2 that takes the largest value of the frequency-bin or the time-bin state fidelity down the channel. We implement this as an incurred loss and renormalise. Again, we then use the equivalence of quantum states under global phase to move all phase dependence onto the logical state that has lower fidelity under the channel. The channel has then been transformed into a form that can utilise the conversion in Appendix E.

We present the key rate as a function of α_2 in Fig. S18(a) for varying time-bin width. As for linear dispersion, we see that as the time-bin width decreases, the rate at which the key rate decays with α_2 increases. Now, we also find that rate of oscillations in the key rate with α_2 increases as the time-bin width increases, since the decoherence phase now also depends on σ_t and the other encoding parameters. Overall, we find that high key rates can be achieved, even for large values of dispersion. For example, considering dispersion only and using the experimental value of $\alpha_2 \approx -27$ ps²/km in fused silica at around 1540nm [70–72], the encoding in Fig. S18(a) can achieve key rates around 0.01 bits/pulse over at least 60km of optical fibre. In Fig. S18(b), we show how varying Ω_1 , as an illustrative example, we can again optimise the encoding such that α_2 is allowed to fluctuate over a significant range whilst maintaining a non-zero key rate.

S.IX. COMPARISON OF OUR ENCODING TO ALTERNATIVE CONTINUOUS DOF ENCODINGS

A. Bell-states across different frequency-bins

In Appendix D, we presented an alternative encoding in the frequency domain, using Bell-states on two pairs of frequency bins, and justified why our proposed encoding allows for higher robustness under reduced noise assumptions. We discussed qualitatively the effect of the FBS operation when it acts on frequency bins that are not the frequency bins chosen for the encoding (in the worst case, when the noise acts on only one of the encoding bins with another bin outside the space). Here, we provide a mathematical analysis of this discussion.

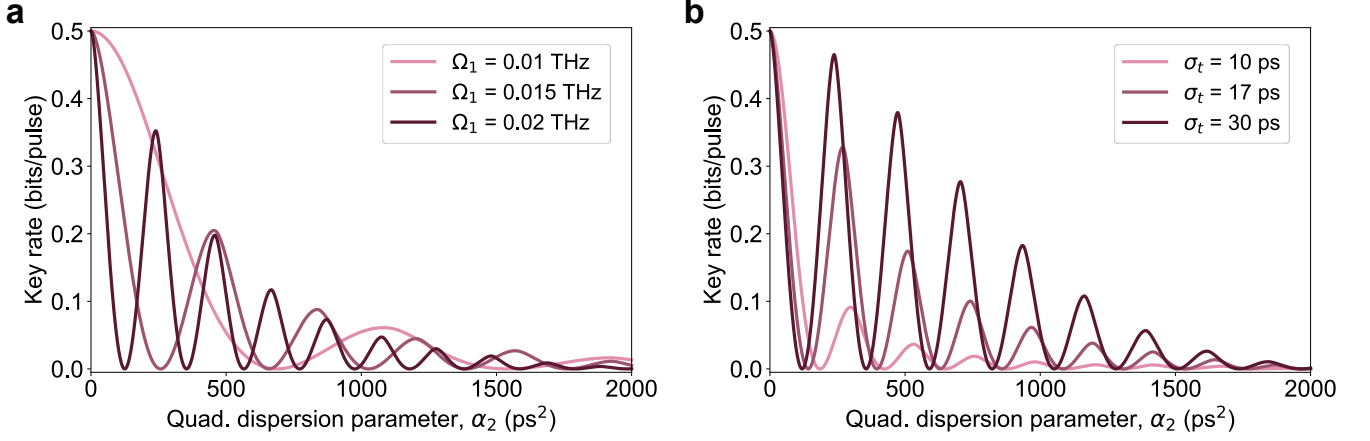


Fig S18. **Key rate as a function of the quadratic dispersion parameter.** The key rate as a function of the linear dispersion parameter α_2 with varying encoding variables. (a) Key rate for varying $\sigma_t = 10, 17, 30$ ps. The other encoding parameters are fixed, with $\Omega_0 = 19.86$ THz $\Omega_1 = 195.879$ THz, $\sigma_\omega = 1.1$ GHz, $\tau_0 = 0$ ps and $\tau_1 = 220$ ps, and ω_0 and Ω_0 are set equal to the central time-bin state frequency. (b) Key rate for varying $\Omega_1 = 0.01, 0.015, 0.02$ THz, with respect to the central time-bin frequency, keeping the other parameters from (a) the same, and setting $\sigma_t = 30$ ps.

First, we demonstrate analytically the effect of this change of the FBS operation on our encoding. As described in the Appendix D, we show there is only an additional incurred loss with negligible incurred bit error rate. Subsequently, we will apply the same analysis to the alternative encoding to show that a bit error rate will be incurred.

To show this, we consider that an FBS noise operation acts across the frequency-bin $|0_f\rangle$ and a third bin, which we label as a qudit state $|2_f\rangle$, and another FBS acts across bin $|1_f\rangle$ and a fourth bin, $|3_f\rangle$. The FBS acts unitaries across these frequency bins, which we label $U_{02}(\theta_1, \phi_1)$ and $U_{13}(\theta_2, \phi_2)$, respectively. The unitary operation $U_{ab}(\theta, \phi)$ on states $|a_f\rangle$ and $|b_f\rangle$ takes the form

$$U_{ab}|a_f\rangle = \cos\theta|a_f\rangle + e^{i\phi}\sin\theta|b_f\rangle, \quad (\text{S1})$$

$$U_{ab}|b_f\rangle = -e^{-i\phi}\sin\theta|a_f\rangle + \cos\theta|b_f\rangle. \quad (\text{S2})$$

Acting these FBS unitary operations on the frequency-bin Bell-state $|0_L\rangle = |\Psi_f^-\rangle_{01,AB}$ results in the state

$$\begin{aligned} U_{02} \otimes U_{13} |\Psi_f^-\rangle_{01} &= \frac{1}{\sqrt{2}} [(\cos\theta_1|0_f\rangle + e^{i\phi_1}\sin\theta_1|2_f\rangle)(\cos\theta_2|1_f\rangle + e^{i\phi_2}\sin\theta_2|3_f\rangle) \\ &\quad - (\cos\theta_2|1_f\rangle + e^{i\phi_2}\sin\theta_2|3_f\rangle)(\cos\theta_1|0_f\rangle + e^{i\phi_1}\sin\theta_1|2_f\rangle)] \\ &= \cos\theta_1\cos\theta_2|\Psi_f^-\rangle_{01} + e^{i\phi_1}\sin\theta_1\cos\theta_2|\Psi_f^-\rangle_{21} \\ &\quad + e^{i\phi_2}\sin\theta_2\cos\theta_1|\Psi_f^-\rangle_{03} + e^{i(\phi_1+\phi_2)}\sin\theta_1\sin\theta_2|\Psi_f^-\rangle_{23} \end{aligned} \quad (\text{S3})$$

at Bob, where $|\Psi_f^-\rangle_{ab,AB} = \frac{|a_f\rangle_A|b_f\rangle_B - |b_f\rangle_A|a_f\rangle_B}{\sqrt{2}}$, as described in Appendix D.

We now consider the effect of this on our encoding. Under the previous noise model (Section II B in the main text), we saw that the frequency-bin state was unaffected and the time-bin state had a reduced fidelity. Under the new model, the time-bin state will show a reduction in fidelity as before, but reduced further by the double FBS operation (see Fig S6), and the overlap of the time-bin state with the frequency-bin state will remain negligible. However, now the frequency-bin Bell-state will also “leak” outside of the logical subspace. The overlap of the transformed frequency-bin Bell-state with its untransformed version $|\Psi_f^-\rangle_{01}$ is reduced from 1 to $\cos\theta_1\cos\theta_2$ [Eq (S3)]. To summarise the effect of this revised model on our encoding, in the Z_L basis, there will be no bit error rate, but now an incurred loss for the $|0_L\rangle$ state of $l_0 = (1 - \cos^2\theta_1\cos^2\theta_2)$ will arise. The incurred loss for $|1_L\rangle$ is found using the methods in Sections S.III and S.IV.

We now compare this to the effect of the revised double FBS operation on the alternative encoding (outlined in Appendix D). We will demonstrate the claim that this encoding can give rise to both an incurred loss and a bit error rate, in contrast to our encoding.

First, let us assume that each FBS acts between each one of the encoding frequency-bins with another frequency-bin that lies outside of the chosen encoding space (i.e. the FBS applies unitaries $U_{04}, U_{15}, U_{26}, U_{37}$). In this case, there is no bit error rate, but each of the two logical qubit basis states has an incurred loss of $l = (1 - \cos^2 \theta_1 \cos^2 \theta_2)$, as seen for our encoding, where θ_1 and θ_2 are the unitary rotation angles that will be different for each frequency-bin pair.

In contrast, if we assume now that the double FBS acts on the worst pairing of bins, such that it applies unitaries $U_{02}(\theta_1, \phi_1)$ and $U_{13}(\theta_2, \phi_2)$ on the frequency-bin pairs $\{|0_f\rangle, |2_f\rangle\}$ and $\{|1_f\rangle, |3_f\rangle\}$, as before, then a bit error rate will also be induced. The effect of $U_{02} \otimes U_{13} |\Psi_f^-\rangle_{01}$ is given by Eq. (S3). The effect of $U_{02} \otimes U_{13} |\Psi_f^-\rangle_{23}$ is given by

$$\begin{aligned} U_{02} \otimes U_{13} |\Psi_f^-\rangle_{23} &= \cos \theta_1 \cos \theta_2 |\Psi_f^-\rangle_{23} - e^{i\phi_2} \sin \theta_2 \cos \theta_1 |\Psi_f^-\rangle_{21} \\ &\quad - e^{i\phi_1} \sin \theta_1 \cos \theta_2 |\Psi_f^-\rangle_{03} + e^{-i(\phi_1 + \phi_2)} \sin \theta_1 \sin \theta_2 |\Psi_f^-\rangle_{01} \end{aligned} \quad (\text{S4})$$

From this, we see that there is an incurred loss of $l_0 = l_1 = 1 - \cos^2 \theta_1 \cos^2 \theta_2 - \sin^2 \theta_1 \sin^2 \theta_2$ for both logical basis states. However, this additionally demonstrates the accumulation of a non-negligible bit error rate of $e_{bit} = \sin^2 \theta_1 \sin^2 \theta_2$ (not normalised for the loss rate), and phase error rate of $e_{ph} = \sin^2(\phi_1 + \phi_2) \sin^2 \theta_1 \sin^2 \theta_2$.

Thus, we have shown that we can achieve better robustness under fewer assumptions on the noise, using our encoding, compared to an alternative encoding. In contrast to our encoding, the alternative encoding will acquire a bit error rate, that can lead to the abortion of the protocol under sufficiently large noise parameters (θ_1, θ_2) .

B. Bell-states of different symmetries

We present another alternative encoding. However, we explain that this encoding does not give rise to a secure QKD protocol, and thus cannot be employed.

Using the ideas in Ref. [17], with the conjugate bases encoding of our scheme, one could consider an alternative continuous DoF encoding in which the key states are given by $|\Psi_f^-\rangle$ and $|\Psi_f^+\rangle$, and the test states are given by $|\Psi_t^-\rangle$ and $|\Psi_t^+\rangle$ (where $|\Psi_x^+\rangle = (|0_x\rangle_A |1_x\rangle_B - |1_x\rangle_A |0_x\rangle_B)/\sqrt{2}$ and x is f or t). Bob could then perform a simpler measurements by performing a Bell-state measurement in either the frequency or the time basis. However, the states of opposite symmetry are always orthogonal (i.e. the symmetric frequency-bin Bell-states are orthogonal to the antisymmetric time-bin Bell-states, and vice versa, as is evident from the equations in Section S.II). This renders the encoding completely insecure, since it forbids Alice and Bob from gaining phase information about the channel, to verify the security of the channel.

From a geometrical picture, these states comprise a 4-dimensional, rather than 2-dimensional space. Eve can make measurements in the higher dimensional space that leave the states in the lower dimensional subspace on which Bob measures undisturbed.

S.X. COLLECTIVE NOISE WITH DIFFERENCES IN NOISE PARAMETERS

Typical experimental implementations of protocols using logical states with multiple photons will expect small deviations of the noise parameters between the photons in the logical state. These deviations are anticipated when the photons are temporally separated or spatially routed into two different fibre cores, for example, so that they can be distinguished. In this section, we analyse the impact of these small experimental deviations in the FBS noise parameters and the dispersion noise between the two photons of our encoding on the fidelity and key rate.

A. FBS noise deviations

Representing the FBS parameters as $\vec{\epsilon} = (\Omega, \mu, \epsilon, \theta, \phi)$ and difference in these parameters between the two photons as $\vec{\delta} = (\delta_\Omega, \delta_\mu, \delta_\epsilon, \delta_\theta, \delta_\phi)$, we model the FBS channel now as applying

$$\rho \rightarrow (\hat{F}_{\vec{\epsilon}} \otimes \hat{F}_{\vec{\epsilon} + \vec{\delta}}) \rho (\hat{F}_{\vec{\epsilon}}^\dagger \otimes \hat{F}_{\vec{\epsilon} + \vec{\delta}}^\dagger), \quad (\text{S1})$$

where $\hat{F}_{\vec{\epsilon}}$ is the FBS channel with parameters $\vec{\epsilon}$.

In Fig. S19, we present the fidelity of the transformed time-bin states compared to the time-bin states sent by Alice and measured by Bob, for varying deviations in each of the noise parameters (including $\vec{\delta} = 0$ plots for comparison

to perfect collective noise). The results in Fig. S19 show that the deviations only have a marginal impact on the fidelity, even under relatively large deviations on the noise parameters between the two photons. Experimentally, the photons are expected to be transmitted in close temporal and spatial proximity, meaning the δ values are expected to be small. Additionally, under these deviations, the bit error rate remains negligible. Similarly, the global phase accumulated by the time-bin state remains small, such that it only contributes to a small reduction in key rate. It is only for large values of δ_ϕ that large global phases, resulting in significant reductions in key rate, are seen. However, as described above, this is unlikely to be expected in typical experimental scenarios.

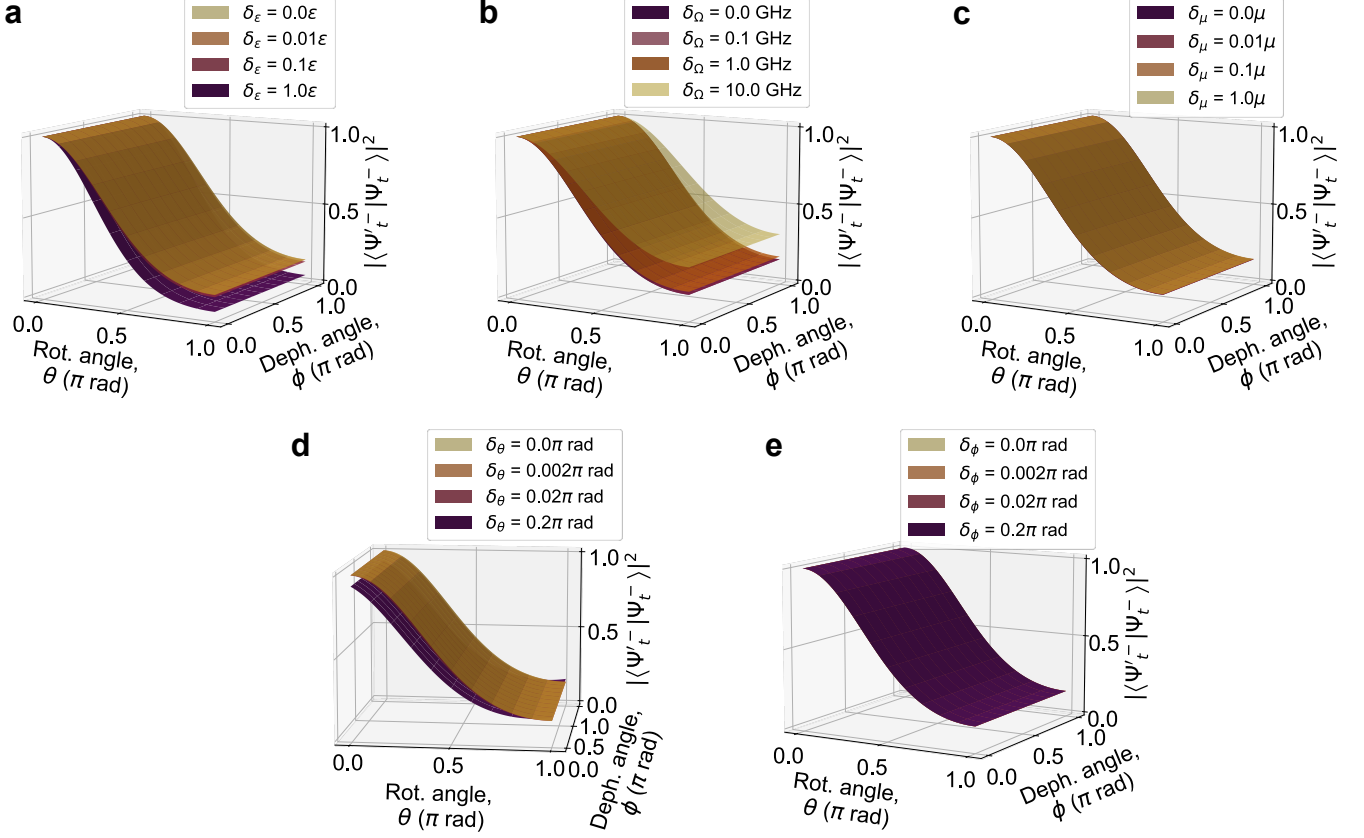


Fig S19. **Robustness of the time-bin Bell-states under FBS noise with deviations between the noise parameters on the two photons.** Fidelity between the arriving state $|\Psi_t^-\rangle$ sent by Alice through the FBS channel with deviating noise parameters on the two photons and the state $|\Psi_t^-\rangle$ measured by Bob. We use values close to the experimentally reported values in Refs. [33, 34], with $\tau_0 = 0$ ps, $\tau_1 = 220$ ps, and $\sigma_t = 17$ ps and a central frequency of 195.860 THz, with FBS noise parameters on the first photon given by $\Omega = 195.860$ THz, $\mu = 0.019$ THz, $\epsilon = 3.0$ GHz. The fidelity is plotted as a function of θ and ϕ for different values of δ_x (with all other δ 's being zero) where x is (a) the noise bin width ϵ , (b) the first noise bin central frequency Ω , (c) the noise bin separation μ , (d) the unitary rotation angle θ , and (e) the unitary dephasing angle ϕ . δ_ϵ and δ_μ are given as fractions of the value of the noise parameters on the first photon, whilst δ_Ω , δ_θ and δ_ϕ are given as absolute values.

In addition to the effect of these parameter deviations on the time-bin states, we must consider the effect on the frequency-bin states. We assume ϵ is always sufficiently large to contain the encoded bins, and that the deviations of Ω and μ are considered still contain either all or none of the encoded bins, such that a unitary is applied to the frequency bins. From Section S.IX.A we know that deviations in Ω or μ to states bins outside of the encoded space simply result in a higher rate of inconclusive outcomes. Considering then the effect of deviations in the θ parameter, with $\phi = 0$, on the frequency-bin state, we assume the action of the FBS on the frequency-bin Bell-states is a unitary with rotation angle θ on one frequency-bin qubits ($U_f(\theta, \phi = 0)$), and a unitary with rotation angle $\theta + \delta_\theta$ on the other ($U_f(\theta + \delta_\theta, \phi = 0)$). Using the small angle approximation, up to $\mathcal{O}(\delta^2)$, this transforms the two-photon frequency-bin state to

$$U_f(\theta, \phi = 0) \otimes U_f(\theta + \delta_\theta, \phi = 0) |\Psi_f^-\rangle = (1 - \delta_\theta^2/2) |\Psi_f^-\rangle - \delta_\theta |\Phi_f^+\rangle. \quad (\text{S2})$$

From this, we see there is a small increase in inconclusive outcomes due to rotating the state into $|\Phi_f^+\rangle$, with a rate given by δ_θ^2 . $|\Phi_f^+\rangle$ will always be orthogonal to an antisymmetric state, due to the orthogonality of opposite symmetry states. In this case, the time-bin state arriving is not perfectly antisymmetric due to the difference in noise parameters between the two qubits. However, since the deviations are typically small, and the time-bins will be broad in frequency, whilst the $|\Phi_f^+\rangle$ is made from narrow frequency bins, the overlap between the two states will remain small. Hence, there is negligible increase in the bit error rate of our encoding.

Bringing these effects together, we see that experimental deviations in the noise parameters between the two photons of the logical state has only a small affect on the achievable key rates of our protocol, due to a marginal increase in inconclusive rates.

B. Dispersion noise deviations

For the dispersion noise, we assume that one photon sees the dispersion parameter α_n and the other photon sees $\alpha_n + \delta_\alpha$ for a fixed n , where δ_α is the experimental deviation.

We present the effect of this in Fig. S20. We see that this offset in the dispersion parameter causes a translation of the key rate with α_n . As discussed for the FBS model, typically experimental deviations between the two photons are small. Therefore, this also has a minimal effect on the key rate of our encoding. Additionally, this can be accounted for in the optimisation of the encoding parameters. Thus, our protocol performs well under and is high applicability to experimentally expected scenarios.

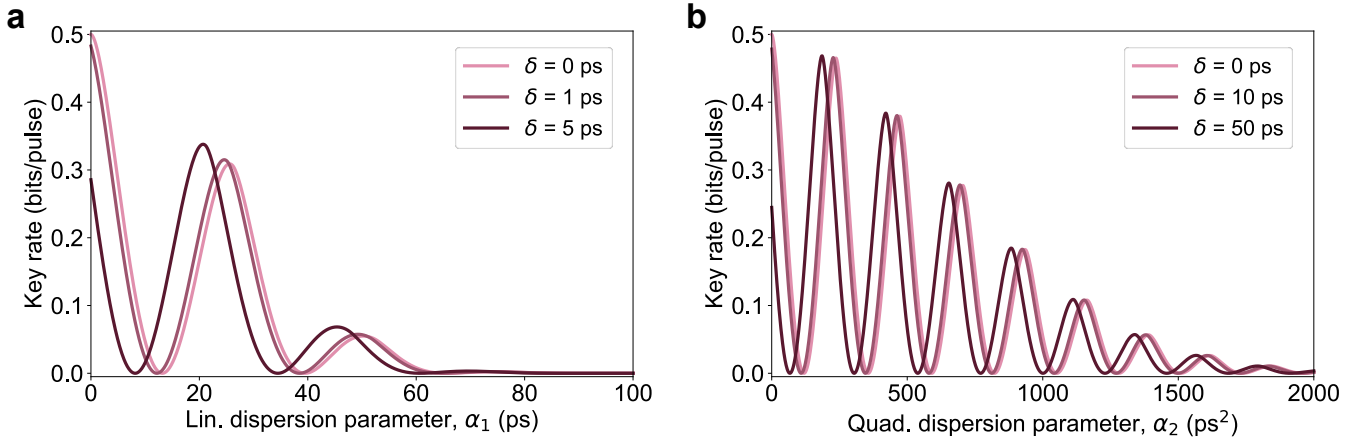


Fig S20. **Robustness of the time-bin Bell-states under dispersion noise with deviations between the noise parameters on the two photons.** Fidelity between the arriving state $|\Psi_t^-\rangle$ sent by Alice through the dispersion channel with deviating noise parameters on the two photons and the state $|\Psi_t^-\rangle$ measured by Bob. We use values close to the experimentally reported values in Refs. [33, 34], with $\tau_0 = 0$ ps, $\tau_1 = 220$ ps, and $\sigma_t = 30$ ps and a central frequency of 195.860 THz. The key rate is plotted as a function of (a) linear dispersion, α_1 , and (b) quadratic dispersion α_2 , with the dispersion parameters offset by an absolute fixed value δ .

S.XI. FREQUENCY-DEPENDENT CHANNEL LOSS

In many practical set-ups, for example, in optical fibres, the absorption of the light is dependent on the frequency of the light [73]. Since we encode photons in the frequency domain across different frequency modes, we should briefly consider the effect of this loss on our encoding.

The logical states are encoded in antisymmetric Bell-states, hence both photons in each state are equally superposed across the different frequencies. Therefore, the effect of loss should be the same on both photons in the logical state, and it is quick to see that the effect of the channel for the frequency-bin Bell-states is simply loss with a probability given by the average of the loss for the two frequencies of the encoding. For the time-bin Bell-states, the average loss will be given by the loss probability of the central frequency of the encoding. This will give rise to an amplitude damping

effect on the key rate, as covered in Appendix E, which can be small if the encoded frequencies are appropriately chosen.